MAGMATIC PROCESSES AT THE GALÁPAGOS 93.25˚W

OVERLAPPING SPREADING CENTER

A THESIS SUBMITTED TO THE GRADUATE DIVISION OF THE
UNIVERSITY OF HAWAI‘I IN PARTIAL FULFILLMENT
OF THE REQUIREMENTS FOR THE DEGREE OF

MASTERS OF SCIENCE

IN

GEOLOGY AND GEOPHYSICS

May 2008

By
Melissa D. Rotella

Thesis Committee:

John Sinton, Chairperson
Julia Hammer
Garrett Ito
John Mahoney

We certify that we have read this thesis and that, in our opinion, it is satisfactory in scope and quality as a thesis for the degree of Master of Science in Geology and Geophysics.

THESIS COMMITTEE

_____

Chairperson

_____

_____

_____

ACKNOWLEDGMENTS

I wish to thank the National Science and Engineering Research Council of Canada for providing me with a Post Graduate Award which funded a large portion of this research. National Science Foundation grants OCE 98-18632 and OCE 03-27051 funded sample collection and analyses and provided financial support. I am indebted to the many hours of laboratory assistance and useful discussions provided by Doug Pyle. Special thanks to Stephanie Ingle, Richard Hey and Mark Behn for providing useful discussions that greatly improved this manuscript. Many thanks to JoAnn Sinton for thin section preparation, Eric Hellebrand for help with on the electron microprobe, William Chazey for some ICPMS data collection, and Loyc Vanderkluysen for his help in the isotope lab. Finally, I wish to thank my committee, John Sinton, John Mahoney, Garrett Ito and Julia Hammer, for their advice and patience.

ABSTRACT

Major, trace and Sr-Nd-Pb isotopic data as well as plagioclase and olivine mineral compositions from samples encompassing the 93.25˚W offset on the Galápagos Spreading Center have been used to understand the magmatic processes at overlapping spreading centers (OSCs). Results show significant variations in composition and extent of low-pressure fractionation over short along-axis distances suggesting magma chambers at 93.25˚W are likely small, discontinuous, and/or poorly mixed. High-Mg, crystal-rich lavas containing multiple populations of plagioclase and olivine with significant variation from grain interior to exterior, and which are significantly out of equilibrium with their host glasses, suggests that lavas from the overlapping limbs originated from magma chambers with low overall melt supply. Isotopic ratios suggest source mixing primarily between two components. Correlation of incompatible element ratios with isotopic ratios allow samples to be separated into three geochemical types: relatively incompatible-element enriched (eT-MORBs), depleted (dT-MORBs) and normal (nT-MORBS) lavas. A long-wavelength along-axis geochemical gradient is apparent along western GSC (e.g. in $^{206}Pb/^{204}Pb$, Nb/Zr, Nb/La), but is interrupted by geochemical variability in the 93.25˚W overlap zone. Propagating rift samples show a decrease in incompatible trace element ratios from east to west, as the OSC is approached. This trend is interrupted inside the overlap zone and a similar trend begins, consistent with an interpretation based on bathymetry for dueling propagation and ridge abandonment in this area. Outside the overlap zone doomed rift samples do not vary beyond the long-wavelength gradation, within the overlap zone they show sharp decreases in incompatible trace element ratios. Three explanations are considered for the generation of incompatible-element depleted lava compositions: (1) increased degrees of melting, (2) melting an incompatible-element depleted source, or (3) variations in melt migration focusing within the upwelling zone. Chemical, mineralogical and petrographic evidence for low melt supply in the OSC argues against increased degree of melting. Although the concept of incomplete melt focusing in the overlap zone is viable, we currently are unable to test this hypothesis. Melting of previously melted mantle is consistent with the geometry of the OSC, such that each limb could be tapping mantle that was previously cycled though the melting zone of the other limb.

TABLE OF CONTENTS

LIST OF TABLES

LIST OF FIGURES

Chapter 1: Magmatic Processes

1. Introduction

1.1 Propagating Ridges and Overlapping Spreading Centers

Overlapping spreading centers (OSCs) are a type of mid-ocean ridge offset in which the two ridge axes or 'limbs' overlap. Typically, the ratio of overlap to offset distance is ~3:1, consistent with crack propagation theory (Macdonald et al., 1984). Since the discovery of these features on the seafloor there has been debate as to the volcanotectonic processes that form them (Macdonald and Fox, 1983; Lonsdale, 1983; Schouten and Klitgord, 1983; Macdonald et al., 1984; Lonsdale 1985; Lonsdale 1986; Macdonald et al., 1986; Sempere and Macdonald, 1986). Two models that have been proposed for the development of OSCs on fast-spreading mid-ocean ridges differ in their relationship with subaxial magma chambers. One model involves low magma supply resulting in separate, small, non-steady-state magma chambers under each overlapping limb (Macdonald and Fox, 1983; Macdonald et al., 1984). Alternatively, OSCs might form in regions of high magma supply with a single, large magma chamber shared between the opposing limbs (Lonsdale, 1983, 1985). Each model has implications for the composition of lavas erupted at the opposing limbs. In the high supply model one might expect the composition of lavas erupted on the two overlapping limbs to be consistent with evolution in the same magma reservoir. In the low supply model a broader range of compositions should be present, possibly reflecting differences in mantle sources or in magmatic evolution (Macdonald, et al., 1986). A large, broad low velocity zone, inferred to be a magma chamber, has been imaged through seismic tomography at the 9˚N OSC on the East Pacific Rise (EPR), possibly supporting the high magma supply model (Kent

et al. 1993; Dunn et al., 2001), although this is the only OSC with this level of investigation and it is unknown if this result is typical of OSCs.

Work by Hey (1977a), Hey et al. (1980, 1989), Sinton et al. (1983), Pollard and Aydin (1984), and Phipps Morgan and Parmentier (1985) has shown that some ridge offsets, including some OSCs, have a history of along-axis propagation. In such cases, the propagating limb breaks through older, off-axis ocean crust while the failing or doomed rift progressively ceases to be active. This process produces a V-shaped wake of new seafloor on the propagating limb, the boundaries of which are termed pseudofaults because they represent age and topographic discontinuities on the seafloor that resemble faults despite having formed by simple accretion processes. Past positions of the doomed rift are visible on the seafloor as a zone of failed or abandoned rifts. In this process new lithosphere created on one plate can be transferred to the other plate with the passing of the propagating rift, resulting in a zone of transferred lithosphere (Hey et al., 1989). Propagating OSCs have a broad transform zone between the overlapping segments (Hey et al., 1989), as the spreading rate varies from zero to the full rate on the propagating rift, with a complementary decrease in spreading rate on the failing or dying rift. Ridges that propagate continuously but do not overlap develop an instantaneous transform fault between the propagating and doomed rift.

The petrology and geochemistry of lavas erupted along OSCs can be useful in understanding crustal magma chamber dynamics and melting conditions in the source mantle at mid-ocean ridges. Previous petrological investigations of OSCs with propagation histories include studies along the Juan de Fuca Ridge (Sinton et al., 1983; Karsten et al., 1990) and at 20.17˚S on the EPR (Sinton et al., 1991). These studies show

that small-scale mantle heterogeneities and poor mixing can occur in these environments. Two major propagating OSCs occur along the western Galápagos Spreading Center (GSC), the well-documented 95.5˚W propagator (Hey et al. 1980; Christie and Sinton, 1981; 1986; Sinton et al., 2003) and the less well studied offset at 93.25˚W (Wilson and Hey, 1995; Sinton et al., 2003). Wilson and Hey (1995) documented propagation histories of the 95.5°W and 93.25°W propagators, and Sinton et al. (2003) described differences in bathymetry, magma supply, and first-order geochemical expressions of these two offsets.

The focus of the present study is a detailed geochemical investigation of lavas in the 93.25°W region with emphasis on the magma chamber and mantle melting processes occurring there. The goals of this work are to use mineral chemistry, major, trace and isotopic data to better understand the magmatic processes that contribute to the differences between the offsets at 95.5° and 93.25°W, with global implications for magmatism at mid-ocean ridge offsets with variable magma supply, propagation histories, offset geometries and composition of upwelling mantle. Results of this study show that the 93.25˚W offset differs widely from the offset at 95.5˚W and may share similarities to other more geochemically and petrologically diverse OSCs such as those on the Juan de Fuca Ridge and at 20˚S on the EPR.

1.2 The Galápagos Spreading Center

1.2.1 Geologic Background

Spreading along the GSC initiated 23-25 Ma when the Farallon plate broke apart along the pre-existing east-west trending Pacific-Farallon fracture zone (Hey, 1977b).

The 90 Ma Galápagos hotspot, which has been centered approximately beneath the GSC axis for most of the history of the spreading center, and is currently located beneath the Galápagos Islands, produced the Carnegie and Cocos aseismic ridges which track the motion of the Cocos and Nazca plates over the hotspot (Figure 1). Current GSC full spreading rates vary from 63 mm/yr at 86˚W to 45 mm/yr at 98˚W, with a rate of ~52 mm/yr at the 93.25˚W OSC (DeMets et al., 1994; Wilson and Hey, 1995). Over the last 5 million years the GSC has generally been migrating to the north, away from the hotspot. Analysis of magnetic anomaly profiles indicates the presence of four rift tips on the GSC with a history of propagation away from the Galápagos hotspot. These rifts have propagation rates ranging from 30-120 mm/yr, commonly near 70 mm/yr (Wilson and Hey, 1995). Two of them, at 95.5˚W and 93.25˚W, are on the western GSC, west of the Galápagos Transform, which is near 90°50'W. These propagating rifts are associated with predominantly southward ridge jumps closer to the hotspot where the crust is hotter and weaker (Hey, 1977b); this process has played an important role in the continuous reorganization of the geometry of the ridge axis (Hey, 1977b; Wilson and Hey, 1995).

Early work showed that many geochemical aspects display regular variations and a degree of symmetry along the GSC with distance from the nearby Galápagos hotspot (Schilling et al., 1976; Fisk et al., 1982; Schilling et al., 1982; Verma and Schilling, 1982; Fisk, 1986). More recent studies have confirmed and expanded on the nature of these regional geochemical patterns (Detrick et al., 2002; Schilling, 2003; Cushman et al., 2004; Christie et al., 2005; Ingle et al., in prep).

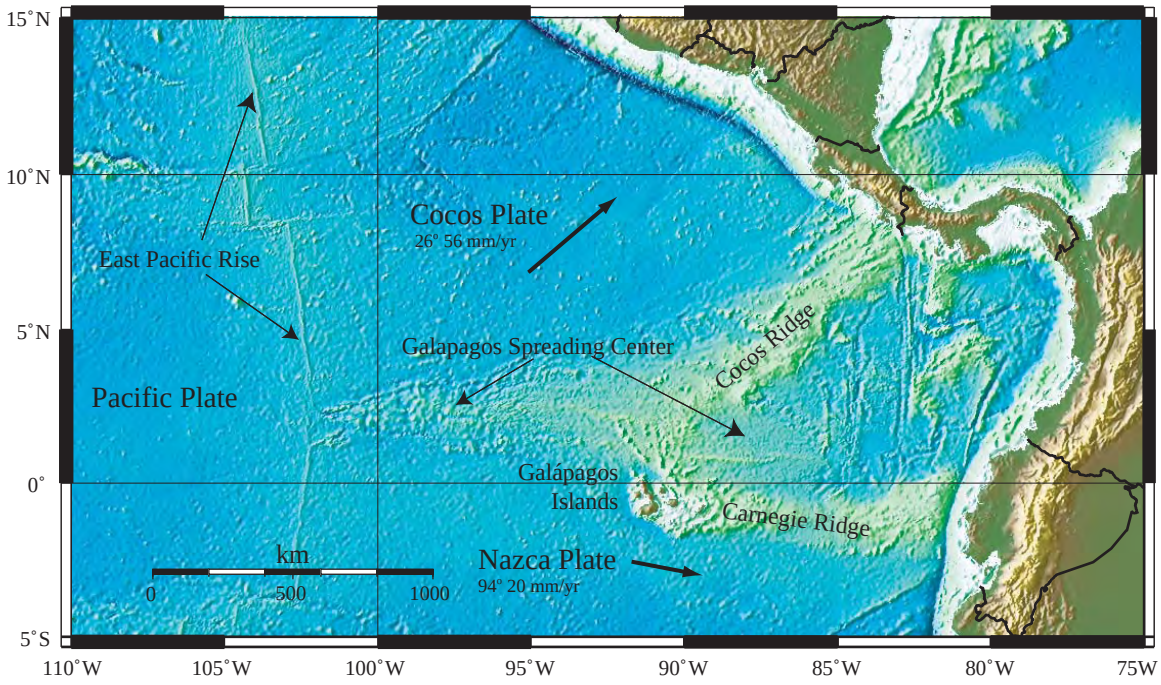

Figure 1 . Geologic setting of the Galápagos Spreading Center (GSC) located in the eastern central Pacific and separating the Cocos and Nazca plates (modified from Cushman et al., 2004). The Galápagos hotspot is currently located beneath the western Galápagos Islands; the Carnegie and Cocos aseismic ridges track the location of the Nazca and Cocos plates, respectively, over the hotspot (Hey, 1977b). The western GSC encompasses the portion of ridge west of the Galápagos transform fault near 91˚W.

1.2.2 The G-PRIME Cruise

In 2000, the Galápagos Plume Ridge Interaction Multidisciplinary Experiment (G-PRIME) was carried out along the western GSC with the goal of understanding the effects of variations in magma supply and primary magma composition on axial topography and crustal magma chambers along an 800-km length of the western GSC from ~91°W to 98°W. This project included multibeam bathymetric mapping, seismic refraction and reflection, gravity measurements, and sampling along axis. Results from this cruise show that the western GSC can be broken into three characteristic provinces (Sinton et al., 2003). The Eastern Province from the Galápagos transform near 90.5˚W to 92.7˚W is closest to the hotspot, has elevated bathymetry with axial highs, small-scale segmentation, a shallow axial magma chamber (AMC) reflector (Detrick et al., 2002; Blacic et al., 2004; Chen and Lin 2004) and a pronounced negative residual mantle Bouguer gravity anomaly (Canales et al., 2002; Detrick et al, 2002). Lavas in this region are incompatible-element-enriched mid-ocean ridge basalts (E-MORB) (Schilling et al., 1982; Sinton et al., 2003; Cushman et al., 2004). Within the Middle Province, between 92.7˚W and the 95.5˚W propagating rift tip, the GSC transitions to deeper bathymetry with the development of an axial valley, larger-scale segmentation, deepening and eventual disappearance of the AMC reflector and a less negative residual mantle Bouguer gravity anomaly. Lavas in this region, which encompasses the 93.25˚W OSC, are transitional T-MORB. Within the Western Province, west of 95.5˚W, normal N-MORB are erupted inside deeper and broader axial valleys. Changes occur in volcanic style from a low abundance of seamounts east of 92.7˚W to high abundance of seamounts in the

axial zone west of 95.5˚W; axial seamounts are rare in the region underlain by a relatively shallow, steady-state AMC (Behn et al., 2004).

1.2.3 The 95.5° and 93.25°W Offsets

The 95.5˚W propagator on the western GSC is one of the most intensively studied propagating ridges in the world (Hey and Vogt, 1977; Hey et al., 1980; Christie and Sinton, 1981; 1986; Hey et al., 1986; Cooper et al., 1987; Kleinrock et al., 1989; Kleinrock and Hey, 1989a, b; Phipps Morgan and Parmentier 1985; Hey et al., 1992). From these studies have evolved generalized models for sub-axial asthenospheric upwelling and magmatic process at propagating and doomed rifts (Christie and Sinton, 1981, Schilling et al., 1982; Sinton et al., 1983; Hey et al., 1989, 1992). The 95.5˚W offset has been propagating into 1 million year old Cocos plate lithosphere at ~50 km/my for at least 3 million years (Hey and Vogt, 1977; Hey et al., 1980). This process has produced a characteristic V-shaped wedge of young lithosphere with unusually high-amplitude magnetic anomalies and petrological diversity. Of note are the positive fractionation and negative bathymetric anomalies behind this propagating rift, which also occur at many other major propagators world wide (e.g., Sinton et al., 1983, Sinton et al., 1991). The fractionation anomaly at 95.5˚W is seen as a decrease in magnesium number (Mg#) of the lavas as the propagating tip is approached. Mg# is proportional to magma temperature, therefore could be representative of cooler and more evolved lavas which have undergone higher degrees of crystal fractionation. Propagating rift lavas at 95.5˚W display a striking and unusual compositional diversity, ranging from highly magnesian to Fe-, Ti-, and Zr-enriched basalts, and rarely to tholeiitic andesites and rhyodacites

(Byerly and Melson, 1976; Byerly, 1980; Christie and Sinton, 1981; Hey et al., 1989). Basalt glasses along the propagating rift are generally more differentiated than those of the doomed and failing rifts (Christie and Sinton, 1986; Hey et al., 1989). Also, the propagating limb is deeper than the surrounding ridge. These anomalies have been related to a delicate balance between cooling rate and reduced magma supply at the tip of a propagating rift (Christie and Sinton, 1981; Sinton et al., 1983; Hey et al., 1989).

The morphology of the 93.25˚W propagating rift differs significantly from the 95.5˚W propagator. It is a classic overlapping spreading center with approximately 24 km of overlap, and 7.5 km of offset whereas 95.5˚W has ~15 km of overlap with an offset of 22.2 km. The overlapping limbs lack pronounced deep bathymetry, instead they are up to 150 m shallower than the surrounding axial ridges away from the offset (Sinton et al., 2003). Lavas have T-MORB compositions; failing rift lavas show an increase in Magnesium within the overlap zone but propagating rift lavas lack the strong fractionation anomaly that characterizes the propagating limb at 95.5˚W and most propagating rifts worldwide. These differences suggest that processes that typically occur at magma-starved propagating rifts, or many other OSCs, may not be at play at 93.25˚W. The 93.25˚W rift has a higher propagation rate than observed at 95.5˚W (70 mm/yr vs. 48 mm/yr) (Wilson and Hey, 1995), and is breaking through younger (260 ka vs. 910 ka) and thicker (6.4 km vs. 5.7 km) crust; overall magma supply is ~20% greater owing to the closer proximity to the Galápagos hotspot (Sinton et al., 2003).

1.2.4 The 93°W Study Area

The 93.25˚W study area comprises a right-stepping offset that separates the eastern and western limbs. Following the terminology of Hey et al. (1989), the eastern limb is the propagating rift and the western limb is the doomed rift, which eventually will fail if propagation continues. The two limbs overlap between 93.13°W and 93.42°'W. Thus the region around the offset can be divided into four regions: the propagating limb east of 93.13°W (which we refer to as the propagating rift or PR), the portion of the PR within the overlap zone (OPR), the doomed rift west of 93.42˚W (DR) and the extension of the doomed limb within the overlap zone (ODR), i.e. the dying or failing rift (Figure 2). The 93.25°W region is in the middle province of the western GSC, characterized by the eruption of T-MORB and where the AMC lies at intermediate depth below the seafloor (Detrick et al., 2002; Sinton et al., 2003; Cushman et al., 2004).

2. Methods

2.1 Sample Selection

The study area includes a sample suite encompassing 24 G-PRIME dredge stations along a 175-km-long section of the GSC spanning the 93.25˚W offset (Figure 2). Geochemical groups within dredge sites were previously defined using major element glass data on one or more samples from every dredge station and reported as group averages (Cushman et al., 2004). For this study, one sample was chosen from each previously defined geochemical group for natural glass trace element analyses by inductively coupled plasma mass spectrometry (ICPMS) and, if enough sample was available, whole rock major and trace element analyses by X-ray fluorescence (XRF)

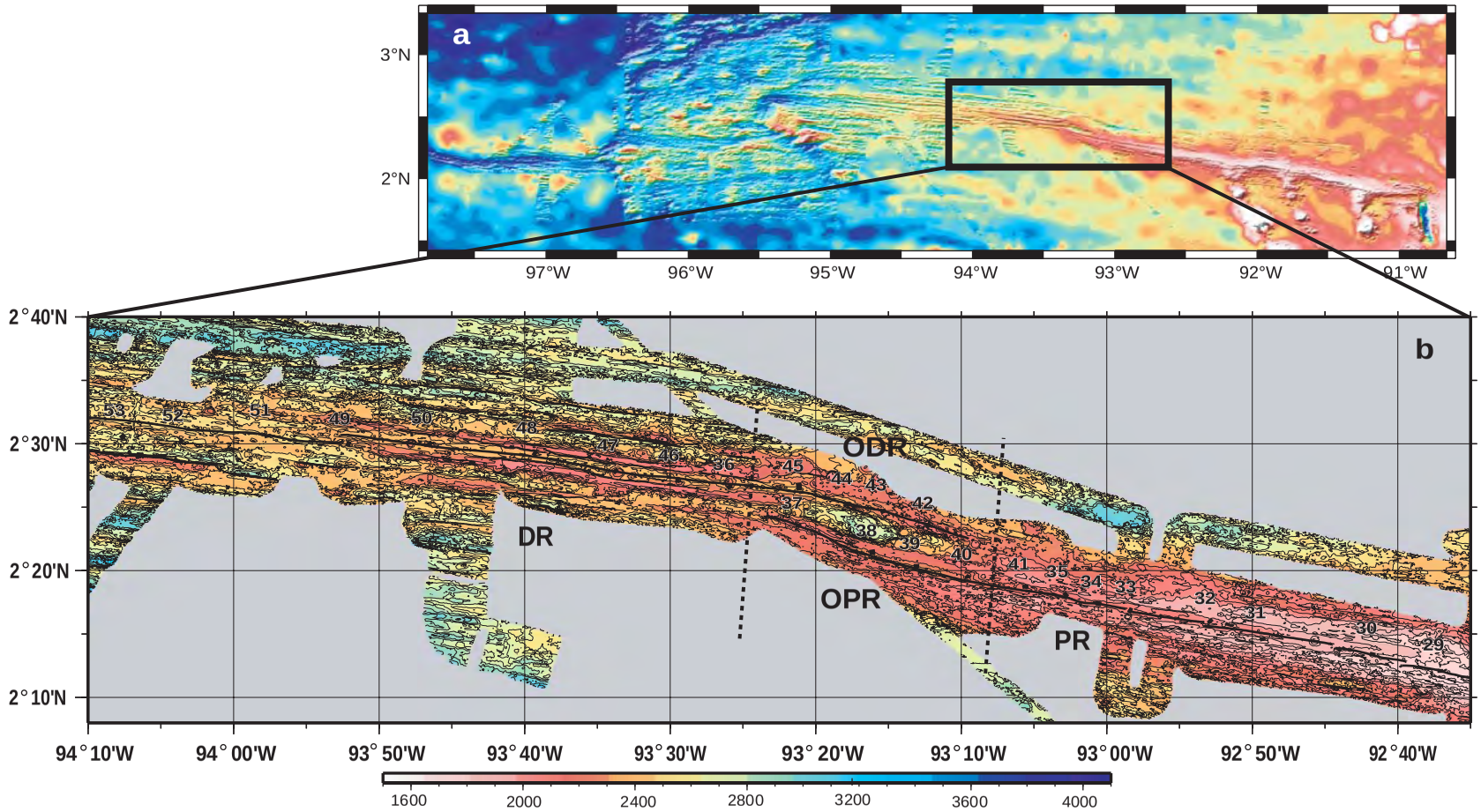

Figure 2. (a) Bathymetry of the western GSC; contour interval is 250 m. Note the transition from axial-high morphology in the east to axial-valley morphology in the west. The black box shows the region enlarged in (b) detailing the location of G-PRIME dredge sites used for this study. The four regions of the study area are labeled. Thin, black, east-west trending line segments represent the ridge axis. Dredge sites are numbered, dotted lines separate the four regions: propagating ridge (PR), overlapping propagating ridge (OPR), overlapping doomed ridge (ODR), and doomed ridge (DR). Contour interval is 50 m. Multibeam bathymetric data from Sinton et al. (2003).

spectrometry. A subset of five hand-picked natural glasses was analyzed for Sr, Nd, and Pb isotopes by thermal ionization mass spectrometry (TIMS). These data complement previously collected ICPMS analyses of 9 samples and isotopic analyses of 6 samples (Ingle et al., in prep) from the study area. Petrographic descriptions and electron microprobe data on mineral compositions were collected for olivine and plagioclase in 12 samples. See Appendix A for glass compositions of all study area samples used to define the chemical groups of Cushman et al. (2004).

2.2 Analytical Methods

Olivine and plagioclase mineral compositions (Tables 1, 2) were determined using the University of Hawai‘i Cameca SX-50 five-spectrometer electron microprobe. Mineral analyses are reported for cores and rims (grain interior and exterior) and are averages of two to eight spots collected from individual crystals. A PAP-ZAF matrix correction was applied to all analyses, which were obtained with a finely focused (~1 μm) beam diameter. Plagioclase was analyzed for Si, Al, Fe, Mg, Ca, Na, and K using an accelerating voltage of 15 kV and a beam current of 15 nA, using mineral standards Lake County plagioclase (Si and Al), San Carlos olivine (Fe and Mg), Amelia albite (Na), anorthite (Ca) and orthoclase (K) for calibration. Peak counting times were 30 s for Na and Si, 40 s for Mg and Al, and 70 s for K, Ca and Fe. Background counting times were 15 s for Na and Si, 20 s for Mg and Al, and 35 s for K, Ca and Fe. Sodium was analyzed first to minimize loss due to volatilization. Olivine was analyzed for Si, Mg, Fe, Ca, Mn and Ni using an accelerating voltage of 15 kV and a beam current of 20 nA,

Table 1. Olivine Compositions - Representative Grains

	29-1		31-1				34-4						36-1		38-2						39-1					
grain	9		10*		6		4		13		11		8	9	11*		19b		13*		18		7		19	
	core	rim	core	rim	core	rim	core	rim	core	rim	core	rim	core	core	core	rim	core	rim	core	rim	core	rim	core	rim	core	rim
n	3	3	3	3	3	3	3	4	3	3	3	4	4	4	3	3	4	3	3	3	3	3	3	3	3	3
Oxides (wt%)																										
SiO_2	38.6	38.6	38.9	38.8	38.7	38.9	39.1	38.9	38.9	39.0	39.2	39.0	38.8	39.2	39.0	38.8	38.7	38.9	39.4	38.9	39.2	39.1	39.1	39.4	39.2	39.1
MgO	41.2	41.7	39.9	39.8	39.3	39.9	43.7	42.6	41.9	42.1	43.1	42.8	40.4	41.6	40.9	40.4	39.7	40.4	42.7	40.5	44.1	43.6	43.1	44.0	43.9	43.7
FeO*	18.7	18.6	19.5	19.7	20.5	19.5	16.7	17.6	18.2	18.1	17.0	17.2	19.4	17.7	18.9	19.3	20.1	19.5	16.6	19.1	15.4	16.0	17.5	16.3	15.8	15.9
CaO	0.31	0.30	0.29	0.31	0.28	0.30	0.30	0.32	0.30	0.31	0.30	0.31	0.28	0.31	0.30	0.30	0.25	0.28	0.30	0.30	0.30	0.30	0.30	0.33	0.31	0.31
MnO	0.31	0.27	0.29	0.29	0.31	0.29	0.27	0.28	0.28	0.27	0.29	0.26	0.26	0.24	0.30	0.31	0.28	0.28	0.23	0.30	0.25	0.26	0.27	0.22	0.21	0.21
NiO	0.10	0.11	0.10	0.09	0.06	0.09	0.17	0.13	0.12	0.13	0.15	0.14	0.09	0.12	0.10	0.11	0.16	0.13	0.12	0.11	0.13	0.13	0.11	0.15	0.13	0.14
Total	99.2	99.6	99.0	99.0	99.2	99.0	100.2	99.9	99.7	99.9	100.0	99.8	99.2	99.2	99.5	99.3	99.3	99.5	99.3	99.3	99.3	99.3	100.4	100.4	99.7	99.5
Cations based on 4 oxygens																										
Si	0.996	0.993	1.009	1.008	1.007	1.008	0.990	0.993	0.997	0.996	0.995	0.995	1.004	1.005	1.003	1.004	1.005	1.004	1.005	1.005	0.995	0.995	0.992	0.993	0.994	0.995
Mg	1.587	1.597	1.543	1.539	1.525	1.544	1.649	1.620	1.599	1.605	1.631	1.627	1.558	1.592	1.570	1.558	1.537	1.556	1.621	1.560	1.669	1.653	1.629	1.654	1.660	1.656
Fe	0.404	0.400	0.423	0.429	0.445	0.423	0.354	0.376	0.391	0.387	0.362	0.366	0.419	0.381	0.408	0.418	0.437	0.421	0.354	0.413	0.326	0.341	0.371	0.344	0.336	0.339
Ca	0.009	0.008	0.008	0.009	0.008	0.008	0.008	0.009	0.008	0.008	0.008	0.009	0.008	0.009	0.008	0.008	0.007	0.008	0.008	0.008	0.008	0.008	0.008	0.009	0.008	0.009
Mn	0.007	0.006	0.006	0.006	0.007	0.006	0.006	0.006	0.006	0.006	0.006	0.006	0.006	0.005	0.006	0.007	0.006	0.006	0.005	0.006	0.005	0.006	0.006	0.005	0.005	0.005
Ni	0.002	0.002	0.002	0.002	0.001	0.002	0.004	0.003	0.003	0.003	0.003	0.003	0.002	0.003	0.002	0.002	0.003	0.003	0.002	0.002	0.003	0.003	0.002	0.003	0.003	0.003
Sum	3.004	3.007	2.991	2.992	2.993	2.992	3.010	3.007	3.003	3.004	3.005	3.005	2.996	2.994	2.997	2.996	2.995	2.996	2.995	2.995	3.005	3.005	3.008	3.007	3.006	3.005
Fo	79.7	80.0	78.5	78.2	77.4	78.5	82.3	81.1	80.4	80.6	81.8	81.6	78.8	80.7	79.4	78.9	77.9	78.7	82.1	79.1	83.6	82.9	81.5	82.8	83.2	83.0

	40-2						42-4				43-1		44-1	48-1				49-1		
grain	8		7		10		2a		4		15		9*	8		7		4*		
	core	rim	core	rim	core	rim	core	rim	core	rim	core	rim	core	core	rim	core	rim	core	rim	
n	3	3	3	3	3	3	3	3	2	2	4	4	5	3	3	3	3	3	3	σ
Oxides (wt%)																				
SiO_2	40.1	39.9	39.7	40.0	39.8	39.9	40.4	40.0	39.7	39.8	40.0	39.9	39.6	39.2	39.5	39.6	39.6	38.5	38.4	0.13
MgO	47.7	46.9	45.7	46.4	46.4	46.5	48.9	46.8	46.1	46.3	45.9	45.7	45.8	44.2	44.6	44.6	44.8	40.5	39.8	0.13
FeO*	11.4	12.3	13.9	13.0	13.1	13.0	10.1	12.2	13.4	13.0	12.6	12.8	13.6	15.8	15.2	15.3	15.2	20.5	21.0	0.01
CaO	0.32	0.32	0.32	0.33	0.30	0.33	0.32	0.32	0.31	0.33	0.35	0.36	0.32	0.32	0.34	0.30	0.33	0.26	0.28	0.02
MnO	0.15	0.19	0.20	0.17	0.19	0.22	0.19	0.17	0.17	0.17	0.21	0.20	0.19	0.23	0.23	0.26	0.21	0.32	0.33	0.11
NiO	0.23	0.25	0.17	0.17	0.21	0.20	0.26	0.18	0.16	0.15	0.16	0.13	0.21	0.13	0.14	0.14	0.14	0.09	0.09	0.02
Total	99.9	99.9	100.0	100.0	100.0	100.1	100.1	99.8	99.9	99.8	99.2	99.1	99.7	100.0	100.0	100.1	100.3	100.1	100.0	0.21
Cations based on 4 oxygens																				
Si	0.994	0.993	0.993	0.995	0.993	0.993	0.992	0.996	0.992	0.994	1.002	1.001	0.994	0.992	0.995	0.995	0.994	0.993	0.995	0.004
Mg	1.760	1.740	1.706	1.723	1.724	1.725	1.791	1.737	1.719	1.724	1.715	1.713	1.711	1.665	1.674	1.671	1.677	1.555	1.538	0.002
Fe	0.237	0.256	0.291	0.270	0.273	0.270	0.207	0.254	0.281	0.272	0.263	0.268	0.284	0.334	0.320	0.322	0.319	0.443	0.455	0.000
Ca	0.008	0.009	0.009	0.009	0.008	0.009	0.008	0.009	0.008	0.009	0.009	0.010	0.009	0.009	0.009	0.008	0.009	0.007	0.008	0.001
Mn	0.003	0.004	0.004	0.004	0.004	0.005	0.004	0.004	0.004	0.004	0.004	0.004	0.004	0.005	0.005	0.006	0.004	0.007	0.007	0.002
Ni	0.005	0.005	0.004	0.004	0.004	0.004	0.005	0.004	0.003	0.003	0.003	0.003	0.004	0.003	0.003	0.003	0.003	0.002	0.002	0.000
Sum	3.006	3.007	3.007	3.005	3.007	3.007	3.008	3.004	3.008	3.006	2.998	2.999	3.006	3.008	3.005	3.005	3.006	3.007	3.005	0.002
Fo	88.1	87.2	85.4	86.4	86.3	86.5	89.6	87.2	86.0	86.4	86.7	86.5	85.7	83.3	84.0	83.9	84.0	77.8	77.2	0.1

All analyses by University of Hawaii electron microprobe. Total Fe assumed to be Fe^{3+}. Fo (forsterite) content is cationic ratio 100 Mg/(Mg+Fe). Data given as averages on *n* sample analyses with 1 standard deviation (s). Note: * denotes skeletal grains.

Table 2. Plagioclase Compositions - Representative Grains

	29-1		31-1					34-4				36-1		
grain	1		3*		8*		17^	3**		6		6^	2	
region	core	rim	core	rim	core	rim	core	core	rim	core	rim	core	core	rim
n	7	7	4	3	4	3	3	6	2	4	4	3	3	4
Oxides (wt%)														
Na_2O	2.97	2.75	3.42	3.19	3.58	3.80	3.97	1.42	2.75	3.17	3.09	3.56	3.35	3.31
MgO	0.20	0.19	0.18	0.16	0.19	0.19	0.23	0.24	0.22	0.20	0.23	0.24	0.23	0.22
Al_2O_3	31.6	32.0	30.5	30.9	30.2	29.6	29.4	34.2	32.0	31.4	31.2	30.2	30.6	30.5
SiO_2	49.8	49.1	50.7	49.9	51.2	51.8	52.2	46.5	49.5	50.4	50.0	51.1	50.9	50.3
K_2O	0.03	0.03	0.03	0.03	0.04	0.04	0.05	0.01	0.02	0.03	0.04	0.04	0.03	0.03
CaO	14.7	15.1	13.7	14.3	13.6	13.1	12.8	17.5	15.2	14.5	14.6	13.5	13.9	14.0
FeO	0.52	0.60	0.51	0.59	0.55	0.63	0.70	0.33	0.54	0.53	0.53	0.68	0.57	0.59
Total	99.7	99.7	99.0	99.1	99.4	99.2	99.4	100.3	100.3	100.2	99.7	99.4	99.5	99.0
Cations (wt%) based on 8 oxygens														
Na	0.264	0.245	0.305	0.285	0.318	0.338	0.352	0.126	0.243	0.280	0.275	0.317	0.298	0.296
Mg	0.014	0.013	0.012	0.011	0.013	0.013	0.015	0.016	0.015	0.013	0.016	0.016	0.016	0.015
Al	1.703	1.731	1.653	1.680	1.632	1.602	1.583	1.849	1.720	1.683	1.685	1.634	1.650	1.657
Si	2.280	2.252	2.330	2.300	2.346	2.373	2.388	2.136	2.259	2.297	2.290	2.341	2.329	2.319
K	0.002	0.002	0.002	0.002	0.002	0.003	0.003	0.001	0.001	0.002	0.002	0.003	0.001	0.002
Ca	0.719	0.740	0.675	0.704	0.666	0.644	0.629	0.863	0.744	0.707	0.717	0.665	0.680	0.689
Fe	0.020	0.023	0.020	0.023	0.021	0.024	0.027	0.013	0.021	0.020	0.020	0.026	0.022	0.023
Total	5.001	5.005	4.996	5.003	4.998	4.996	4.998	5.003	5.003	5.002	5.006	5.002	4.995	5.001
An	73.0	75.1	68.7	71.1	67.5	65.4	63.9	87.2	75.3	73.4	73.0	67.6	69.5	69.8

	40-2				42-4			43-1				44-1	
grain	5&		2*		6* **		11&	6*		17^^		1**	
region	core	rim	core	rim	core	rim	core	core	rim	core	rim	core	rim
n	5	6	6	5	8	4	4	4	3	4	3	4	4
Oxides (wt%)													
Na_2O	2.67	2.09	1.23	2.08	1.30	1.11	2.89	1.42	2.57	2.67	2.51	1.81	1.69
MgO	0.19	0.25	0.16	0.26	0.38	0.22	0.22	0.23	0.33	0.35	0.31	0.24	0.23
Al_2O_3	32.1	32.8	34.4	32.8	33.9	34.4	31.5	33.7	31.3	31.3	31.7	33.5	33.7
SiO_2	49.2	47.5	45.3	47.5	46.2	45.8	49.2	46.2	49.5	49.3	48.9	47.0	46.6
K_2O	0.02	0.01	0.00	0.01	0.00	0.00	0.02	0.00	0.01	0.01	0.01	0.01	0.00
CaO	15.0	16.1	17.6	16.2	17.8	18.0	15.1	17.2	15.2	15.2	15.4	16.6	16.9
FeO	0.49	0.42	0.31	0.40	0.41	0.38	0.48	0.32	0.50	0.43	0.46	0.38	0.42
Total	99.7	99.1	99.1	99.2	99.9	99.9	99.4	99.1	99.5	99.3	99.3	99.6	99.5
Cations (wt%) based on 8 oxygens													
Na	0.238	0.187	0.111	0.187	0.116	0.100	0.258	0.128	0.229	0.239	0.224	0.162	0.151
Mg	0.013	0.017	0.011	0.018	0.026	0.015	0.015	0.016	0.023	0.024	0.021	0.016	0.016
Al	1.733	1.786	1.886	1.786	1.841	1.871	1.711	1.845	1.698	1.700	1.719	1.823	1.834
Si	2.256	2.197	2.107	2.197	2.131	2.112	2.264	2.142	2.273	2.270	2.254	2.166	2.152
K	0.001	0.000	0.000	0.001	0.000	0.000	0.001	0.000	0.001	0.001	0.000	0.000	0.000
Ca	0.737	0.800	0.879	0.800	0.878	0.891	0.743	0.857	0.750	0.749	0.762	0.823	0.838
Fe	0.019	0.016	0.012	0.016	0.016	0.014	0.019	0.013	0.019	0.016	0.018	0.015	0.016
Total	4.997	5.004	5.006	5.004	5.007	5.003	5.010	5.000	4.993	4.999	4.999	5.004	5.007
An	75.5	81.0	88.8	81.0	88.3	89.9	74.2	87.0	76.5	75.8	77.2	83.5	84.7

All analyses by University of Hawaii electron microprobe. Total Fe assumed to be Fe^{3+}. An (anorthite) content is cationic ratio 100 Ca/(Ca+Na+K). Data given as averages on *n* sample analyses with 1 standard deviation. *=visibly zoned, **=sieve texture, ^=plagioclase +cpx glomophyric intergrowth (glom), ^^=plagioclase +olivine glom, &&=plagioclase glom, &=skeletal.

Table 2. (Continued) Plagioclase Compositions - Representative Grains

	38-2									39-1							
grain	10		6		7^^	2*		4*		12		15^		14&&		8*	
region	core	rim	core	rim	core	core	rim	core	rim	core	rim	core	rim	core	rim	core	rim
n	4	3	4	3	3	4	3	3	3	2	5	3	3	5	5	4	4
Oxides (wt%)																	
Na_2O	3.79	3.68	3.28	3.30	3.12	1.43	2.73	2.91	3.52	1.95	2.94	3.43	3.15	2.11	1.72	2.69	2.17
MgO	0.14	0.20	0.19	0.20	0.20	0.22	0.22	0.15	0.18	0.20	0.25	0.29	0.24	0.19	0.16	0.23	0.19
Al_2O_3	30.1	30.0	30.7	30.6	31.0	33.7	31.6	31.4	30.3	33.2	31.5	30.4	31.1	33.1	33.9	32.2	33.1
SiO_2	51.4	51.7	50.6	51.0	49.9	46.2	49.4	49.4	51.3	47.5	49.8	51.2	50.5	47.9	46.9	49.7	48.1
K_2O	0.04	0.05	0.03	0.04	0.02	0.01	0.01	0.03	0.03	0.02	0.03	0.04	0.04	0.02	0.01	0.02	0.02
CaO	13.3	13.3	14.1	14.0	14.4	17.2	15.0	14.7	13.6	16.5	14.7	13.9	14.5	16.3	17.0	15.5	16.3
FeO	0.59	0.61	0.54	0.57	0.52	0.34	0.52	0.56	0.60	0.38	0.50	0.60	0.56	0.38	0.43	0.47	0.52
Total	99.3	99.6	99.5	99.7	99.2	99.1	99.5	99.3	99.5	99.7	99.8	99.8	100.0	100.0	100.1	100.8	100.4
Cations (wt%) based on 8 oxygens																	
Na	0.336	0.326	0.291	0.292	0.278	0.129	0.243	0.259	0.313	0.174	0.261	0.304	0.279	0.188	0.153	0.236	0.192
Mg	0.010	0.014	0.013	0.014	0.014	0.015	0.015	0.010	0.012	0.013	0.017	0.020	0.016	0.013	0.011	0.015	0.013
Al	1.623	1.615	1.658	1.646	1.680	1.843	1.710	1.705	1.632	1.799	1.699	1.633	1.673	1.790	1.834	1.721	1.782
Si	2.354	2.362	2.320	2.332	2.298	2.143	2.270	2.276	2.346	2.187	2.280	2.338	2.303	2.197	2.155	2.257	2.200
K	0.002	0.003	0.002	0.002	0.001	0.000	0.001	0.002	0.002	0.001	0.002	0.002	0.002	0.001	0.001	0.001	0.001
Ca	0.655	0.652	0.693	0.685	0.711	0.857	0.739	0.728	0.668	0.813	0.723	0.679	0.707	0.801	0.835	0.752	0.799
Fe	0.023	0.023	0.021	0.022	0.020	0.013	0.020	0.022	0.023	0.015	0.019	0.023	0.021	0.014	0.017	0.018	0.020
Total	5.003	4.995	4.998	4.993	5.002	5.000	4.997	5.002	4.996	5.002	5.001	4.999	5.001	5.003	5.005	5.001	5.006
An	65.9	66.5	70.3	70.0	71.8	86.9	75.2	73.6	68.0	82.3	73.3	68.9	71.5	80.9	84.5	76.0	80.5

	48-1						49-1					
grain	10		12*		1*		3*		10*		16^	
region	core	rim	core	rim	core	rim	core	rim	core	rim	core	
n	3	3	3	2	4	3	4	3	4	4	4	σ
Oxides (wt%)												
Na_2O	1.88	2.00	1.48	2.61	2.34	2.10	3.16	2.77	3.20	3.87	3.93	0.03
MgO	0.19	0.21	0.22	0.26	0.23	0.22	0.19	0.18	0.19	0.23	0.22	0.01
Al_2O_3	33.3	33.3	34.3	32.3	32.7	33.2	31.2	31.8	31.1	29.9	29.9	0.08
SiO_2	47.4	48.0	46.5	49.5	48.4	48.1	50.1	49.7	50.6	52.1	52.2	0.10
K_2O	0.00	0.01	0.00	0.02	0.00	0.01	0.03	0.02	0.03	0.04	0.03	0.00
CaO	16.7	16.6	17.6	15.6	16.1	16.5	14.5	15.0	14.4	13.3	13.2	0.07
FeO	0.47	0.50	0.35	0.53	0.44	0.43	0.57	0.63	0.58	0.68	0.72	0.02
Total	99.9	100.6	100.4	100.8	100.2	100.5	99.8	100.1	100.2	100.1	100.1	0.15
Cations (wt%) based on 8 oxygens												
Na	0.168	0.177	0.132	0.230	0.208	0.185	0.280	0.246	0.283	0.341	0.346	0.003
Mg	0.013	0.014	0.015	0.017	0.016	0.015	0.013	0.012	0.013	0.015	0.015	0.001
Al	1.804	1.792	1.853	1.730	1.764	1.787	1.683	1.710	1.672	1.602	1.600	0.003
Si	2.178	2.189	2.132	2.247	2.214	2.195	2.294	2.271	2.305	2.368	2.371	0.003
K	0.000	0.000	0.000	0.001	0.000	0.001	0.002	0.001	0.002	0.002	0.002	0.000
Ca	0.821	0.812	0.863	0.758	0.789	0.805	0.711	0.735	0.704	0.649	0.642	0.003
Fe	0.018	0.019	0.013	0.020	0.017	0.017	0.022	0.024	0.022	0.026	0.027	0.001
Total	5.004	5.004	5.008	5.003	5.008	5.005	5.005	4.998	5.001	5.003	5.003	0.003
An	83.0	82.1	86.7	76.7	79.1	81.2	71.6	74.9	71.2	65.4	64.8	0.25

All analyses by University of Hawaii electron microprobe. Total Fe assumed to be Fe^{3+}. An (anorthite) content is cationic ratio 100 Ca/(Ca+Na+K). Data given as averages on *n* sample analyses with 1 standard deviation (σ). *=visibly zoned, **=sieve texture, ^=plagioclase +cpx glomglomophyric intergrowth (glom), ^^=plagioclase +olivine glom, &&=plagioclase glom, &=skeletal.

using San Carlos olivine (Si and Mg), Verma garnet (Mn), diopside (Ca), magnetite (Fe) and Ni-oxide metal (Ni) for calibration. Peak counting times were 60 s for Mg, Si, Ni and Ca and 30 s for Fe and Mn. Background counting times were 30 s for Mg, Si, Ni and Ca and 15 s for Fe and Mn. Accepted data have oxide totals between 98.5 and 101.0 wt % and cation totals between 3.01 and 2.99 per 4 oxygens for olivine and 5.01 and 4.99 per 8 oxygens for plagioclase. Standard deviations for olivine and plagioclase were calculated from repeat analyses of San Carlos and Spring Water olivines, and Lake County plagioclase, respectively. Analytical procedures for glass analyses by microprobe were reported in Cushman et al (2004).

Major, minor, and trace element compositions were measured for 27 whole-rock samples by XRF using the University of Hawai‘i Siemens 303AS spectrometry system with a Rh-target, end-window X-ray tube (Table 3). Samples were crushed to a 5 mm size fraction, hand inspected to avoid alteration, and crushed in an alumina swing mill. Powders were analyzed for major and minor elements on fused disks following methods similar to those of Norrish and Hutton (1977). Trace elements were analyzed on pressed powder pellets. Peak intensities for the trace elements were corrected for backgrounds, line interferences and matrix absorption using methods similar to Chappell (1992). Corrected intensities were calibrated against a wide range of natural rock standards. Standard deviations for major elements were calculated from analyses of rock standards run as unknowns with our samples (12 major element analyses of standard basalt W-1 and three trace element analyses of BHVO-1).

ICPMS and isotopic analyses (Table 4) were obtained for fresh basaltic glass, crushed to a 350-710 µm size fraction, and hand picked under binocular microscope

Table 3. Galápagos Spreading Center - Whole Rock XRF Data

Sample	29-1	31-1	32-2	33-1	34-1	34-4	35-1	38-2	39-1	40-2	41-1	41-5	41-7	42-4	43-1	45-2	47-1	48-4	49-1	50-1	51-1	53-1	σ
latitude (˚N)	2.202	2.244	2.267	2.281	2.290	2.29	2.301	2.358	2.340	2.325	2.313	2.313	2.313	2.393	2.412	2.444	2.464	2.488	2.500	2.500	2.510	2.510	-
longitude (˚W)	92.618	92.822	92.882	92.973	93.010	93.01	93.049	93.269	93.218	93.160	93.094	93.094	93.094	93.205	93.256	93.353	93.563	93.655	93.869	93.776	93.962	94.127	-
SiO_2	50.9	50.9	50.7	51.2	50.8	50.4	51.4	50.4	51.2	49.8	50.9	51.2	50.6	51.4	50.2	50.3	51.7	50.9	50.7	50.9	50.8	51.2	0.11
TiO_2	1.65	1.77	1.65	1.59	1.43	1.49	1.71	1.57	1.37	0.93	1.35	1.29	1.26	0.90	0.93	1.25	1.67	1.68	1.71	1.36	1.23	1.78	0.02
Al_2O_3	14.3	14.0	13.8	13.9	14.7	14.5	14.2	14.1	15.0	15.8	14.4	14.7	14.7	15.2	15.0	14.9	14.4	14.2	13.7	14.8	14.9	13.7	0.14
FeO*	12.2	13.0	12.8	13.0	11.6	11.9	12.8	12.1	11.1	9.5	11.6	11.5	11.2	10.0	9.4	10.9	12.6	12.5	13.0	10.9	10.6	13.3	0.05
MnO	0.20	0.21	0.20	0.21	0.19	0.20	0.21	0.20	0.18	0.17	0.19	0.19	0.19	0.17	0.16	0.18	0.20	0.20	0.22	0.18	0.18	0.21	0.01
MgO	6.95	6.71	6.94	6.76	7.45	7.21	6.40	7.20	7.33	8.96	7.55	7.73	7.85	8.21	8.75	8.65	6.44	6.88	6.57	7.94	7.97	6.58	0.03
CaO	11.4	11.0	11.4	11.1	11.9	11.8	11.3	11.5	12.2	13.1	11.9	12.2	12.3	13.3	13.4	11.8	11.3	11.4	11.0	12.4	12.4	10.8	0.06
Na_2O	2.22	2.31	2.05	2.56	2.09	1.92	2.37	2.38	2.04	1.53	1.90	1.99	1.89	1.39	1.54	2.37	2.24	2.17	2.61	1.97	1.84	2.27	0.11
K_2O	0.19	0.21	0.15	0.17	0.14	0.14	0.16	0.15	0.16	0.05	0.14	0.12	0.12	0.06	0.04	0.11	0.18	0.18	0.21	0.14	0.08	0.16	0.01
P_2O_5	0.16	0.15	0.14	0.15	0.13	0.13	0.15	0.15	0.13	0.07	0.11	0.11	0.10	0.07	0.07	0.11	0.16	0.15	0.16	0.11	0.09	0.15	0.01
Sum	100.2	100.3	99.8	100.7	100.4	99.6	100.7	99.8	100.6	99.9	100.0	100.9	100.2	100.8	99.6	100.6	100.9	100.1	100.0	100.7	100.1	100.2	-
LOI	-0.43	-0.61	-0.49	-0.66	-0.84	-0.62	-0.54	-0.65	-0.42	-0.37	-0.57	-0.48	-0.38	-0.39	-0.56	-0.45	-0.62	-0.58	-0.40	-0.42	-0.83	-0.52	-
Sc	48	47	49	44	48	47	50	45	49	44	50	50	50	48	48	43	49	48	43	49	49	47	1
V	378	408	420	412	359	371	408	386	352	265	379	353	357	322	307	301	411	415	420	351	341	424	1
Cr	94	55	122	52	225	208	51	201	268	439	206	225	259	356	338	382	97	95	66	315	285	61	2
Co	47	48	48	49	49	49	45	46	46	50	49	49	48	48	48	50	45	47	45	49	46	49	1
Ni	58	51	58	54	88	82	51	79	88	152	84	88	92	110	98	158	58	58	53	89	80	51	1
Zn	103	117	110	110	98	96	109	101	91	69	96	93	89	77	72	88	107	108	113	91	87	118	1
Rb	4.4	5.5	4.1	4.1	4.1	3.6	4.3	3.9	4.3	1.8	3.8	3.6	3.5	2.1	1.5	3.3	5.2	4.4	4.5	4.0	2.9	4.3	0.2
Sr	98	109	85	85	93	91	100	82	105	82	79	79	76	59	63	79	98	95	89	94	87	85	0.2
Y	36	41	37	36	33	33	39	36	30	22	32	31	30	22	21	28	39	36	39	30	31	43	0.1
Zr	93	108	93	88	83	83	101	89	80	48	75	72	68	43	43	66	100	98	99	75	73	109	0.5
Nb	6.8	8.6	6.4	6.6	6.3	6.4	6.4	6.0	7.4	3.7	5.5	5.4	4.8	2.8	2.0	4.2	8.0	7.4	7.2	6.2	4.0	6.8	0.3
Ba	13	39	-10	-11	29	10	22	-11	29	-9	-12	19	-10	-10	-10	-11	29	22	21	21	-14	22	7

negative values = < value (detection limit). One sigma values (σ) were calculated from analyses of rock standards run as unknowns with our samples (12 major element analyses of standard basalt W-1 and three trace element analyses of BHVO-1)

Table 4. Galápagos Spreading Center - Natural Glass Trace Element and Isotope Data

Sample	29-1*	31-1	32-2	33-1	34-1	34-4	35-1	35-2	36-1	37-4	38-2*	39-1	39-2	40-2
latitude	2.202	2.244	2.267	2.281	2.290	2.290	2.301	2.301	2.444	2.393	2.358	2.340	2.340	2.325
longitude	92.618	92.822	92.882	92.973	93.010	93.010	93.049	93.049	93.432	93.353	93.269	93.218	93.218	93.160
Ni	47.23	43.07	53.98	47.66	67.84	64.68	43.68	42.49	59.74	57.28	48.90	73.48	46.27	113.14
Rb	4.70	4.62	3.82	3.92	3.55	3.64	3.53	3.69	3.94	2.82	3.50	3.99	4.17	1.72
Sr	93.77	106.37	87.46	87.46	93.51	93.14	98.58	99.18	94.60	84.31	81.01	104.70	97.76	82.93
Y	38.14	41.85	40.72	39.40	36.65	37.40	40.90	41.78	37.79	32.06	32.33	32.75	38.92	24.84
Zr	-	106.54	-	107.01	84.83	86.58	100.62	103.04	92.34	69.81	86.87	80.88	96.63	50.50
Nb	8.15	8.26	6.81	6.87	6.47	6.57	6.49	6.79	7.13	5.17	6.29	7.41	7.57	3.11
Cs	0.04	0.05	0.04	0.04	0.04	0.04	0.04	0.04	0.04	0.03	0.06	0.04	0.05	0.02
Ba	46.71	50.69	39.59	41.90	38.48	39.62	37.90	39.56	41.99	31.66	40.55	44.34	39.81	21.03
La	5.56	5.99	5.02	5.00	4.73	4.82	4.99	5.19	5.15	3.88	5.12	5.11	5.44	2.57
Ce	13.63	15.17	12.92	12.67	12.02	12.27	13.14	13.63	12.97	9.90	13.48	12.50	13.76	6.82
Pr	2.27	2.37	2.07	2.02	1.92	1.94	2.14	2.21	2.05	1.58	2.18	1.91	2.16	1.12
Nd	11.05	12.15	10.77	10.48	9.91	10.05	11.14	11.46	10.49	8.23	10.91	9.57	11.03	5.97
Sm	3.31	4.01	3.63	3.53	3.33	3.37	3.72	3.83	3.47	2.83	3.68	3.07	3.61	2.12
Eu	1.16	1.36	1.23	1.21	1.15	1.15	1.27	1.30	1.17	1.01	1.26	1.07	1.24	0.79
Gd	4.18	4.78	4.41	4.32	4.10	4.14	4.52	4.64	4.21	3.54	5.07	3.77	4.36	2.70
Tb	0.87	0.94	0.89	0.86	0.81	0.82	0.89	0.92	0.83	0.70	0.94	0.74	0.86	0.54
Dy	5.35	6.41	6.11	5.97	5.56	5.63	6.15	6.31	5.69	4.84	6.01	4.98	5.83	3.75
Ho	1.28	1.41	1.35	1.33	1.24	1.25	1.36	1.39	1.25	1.08	1.31	1.10	1.29	0.84
Er	3.32	4.17	4.01	3.95	3.66	3.71	4.02	4.12	3.70	3.17	3.75	3.25	3.80	2.49
Tm	0.51	0.67	0.65	0.63	0.59	0.59	0.64	0.66	0.59	0.51	0.59	0.52	0.61	0.40
Yb	3.43	4.07	3.95	3.90	3.61	3.64	3.93	4.03	3.63	3.10	-	3.16	3.71	2.43
Lu	0.55	0.62	0.60	0.60	0.55	0.56	0.60	0.62	0.55	0.47	0.62	0.48	0.57	0.37
Hf	2.37	2.86	-	2.89	2.35	2.38	2.68	2.77	2.48	1.94	2.55	2.16	2.60	1.41
Ta	0.43	0.51	0.41	0.42	0.39	0.40	0.39	0.41	0.43	0.31	0.42	0.44	0.46	0.19
Pb	0.52	0.55	0.48	0.55	0.45	0.48	0.54	-	0.50	0.40	0.57	0.47	0.56	0.30
Th	0.53	0.60	0.50	0.50	0.48	0.48	0.47	0.49	0.51	0.38	0.48	0.54	0.55	0.24
U	0.14	0.17	0.14	0.14	0.13	0.13	0.13	0.14	0.14	0.10	0.13	0.15	0.15	0.06
ε Nd	7.30			7.2					7.2		7.40	6.8		
$^{143}Nd/^{144}Nd$	0.513015			0.513009					0.513010		0.513018	0.512989		
$^{87}Sr/^{86}Sr$	0.70294			0.70300					0.70300		0.70301	0.70304		
$^{206}Pb/^{204}Pb$	18.9230			-					18.8722		18.7940	19.0048		
$^{207}Pb/^{204}Pb$	15.566			-					15.577		15.563	15.592		
$^{208}Pb/^{204}Pb$	38.675			-					38.684		38.620	38.827		

*Trace element data collected with the University of Hawaii's V6 Plasma Quad II by William Chazey, otherwise collected as part of this study on the University of Hawaii's Element2. Isotope analyses for samples 29-1, 38-2, 41-1, 45-2, 48-4 and 49-1 were collected by William Chazey. All analyses were collected using the University of Hawaii's V6 Sector TIMS. One sigma values (σ) for ICPMS analyses are based on six K1919 analyses. Data are reported relative to the measured value of $^{87}Sr/^{86}Sr$=0.710239 +/- 0.000016 (n = 34) for NBS 987 Sr standard, to $^{143}Nd/^{144}Nd$=0.511845 +/- 0.000010 (n = 18) for La Jolla Nd standard, and to the Pb isotope values of $^{206}Pb/^{204}Pb$ = 16.9406 +/- 0.0006, $^{207}Pb/^{204}Pb$ = 15.4974 +/- 0.0010, $^{208}Pb/^{204}Pb$ = +/- 0.0022 (n = 21) for NBS 981 Pb standard. All uncertainties listed above are 2σ. For Nd, Sr, and Pb isotope ratios, precision on all of the sample measurements is as good as or better than the external uncertainties on standards with the exception of sample 44-1 which has 2σ uncertainties as follows: $^{206}Pb/^{204}Pb$ +/- 0.0029, $^{207}Pb/^{204}Pb$ +/- 0.0033, $^{208}Pb/^{204}Pb$ +/- 0.0060.
The fractionation correction for Nd is 148NdO/144NdO = 0.242436 (148Nd/144Nd = 0.241572). The correction for Sr is 86Sr/88Sr = 0.1194.

Table 4. (Continued) Galápagos Spreading Center - Natural Glass Trace Element and Isotopic Data

Sample	41-1*	41-7*	42-4	43-1	44-1	45-2*	46-1	47-1	48-1	48-4	49-1*	50-1	51-1	53-1	σ
latitude	2.313	2.313	2.393	2.412	2.420	2.444	2.453	2.464	2.488	2.488	2.500	2.500	2.510	2.510	-
longitude	93.094	93.094	93.205	93.256	93.296	93.353	93.492	93.563	93.655	93.655	93.869	93.776	93.962	94.127	-
Ni	79.02	71.98	98.62	86.42	149.75	144.37	71.98	50.15	85.17	45.00	54.81	79.03	68.45	41.24	0.84
Rb	3.26	2.48	1.48	1.19	2.08	2.57	2.95	4.31	2.61	3.75	4.08	3.68	2.19	3.99	0.01
Sr	77.72	72.45	60.90	67.26	74.32	76.31	84.69	97.95	83.23	92.67	84.79	97.16	86.26	85.68	0.96
Y	33.29	-	22.91	23.48	28.20	28.70	30.53	39.95	30.91	30.77	40.07	32.16	33.47	48.45	0.09
Zr	74.94	59.18	41.46	47.41	58.67	62.51	80.02	99.42	81.53	90.72	99.01	76.04	78.17	115.04	7.57
Nb	5.63	4.36	2.69	2.19	3.93	4.34	5.19	7.71	3.41	6.95	7.05	6.44	3.78	7.11	0.10
Cs	0.05	0.04	0.02	0.01	0.02	0.04	0.03	0.05	0.03	0.06	0.06	0.04	0.03	0.04	0.001
Ba	33.62	29.46	17.74	14.88	22.87	25.56	32.10	45.12	24.06	45.90	40.45	40.38	24.25	38.72	1.10
La	4.35	3.56	2.18	1.95	3.03	3.43	3.81	5.57	2.94	5.51	5.51	4.59	3.33	5.48	0.15
Ce	11.19	9.34	5.71	5.50	7.95	8.95	9.61	14.04	8.36	14.16	14.30	11.31	9.08	14.39	0.38
Pr	1.74	1.51	0.94	0.94	1.29	1.45	1.53	2.20	1.43	2.27	2.18	1.74	1.52	2.34	0.06
Nd	9.21	7.58	4.99	5.21	6.76	7.46	7.88	11.22	7.52	11.14	11.60	8.82	8.07	12.30	0.30
Sm	3.00	2.61	1.81	1.92	2.35	2.63	2.67	3.65	2.68	3.61	3.81	2.91	2.83	4.18	0.08
Eu	1.06	0.94	0.69	0.73	0.84	0.96	0.94	1.24	0.95	1.30	1.29	1.02	1.00	1.37	0.02
Gd	4.22	3.65	2.46	2.55	3.02	3.56	3.31	4.43	3.47	4.93	4.89	3.57	3.57	5.06	0.08
Tb	0.78	0.69	0.50	0.52	0.61	0.70	0.66	0.87	0.69	0.91	0.96	0.71	0.72	1.02	0.01
Dy	5.29	4.50	3.40	3.53	4.21	4.51	4.55	5.97	4.77	5.84	5.83	4.84	4.98	7.08	0.08
Ho	1.19	0.98	0.77	0.79	0.95	1.04	1.01	1.32	1.05	1.26	1.43	1.07	1.11	1.56	0.01
Er	3.31	2.90	2.30	2.34	2.84	2.84	3.00	3.91	3.17	3.65	3.89	3.14	3.30	4.71	0.04
Tm	0.54	0.46	0.37	0.37	0.46	0.45	0.48	0.62	0.52	0.56	0.64	0.50	0.53	0.76	0.01
Yb	3.55	3.03	2.28	2.29	2.82	2.99	2.93	3.80	-	3.75	3.92	3.06	3.23	4.62	0.04
Lu	0.56	0.49	0.36	0.35	0.44	0.46	0.45	0.58	0.49	0.59	0.66	0.47	0.49	0.71	0.01
Hf	2.24	1.77	1.19	1.34	1.64	1.93	2.15	2.67	2.22	2.62	2.84	2.06	2.14	3.13	0.19
Ta	0.37	0.29	0.16	0.14	0.24	0.28	0.31	0.46	0.21	0.47	0.44	0.38	0.24	0.43	0.01
Pb	0.45	0.37	0.30	0.28	0.34	0.37	0.42	0.53	0.16	-	0.59	0.45	0.44	0.54	0.01
Th	0.37	0.33	0.20	0.16	0.29	0.29	0.39	0.57	0.24	0.53	0.44	0.49	0.30	0.54	0.01
U	0.11	0.09	0.05	0.04	0.08	0.09	0.10	0.16	0.07	0.15	0.13	0.13	0.08	0.14	0.003
ε Nd		7.40		8.1	7.5	7.60				7.30	7.30				0.1
$^{143}Nd/^{144}Nd$		0.513018		0.513057	0.513026	0.513032				0.513014	0.513012				0.000005
$^{87}Sr/^{86}Sr$		0.70307		0.70287	0.70302	0.70287				0.70294	0.70294				0.000008
$^{206}Pb/^{204}Pb$		18.8560		18.6806	18.8540	18.8910				18.8600	18.8350				0.0003
$^{207}Pb/^{204}Pb$		15.564		15.557	15.568	15.567				15.573	15.568				0.0005
$^{208}Pb/^{204}Pb$		38.667		38.453	38.637	38.673				38.697	38.654				0.0011

*Trace element data collected with the University of Hawaii's V6 Plasma Quad II by William Chazey, otherwise collected as part of this study on the University of Hawaii's Element2. Isotope analyses for samples 29-1, 38-2, 41-1, 45-2, 48-4 and 49-1 were collected by William Chazey. All analyses were collected using the University of Hawaii's V6 Sector TIMS. One sigma values (σ) for ICPMS analyses are based on six K1919 analyses. Data are reported relative to the measured value of $^{87}Sr/^{86}Sr$=0.710239 +/- 0.000016 (n = 34) for NBS 987 Sr standard, to $^{143}Nd/^{144}Nd$=0.511845 +/- 0.000010 (n = 18) for La Jolla Nd standard, and to the Pb isotope values of $^{206}Pb/^{204}Pb$ = 16.9406 +/- 0.0006, $^{207}Pb/^{204}Pb$ = 15.4974 +/- 0.0010, $^{208}Pb/^{204}Pb$ = +/- 0.0022 (n = 21) for NBS 981 Pb standard. All uncertainties listed above are 2σ. For Nd, Sr, and Pb isotope ratios, precision on all of the sample measurements is as good as or better than the external uncertainties on standards with the exception of sample 44-1 which has 2σ uncertainties as follows: $^{206}Pb/^{204}Pb$ + 0.0029, $^{207}Pb/^{204}Pb$ + 0.0033, $^{208}Pb/^{204}Pb$ + 0.0060.

The fractionation correction for Nd is $^{148}NdO/^{144}NdO$ = 0.242436 ($^{148}Nd/^{144}Nd$ = 0.241572). The correction for Sr is $^{86}Sr/^{88}Sr$ = 0.1194.

magnification to eliminate alteration and phenocryst phases. Picked glasses were rinsed with ethanol to remove organic surface contaminants and leached with ~1N HCl in a sonic bath for 5 minutes. For each sample, ~ 50 mg of cleaned glass chips were weighed and subsequently digested with an HF-HNO_3 (1:2) acid solution. Samples then underwent four successive dry downs, the first with 6N HCl to help break down calcium-fluoride precipitates, followed by three washes in ~8N HNO_3 to remove residual Cl and F. Samples were then diluted with ~12 ml of 4N HNO_3, from which subsequent dilutions were made for analysis on the ICPMS instrument.

Natural glass was analyzed for a range of trace elements in seventeen samples using the University of Hawai‘i Thermo-Finnigan Element2 ICPMS. Trace element concentrations were determined by external calibration with USGS standards BIR-1, W-2, BHVO-1 and BCR-1. Two dilutions of each standard were analyzed at the beginning and end of the ICPMS run resulting in a 16 point calibration curve (Pyle et al., 1995). A University of Hawai‘i in-house standard, K1919 (similar to BHVO-1), was analyzed after every fifth sample to monitor possible instrument drift not accounted for by the 1 ppb internal standards (Be, In, Tl, Bi) added to each sample and standard. Because the K1919 results varied with analytical uncertainty of known concentrations, sample data were not normalized to our K1919 reference values. Repeat analyses of K1919 are good indicators of analytical uncertainty and run-to-run precision. Separate dissolutions of BHVO-1 and BIR-1 were also treated as unknowns (i.e., not used in the standard calibration curves) as a further assessment of accuracy of the analyses. Two samples were picked, dissolved and analyzed in duplicate to assess procedural error and variation in glass picking procedure. In addition, we re-analyzed three previously analyzed samples with newly

picked glass to assess differences arising from slight procedural differences and the use of a different analytical instrument, the VG Plasma Quad II mass spectrometer at the University of Hawaii. All tests show the analyses reported here to be within analytical error. Errors for each element are reported as one standard deviation (Table 4) and range from 0.3% to 3.4% of that element's average abundance with the exception of Zr, for which the uncertainty is 9.2% and Hf, for which it is 8.5%. Analyses which yielded results which were not deemed reliable are not reported.

Strontium, Neodymium, and Lead isotopic data (Table 4) were collected on a subset of five hand-picked phenocryst-free glass samples by thermal ionization mass spectrometry (TIMS) using the VG Sector mass spectrometer at the University of Hawai'i. Procedures followed were those of Mahoney et al. (Pb isotope analyses e.g. Mahoney 1991, 1992, and Ishikawa 2005), except that the double-spike Pb isotope analyses were made in multi-dynamic mode rather than multi-static mode.

3. Results

3.1 Petrography

Modal phenocryst abundances were determined by collecting 2000-point counts on four samples spanning the range of modal abundances and visually estimating the remainder relative to the point-counted samples (Table 5). Minerals <0.05 mm across were assumed to have crystallized after eruption and are here considered "groundmass". Lavas recovered from the 93.25˚W OSC study area are tholeiitic pillow and sheet flows ranging in total phenocrysts from <1 to 16 %. The phenocryst assemblage for all samples is plagioclase ± olivine ± clinopyroxene with plagioclase being the most abundant

Table 5. Mineral Modes (%)

	Propagating Limb											Overlapping Propagating Limb					Overlapping Doomed Limb				Doomed Limb								
sample	29-1*	31-1*	32-2	33-1	34-1	34-4*	35-1	35-2	41-1	41-5	41-7	40-2*	39-1*	39-2	38-2*	37-4	42-4*	43-1*	44-1*	45-2	36-1*	46-1	47-1	48-1*	48-4	50-1	49-1*	51-1	53-1
longitude	92.62	92.82	92.88	92.97	93.01	93.01	93.05	93.05	93.09	93.09	93.09	93.16	93.22	93.22	93.27	93.35	93.20	93.26	93.30	93.35	93.43	93.49	93.56	93.66	93.66	93.78	93.87	93.96	94.13
MgO	6.8	6.4	6.8	6.7	7.2	7.0	6.5	6.4	7.3	7.6	7.7	8.7	7.4	6.5	6.7	7.3	8.8	8.7	8.6	8.1	7.1	7.9	6.7	8.1	6.7	7.8	6.6	7.7	6.1
plag	2	2.65	3.9	4	7	8	6	5	4	4	4	9	6	9	8.55	7	2	4	<1	1	1.32	1	3	3	4	1	2	8	8
olivine	<<1	0.75	0.7	<1	3	3	2	2	2	1	1	3	1	2	1.70	2	1	2	<1	2	0.88	<1	1	<1	2	<1	1	3	2
cpx	1	0.85	1.6	3	0	0	0	0	1	<1	<1	<1	3	3	5.75	1	<<1	1	0	0	0	1	0	0	<1	0	2	<1	4
vessicles	2	2.65	1.6	1	0	<1	1	2	<1	<1	<1	1	1	<1	3.20	1	<1	1	0	<1	0	<1	<1	<1	<1	<1	2	0	<1

Samples 31-1, 32-2, 38-2 and 36-1 were determined by 2000-point counts, the remaining samples were determined visually. Glass and matrix account for the remaining modal assemblage to attain 100%. Samples indicated by an asterix have plagioclase and olivine data as well as a detailed petrographic description. plag = plagioclae, cpx = clinopyroxene, MgO content is of the glass and is given as weight percent.

phenocryst phase in most cases. Olivine ranges in texture from highly skeletal to euhedral and tends to be <1.3 mm. Plagioclase is commonly visibly zoned; several samples contain large plagioclase grains (2.6 mm) with sieve (partial dissolution) texture, a common disequilibrium texture indicating a complex crystallization history, possibly affected by magma mixing (Figure 3). Clinopyroxene is more prevalent in more evolved rocks and dominantly occurs as small anhedral grains in glomophyric intergrowths with plagioclase laths, and rarely as isolated phenocrysts. A description of each thin section in which olivine and plagioclase data were collected is presented in Appendix B.

3.2. Mineral Chemistry

Olivine and plagioclase compositions for both cores and rims were determined for a suite of 12 samples. Six samples were chosen from within the overlapping region of the ridge (OPR and ODR) and six samples from outside the overlap zone (PR and DR). Results are reported as an average of at least two analyses. Appendices C and D contain a complete data set of probed olivine and plagioclase compositions, respectively.

Olivine occurs as non-zoned grains, as well as normally or reversely zoned varieties with cores and rims spanning a range of mol. % forsterite (Fo) from 76.8 to 90. Each sample contains from one to three representative types of olivine (Table 1). Olivine Fo content generally increases with Mg# {atomic $Mg/(Mg+Fe^{2+}) \times 100$} of the host glass, although variation of up to 5.5 mol % Fo can occur within individual samples (Figure 4). We calculated glass Mg# assuming $Fe^{3+}/\Sigma Fe = 0.1$, a value intermediate between those of Christie et al. (1986) (0.07 ± 0.03) and Bezos and Humler (2005) (0.12 ± 0.02). Olivine Fo compositions fall mostly within the bounds of predicted equilibrium with distribution

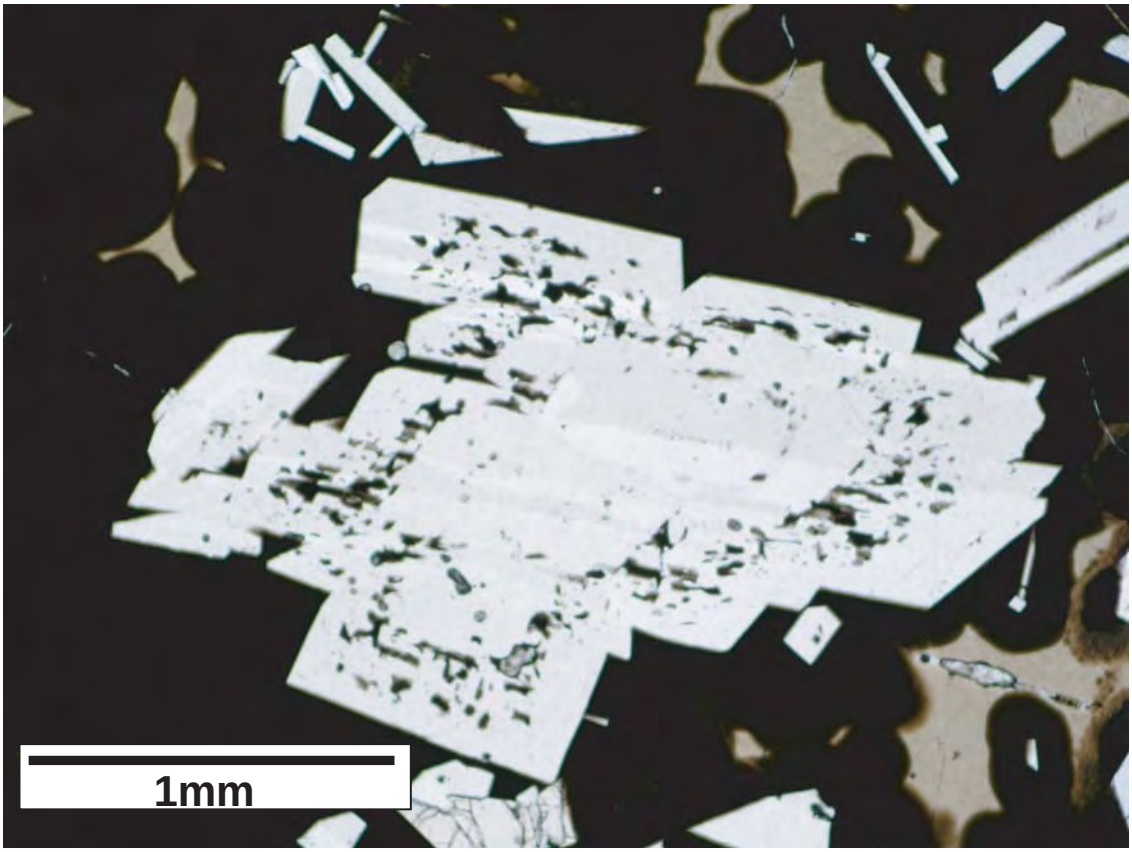

Figure 3. Photomicrograph of a plagioclase grain in sample 34-4 displaying sieve texture; black and brown patches are glass. Plagioclase grain is 2.6 mm long. This texture indicates partial melting of an early-formed crystal, subsequently overgrown by a plagioclase rim.

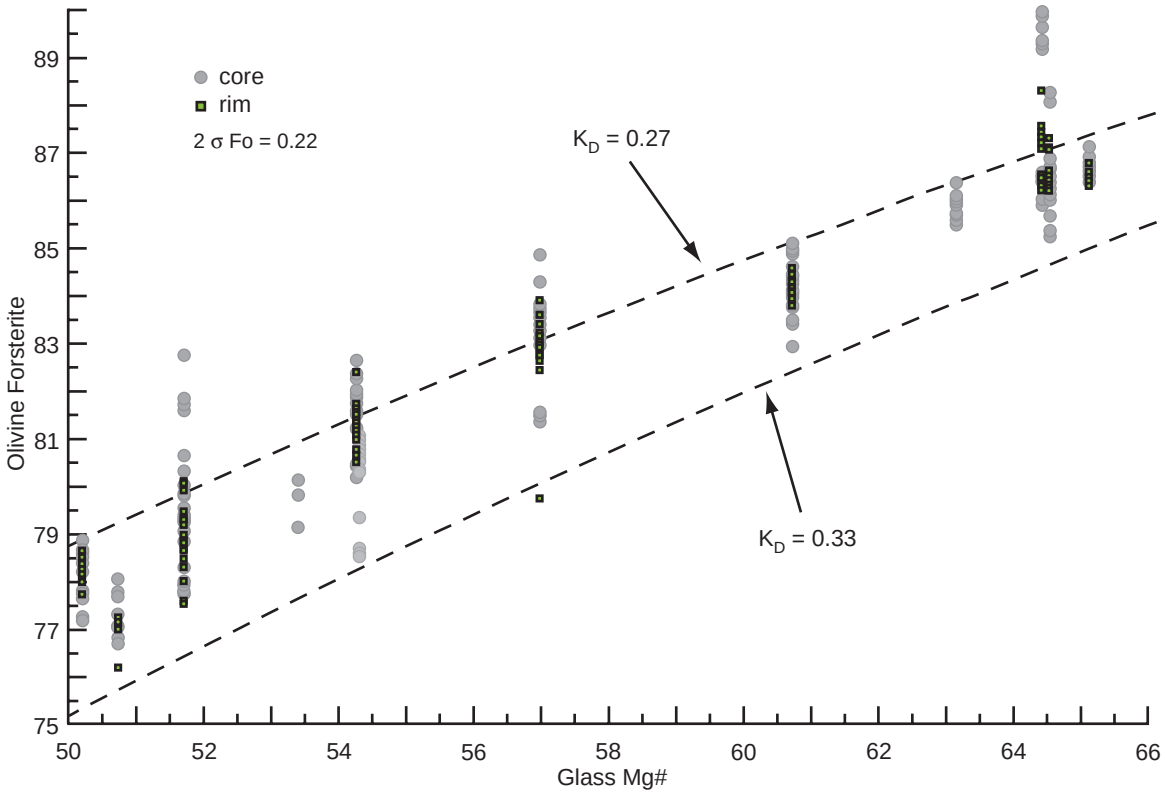

Figure 4. Olivine core and rim forsterite (Fo) compositions compared to the Mg# (atomic Mg/[Fe^{2+} + Mg] x 100) of its glass. Ferrous iron (Fe^{2+}) is assumed to be 10% of total iron as FeO*. Area between hatched lines shows the range of equilibrium olivine compositions for a given Mg# of glass with Fe/Mg K_D of 0.30 +/- 0.03 (based on Roeder and Emslie, 1970). Most olivine is in equilibrium with the melt with systematic deviations toward more Fo-rich olivine suggesting the melt continues to evolve faster than growth through clinopyroxene crystalization or that there is subsolidus equilibration of olivine crystals. Representative olivine analyses are given in Table 1. Core analyses were determined for the interior of the grain, rim analyses for the exterior of the grain, grains are not necessarily chemically or visibly zoned. $K_D=(XFeO_{ol}/XFeO_{liq})x(XMgO_{ol}/XMgO_{liq})$.

coefficient $K_D = 0.30 \pm 0.03$ (Roeder and Emslie, 1970) (Figure 4). Five samples contain olivine grains with Fo contents higher than expected for equilibrium; all are from the overlapping region of the study area, with the exception of 34-4 which is from the propagating limb.

Plagioclase compositions range from 62.3 to 91.8 mol. % anorthite (An); both normally and reversely zoned plagioclase grains are present. Although some samples contain relatively uniform plagioclase textural types and a limited compositional range, others are more complex, both texturally and compositionally (Table 2, Figure 5). The most widely varying samples occur near or within the overlapping region and these samples tend to have two compositional populations, based on An contents. The lowest An plagioclase grains occur in glomeroporphyritic clusters with clinopyroxene or olivine. The highest An contents occur in samples near or within the overlapping region of the study area.

Equilibrium plagioclase compositions for each host glass were calculated using the MELTS and Adiabat_1ph algorithms (Ghiorso and Sack, 1995; Smith and Asimow, 2005), at pressures of 500 to 2000 bars (Appendix E). This pressure range encompasses AMC depths of 2500-5000 $\pm$ 400 meters below seafloor observed from multichannel seismic imaging (Blacic et al., 2002) and is equivalent to 925-1635 $\pm$ 145 bars pressure assuming a 2215 $\pm$ 295 m water depth, a crustal density of 2900 kg/m^3 and lithostatic pressure. The greatest deviations from predicted equilibrium are shown by samples from within the overlap zone and along the doomed limb. The 145 bar uncertainty in pressure corresponds to a 0.1 mol. % An difference in predicted plagioclase equilibrium. Sample 42-4, at the tip of the doomed limb, contains the most calcic grains, with some cores and

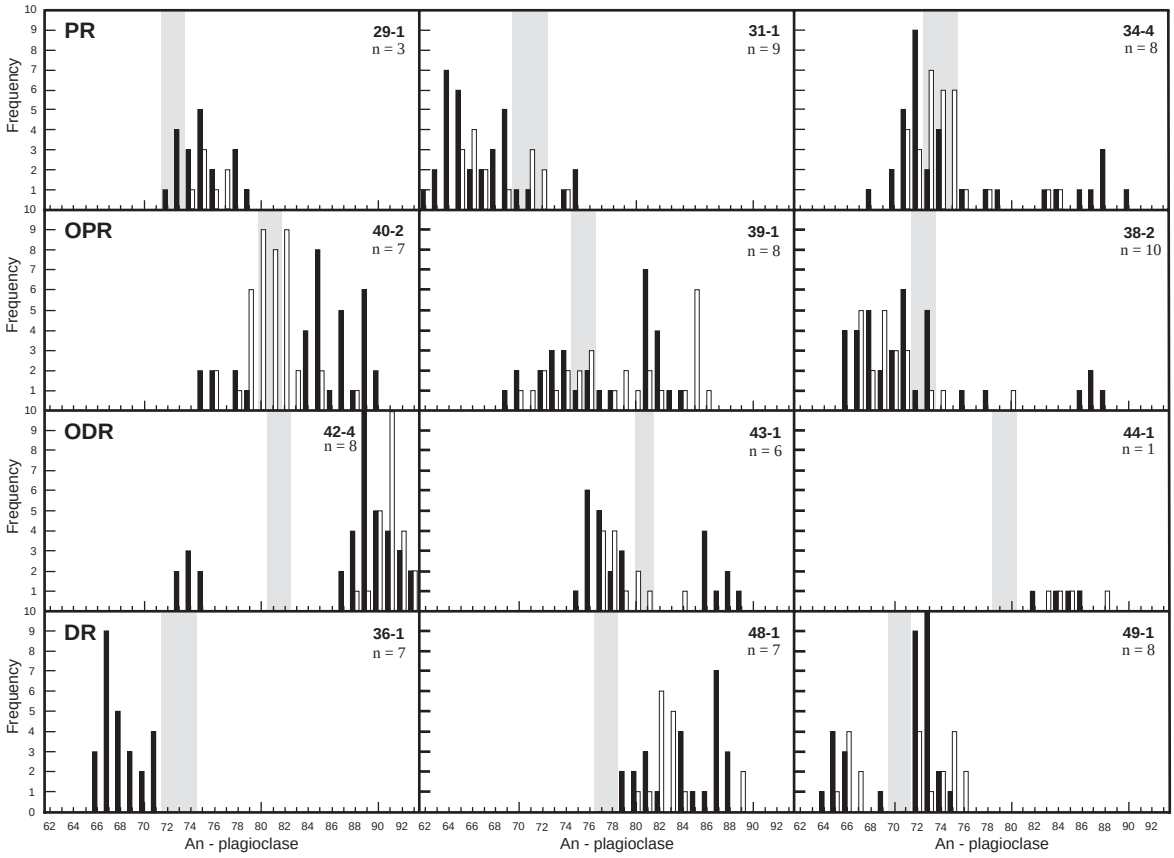

Figure 5. Histograms of plagioclase anorthite (An) content for the four regions of the study area. Cores = black bars, rims = white bars. Shaded bars denotes equilibrium compositions predicted by MELTS (Ghiorso and Sack, 1995; Smith and Asimow, 2005) for each host glass composition (from Cushman et al., 2004) at pressures of 500 to 2000 bars. Each sample's glass composition, including water content, was used as the starting liquid composition for the model run (Cushman et al., 2004). For those sampes lacking H_2O data, $H_2O$was assumed to be 0.25 wt% (analyzed samples contain 0.10 to 0.31 wt% H_2O). n refers to the number of grains analyzed. Core analyses were determined for the interior of the grain, rim analyses for the exterior of the grain, grains are not necessarily chemically or visibly zoned. MELTS outputs are displayed in Appendix E.

rims between 87 and 92 mol. % An, including one sieve textured grain. The calculated equilibrium composition for sample 42-4 is much lower, at 81-83 mol. % An. The core of the sieve-textured plagioclase of 34-4 is much more calcic than its rim (87 mol. % An core, 75 mol. % An rim) or other plagioclase grains in the sample, which are close to the calculated equilibrium composition for the enclosing glass (73-76 mol. % An, Figure 5). For all samples, plagioclase that occurs in glomeroporphyritic clusters with clinopyroxene or olivine tends to be much less calcic than grains with any other texture.

3.3. Trace Element Compositions

Natural glass trace element compositions were determined by ICPMS for one sample from each geochemical group defined by Cushman et al. (2004). Primitive-mantle-normalized plots of natural glass incompatible trace element compositions show that lavas from the ODR differ from other lavas in the study area, with the exception of sample 40-2 on the propagating limb (Figure 6). ODR lavas have overall lower incompatible element abundances, consistent with their higher MgO concentrations, which indicate less overall differentiation; many of these samples also have less pronounced troughs at Sr on mantle-normalized diagrams, suggesting that Sr depletion can be explained by plagioclase fractionation. The patterns for samples 43-1 and 42-4 cross, indicating that they cannot be related simply by different degrees of differentiation from a common parental magma. Lavas from the DR are similar to those of the PR and OPR but have slightly higher abundances of heavy rare earth elements (REE). Flatter values of heavy REEs in PR and OPR samples, which are from sites closer to the

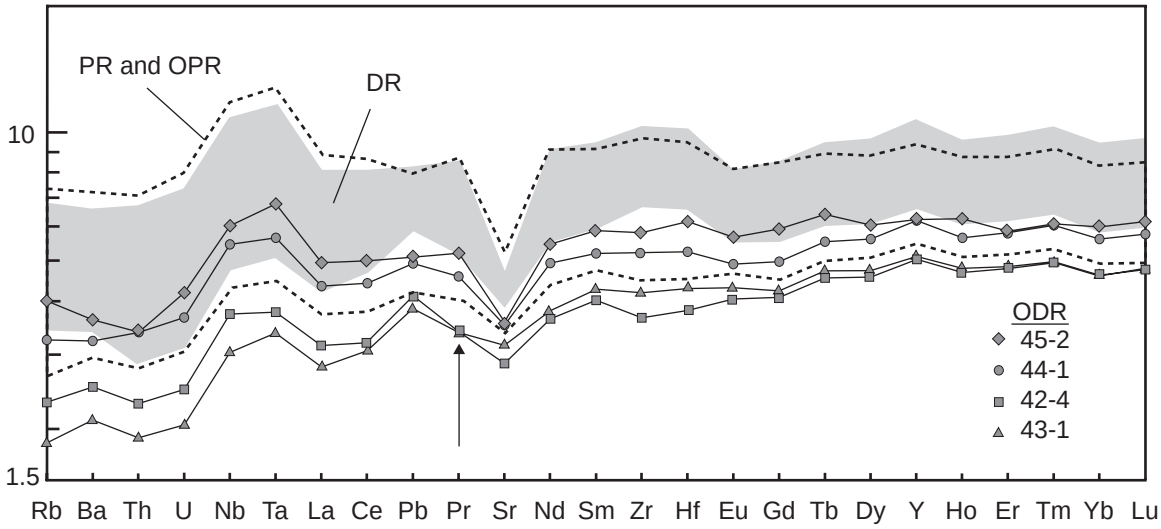

Figure 6. Primitive-mantle-normalized incompatible element patterns for lavas of the 93.25^{o}W offset on the western GSC. Dashed lines enclose a field representing all propagating limb samples (PR and OPR) and the shaded field encloses data for doomed limb samples outside the overlapping region (DR). Individual patterns shown are for the overlapping region of the doomed limb (ODR). Arrow denotes location where the patterns for samples 42-4 and 43-1 cross (see text for discussion). Primitive-mantle normalizing values are those of Sun and McDonough (1989). Zr values in samples 29-1, 32-2 and 45-2, and Y values in samples 38-2, 48-4 and 41-7 are XRF values, which we consider to be more reliable than the ICPMS values as they have lower uncertainties.

Galápagos hotspot, may indicate increasing involvement of garnet in melting closer to the hotspot.

3.4 Chemical Types

Because isotopic ratios are not affected by partial melting or crystal fractionation they act as a direct indicator of the source that melted. Western GSC samples tend to have nearly linear trends for Sr, Nd and Pb isotope ratios (Figure 7); samples from the study area encompass approximately 50-60% of the total isotopic range for the entire western GSC. Notably, data for several samples plot on the high $^{87}Sr/^{86}Sr$ side of the overall GSC array for a given εNd (Figure 7d). One of these (sample 41-7) is visibly altered and also contains high Cl (234 ppm; Ingle et al., in prep). However, sample 44-1 contains pristine glass with few phenocrysts or visual signs of alteration. If the $^{87}Sr/^{86}Sr$ of this sample has been affected by seawater it must be through pre-eruptive assimilation rather than later alteration.

The strongly linear correlation among Pb, Sr, and Nd isotopic ratios along the GSC (Figure 7) indicates that much of the variation can be explained by mixing between two main components with different isotopic ratios (e.g. Schilling et al., 1982; Schilling et al., 2003; Ingle et al., in prep). Samples 39-1 and 43-1 define the isotopic extremes within the study area. Like other GSC samples, those from the study area appear to have been derived from a mantle containing a mixture of components, one with low Sr and Pb isotopic ratios and high ε_{Nd}, and one with high Pb and Sr isotopic ratios and low ε_{Nd}.

Incompatible trace element ratios also are strongly correlated with isotopic ratios for western GSC samples (Figure 8). Because these ratios also tend to be affected little

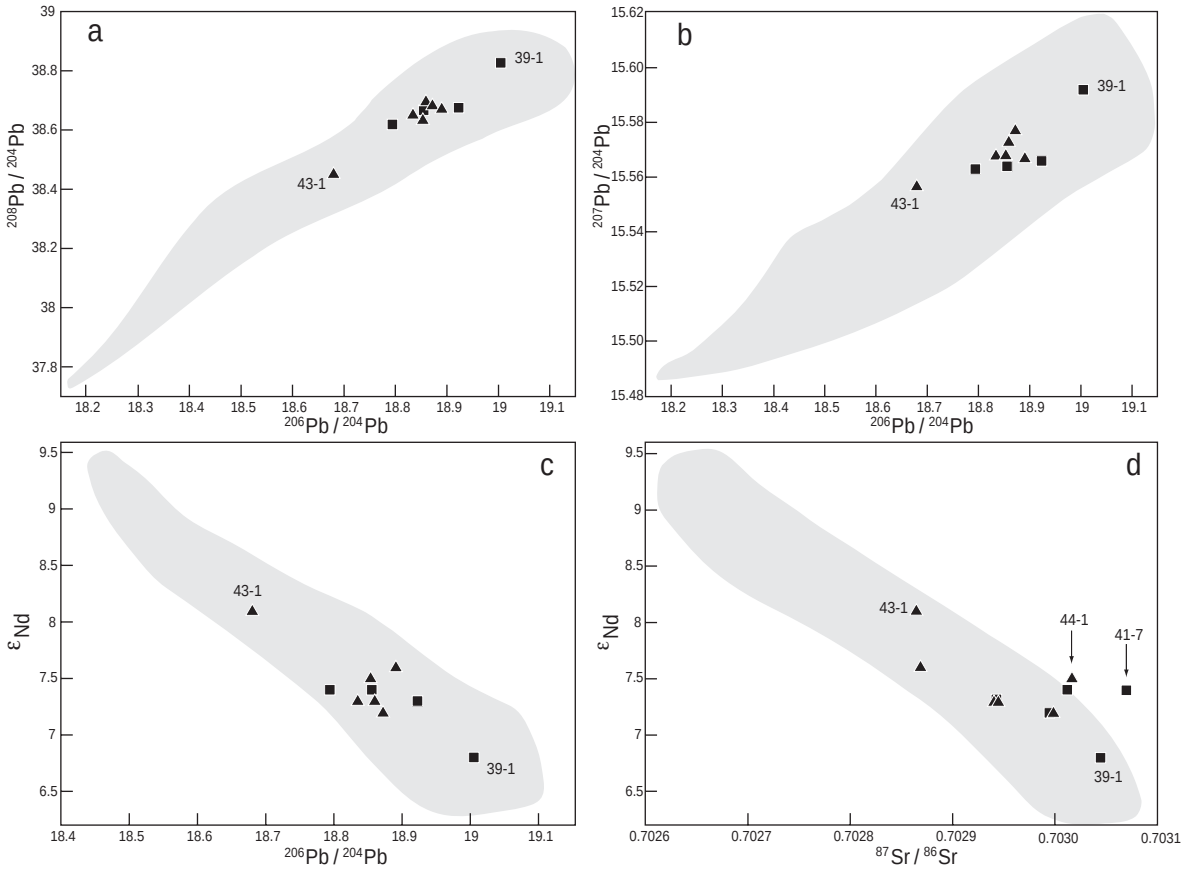

Figure 7. Sr-Nd-Pb isotopic data for the study area (symbols). Triangles denote doomed limb samples and squares denote propagating limb samples. Shaded field encloses data for the entire western GSC from Schilling et al. (2003), Christie et al. (2005), and Ingle et al. (in prep). Samples 39-1 and 43-1 define the extremes within the study area, with other data generally clustering between the two. Errors for the isotopic data are similar to or smaller than the size of the symbols.

by fractionation, they are likely representative of the range of parental magmas for this section of ridge. Furthermore, at moderate to large extents of melting, parental magma incompatible element ratios will be very similar to those of the source mantle, especially for elements with similar bulk distribution coefficients. The strong correlation of incompatible element ratios with isotopic ratios indicates that the incompatible element ratios of samples from the study area shown in Figure 8 can largely be attributed to chemical differences in the source. The two isotopically extreme study area samples also have extreme values of Nb/Zr, La/Sm and Nb/La. Plots of different trace element ratios are similarly correlated (Figure 8d, e, f) and allow us to distinguish geochemical sources for samples lacking isotopic data. Using Nb/Zr, study area samples have been separated into three general geochemical types: relatively incompatible-element enriched samples (29-1, 39-1 and 50-1) with Nb/Zr >0.08, relatively incompatible-element depleted samples (43-1, 48-1 and 51-1) with Nb/Zr < 0.06, and all other samples comprising an intermediate group with Nb/Zr between 0.06 and 0.08. The isotopically extreme samples (39-1 and 43-1) clearly fall within the two end-member types. According to the classification scheme of Cushman et al. (2004), based primarily on K/Ti, all these samples are T-MORB, except for sample 43-1, which is N-MORB. We therefore adopt the terminology of eT-MORB, nT-MORB and dT-MORB to distinguish our three groups. Obviously, this is an arbitrary division among a continuum and, even though sample 43-1 can be classified as N-MORB, we will retain the terminology of dT-MORB in this paper.

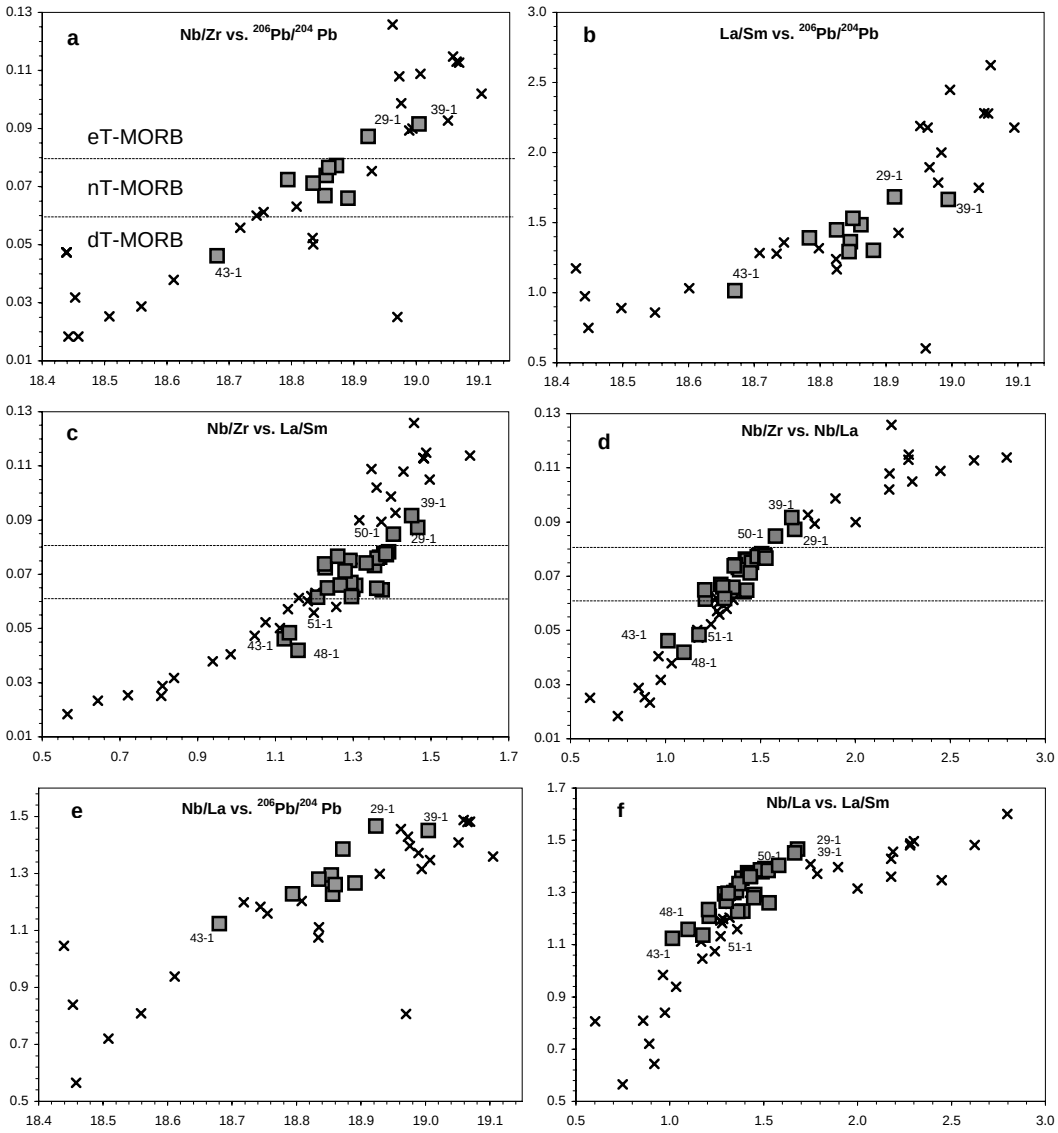

Figure 8. Correlations among isotopic ratios and ratios of incompatible trace elements allow us to subdivide the GSC T-MORB into three geochemical types. Because these ratios are little affected by melting and differentiation, these variations likely reflect differences in mantle source composition. Squares denote study area lavas; x's denote lavas to the east and west of the study area along the western GSC collected as part of the G-PRIME cruise (Ingle et al., in prep). Study area sample trends are similar to those for the rest of the western GSC. Using Nb/Zr as a discriminant, we define the three types as relatively depleted dT-MORB with Nb/Zr <0.06, normal nT-MORB with Nb/Zr between 0.06 and 0.08, and relatively enriched eT-MORB with Nb/Zr > 0.08. Study area dT-MORB and eT-MORB are labeled. The same results are attained if $^{87}Sr/^{86}Sr$, εNd, $^{208}Pb/^{204}Pb$, or $^{207}Pb/^{204}Pb$ is plotted instead of $^{206}Pb/^{204}Pb$.

3.5 Geochemical Variations

Overall variations of most major and trace elements in this study are generally consistent with evolution by crystallization of olivine ± plagioclase ± clinopyroxene (Figure 9). As expected, the eT- and dT-MORB chemical types defined in the previous section show trends at higher and lower values, respectively, for the incompatible elements Nb, La, K/Ti and P_2O_5 (not shown) at a given value of MgO. These differences are apparent in both glass and whole-rock data for Nb and K/Ti, despite analysis by different methods and the incorporation of variable amounts of phenocrysts in the whole rocks. Although whole-rock XRF analyses for Na_2O are consistently ~0.15 wt % lower than values obtained by electron probe on glass, Na_2O values for the three groups (eT-, nT-, and dT-MORB) are indistinguishable at the same MgO content. In addition, sample data for the eT group tend to cluster near the high side of Sr at a given MgO, while the dT group samples may have lower Ni content at a given MgO compared to other samples from the area.

Much of the scatter in several MgO variation diagrams (e.g. CaO, Na_2O, Sr, and Ni) is greatest at high MgO values, and many of these samples come from the overlap zone between the OPR and ODR. For example, all samples with >140 ppm Ni are nT-MORB within the overlap zone. Of these, sample 44-1 also has low SiO_2 and moderately high Al_2O_3, features that Eason and Sinton (2006) attribute to high-pressure crystallization of clinopyroxene close to offsets along the GSC. Sample 45-2 has low Al_2O_3 and CaO, as well as high Na_2O, TiO_2, K_2O and P_2O_5 compared to other samples from the study area.

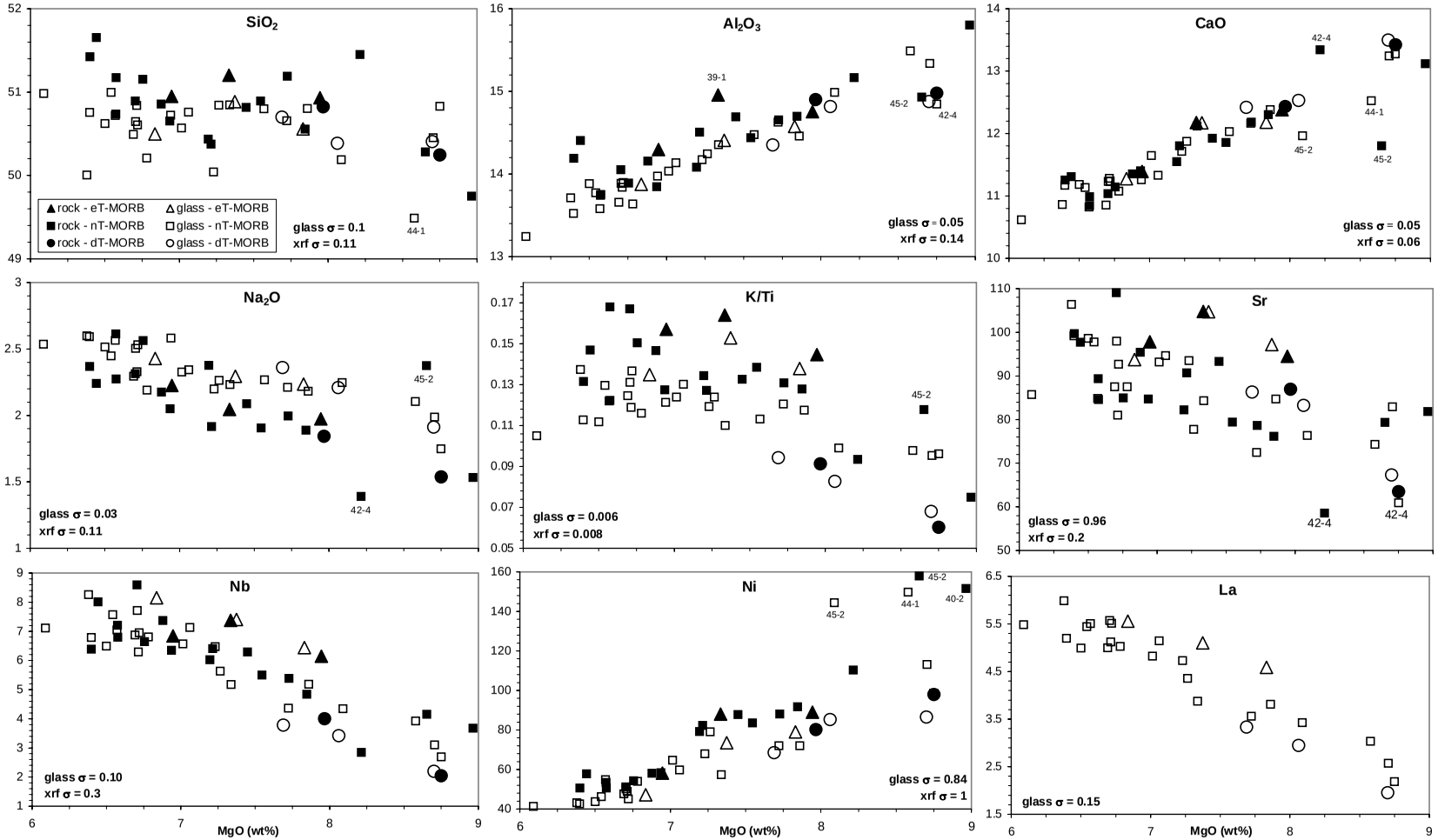

Figure 9. Variation of selected major element oxides (wt %) and trace elements (ppm) versus wt %MgO. Glass data obtained by electron probe and ICPMS, as well as whole rock XRF data are plotted; see legend. Most trends are at least broadly consistent with low-pressure evolution by fractional crystallization. Standard deviation for glass MgO is 0.07 wt% and whole rock MgO is 0.03 wt%. For explanation of how standard deviaitons were determined; see text for whole rock, Cushman et al. (2004) for glass major element oxides, and Table 4 for glass trace elements.

3.5.1. Along-Axis Geochemical Variations

The geochemical signature of MORB is highly dependant on the degree of partial melting incurred in the mantle. In order to compare the degree of melting of samples with varying degrees of differentiation along axis, each samples composition was adjusted to a common MgO content of 8 wt%, according to the procedure of Klein and Langmuir (1987). Trace element variations versus MgO are curved, as approximated by Henry's Law, and were adjusted using a power-law regression ($y=Ax^B$). Major element oxide variations versus MgO are straight and were adjusted using a linear regression (Cushman et al., 2004). Following the methods of Cushman et al. (2004), samples with MgO content >8.5 wt% or <3.5wt% were not used in the regressions. The adjusted values are indicated hereafter with the subscript 8.

Many geochemical parameters along the GSC show long-wavelength trends with distance from the Galápagos hotspot (e.g. Schilling et al., 1982; Langmuir et al., 1992; Detrick et al., 2002; Cushman et al., 2004), and many of these gradients are apparent around the 93.25˚W OSC (Figure 10). For example, $^{206}Pb/^{204}Pb$, Nb/Zr Nb/La, $La_{(8)}/Sm_{(8)}$ and $La_{(8)}/Yb_{(8)}$ all increase from west to east through the study area, especially if only the nT-MORB samples are considered, the most abundant geochemical type. For many chemical parameters there are crudely parallel compositional trends with distance along axis among each of the chemical types, although eT- and dT-MORB are less well represented in our collection. The long-wavelength trends are not continuous through the overlap zone, which is characterized by much greater geochemical variability than the ridge segments to the west and east. Much of this variability is related to the presence of extreme compositional types. E.g., the samples with both the highest and lowest Nb/Zr,

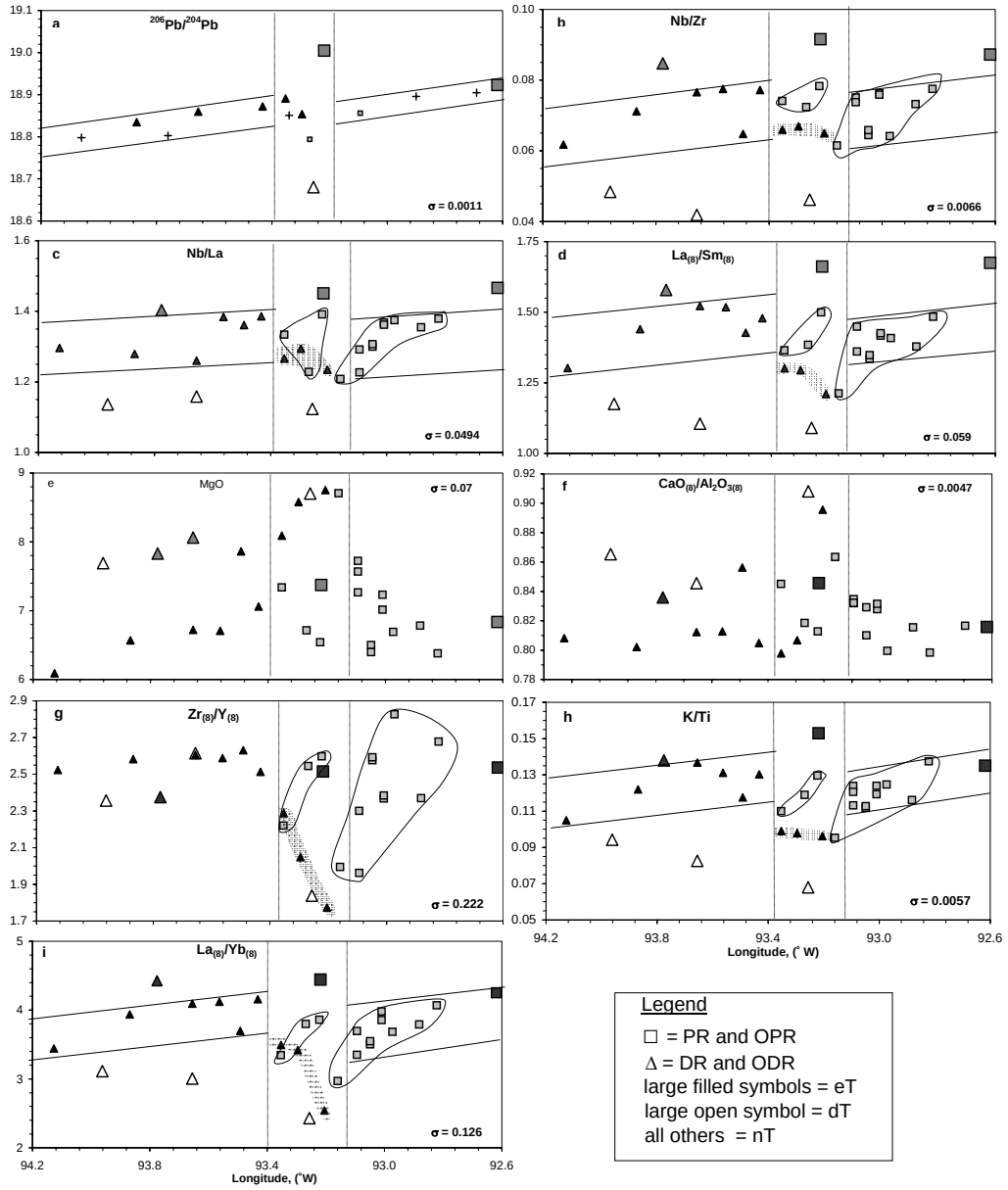

Figure 10. Along axis variations of selected parameters in glass. Major element glass data for each sample are presented in Appendix A and reported as group averages for each dredge in Cushman et al. (2004). Crosses in $^{206}Pb/^{204}Pb$ are data from Schilling et al. (2003). Vertical lines bound the overlap region. Notice the long-wavelength chemical gradient seen in nT samples (bounded by sub-horizontal lines) interrutped by large variations in the overlapping region. Two trends of decreasing incompatible trace element ratios from east to west are seen in the propagating limb and outined with light shading. A sharp decrease in doomed rift incompatible element ratios as the overlap zone is entered is shown with dark shading. Similar trends are seen in eT and dT samples. Group average K/Ti data (Cushman et al., 2004) are used for K/Ti of sample 29-1.

Nb/La, $La_{(8)}/Sm_{(8)}$ and $^{206}Pb/^{204}Pb$ were recovered from within the overlap zone. It is notable, however, that the various chemical types are not geographically restricted, but instead have representatives that occur sporadically along the length of the study area and in all four regions (DR, PR, OPR, ODR).

There also are pronounced variations in MgO, with generally increasing values as the overlap zone is approached from both the east and west. Again, similar increases are observed for the different geochemical types. Both eT and dT samples tend to have higher MgO for their position on the ridge axis, relative to the more common nT group for DR and ODR samples. The overall pattern for the doomed rift is for lower values of Nb/La, $La_{(8)}/Sm_{(8)}$ and $Zr_{(8)}/Y_{(8)}$ within the overlap zone compared to outside the overlap zone; i.e., as the doomed rift progressively fails. Relations along the propagating rift are more complicated, the details of which are contained in a later section.

4. Discussion

4.1 Evidence for Dueling Propagation

Studies of the fine-scale structure of ridge-axis discontinuities indicate that short ridge segments can be abandoned by a process described as self-decapitation and dueling propagation (Macdonald et al., 1987). This concept was developed further with computer simulations by Wilson (1990), who argued that rift failure associated with propagating OSCs is likely to be highly episodic. In these models, ridge behavior is shown to be cyclic, with the tip of the failing rift becoming deflected away from the ridge axis through time until a certain degree of outward curvature is obtained, at which time it is abandoned, and a new doomed rift forms (Figure 11). For small offsets, as in the

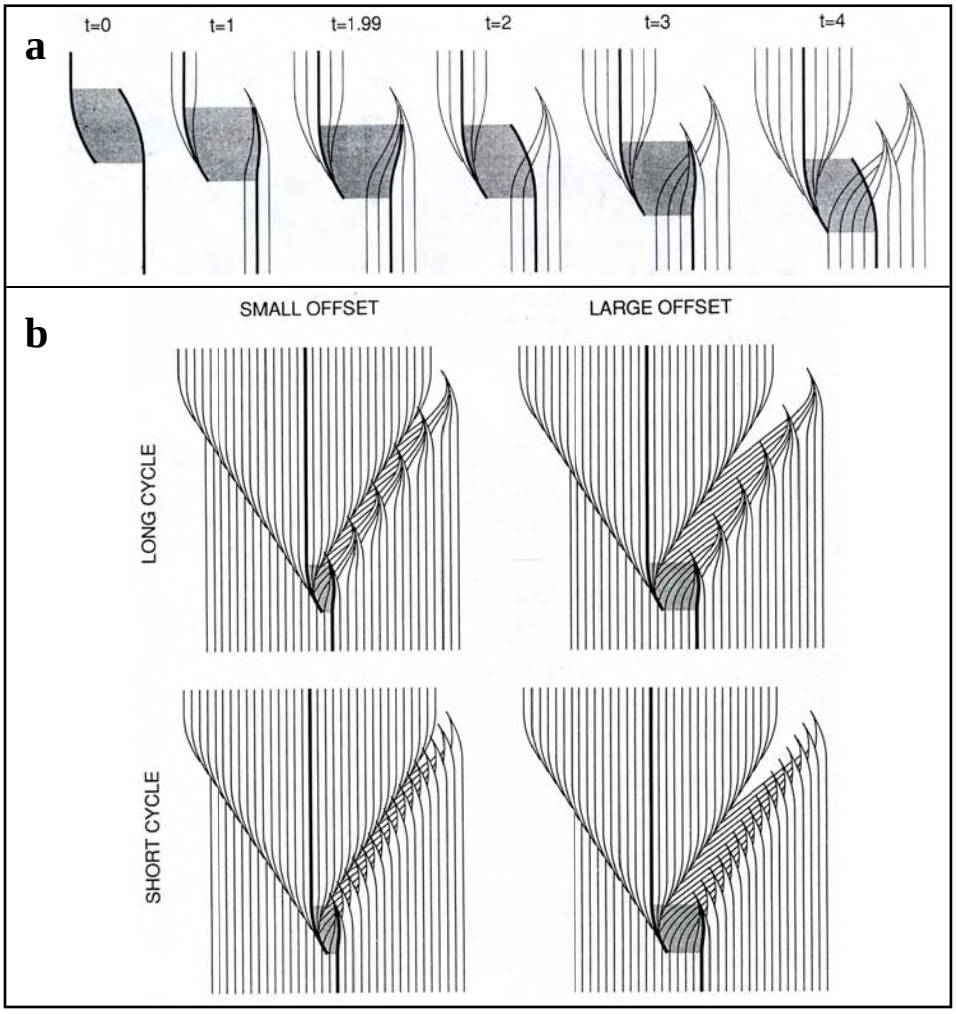

Figure 11. (a) Kinematics of overlapping rift propagation by cyclic failure of the doomed rift shown through a series of snapshots through time (from Wilson, 1990). The doomed limb fails episodically through the process of self decapitation, first described by Macdonald et al. (1987). The thick line is the ridge axis, the grey area represents the zone of transferred lithosphere, the thin lines represent increments of seafloor spreading, or isochrons. At t=0 the overlapping limbs are curved towards each other in a stable configuration. At t=1 some increment of seafloor spreading and propagation has occurred causing the doomed rift tip to become deflected away from the ridge axis. At t=1.99 the doomed rift has obtained a very unstable configuration. At t=2 the doomed ridge is abandoned and a new failing rift propagates across the inner pseudofault to achieve a more stable configuration. This model assumes non-dueling propagation but can be modified to incorporate dueling OSCs in which the propagating rift also can become abandoned during times of failing rift jumping and propagation. (b) Small offsets and short cycles are less obvious in seafloor bathymetry.

93.25˚W OSC, inward jumps can cut across the inner pseudofault into material formed at the propagating segment. The physical manifestations of these episodic ridge jumps on the seafloor are lost if the jumps occur frequently relative to the spreading rate. The above described model assumes non-dueling OSC limbs, with uninterrupted propagation, but can be modified to incorporate dueling OSCs in which the propagating rift can also be abandoned during times of failing rift jumping and propagation.

Visual inspection of high-resolution multi-beam bathymetry (Sinton et al., 2003) shows the possibility of abandoned rifts on the propagating and doomed limbs (Figure 12). Dredges 37, 38, and 39 appear to have sampled an abandoned rift with dredge 40 sampling the current rift tip. Coincidentally, the interruption in the repeating pattern seen in the along axis geochemistry, between dredge 40 and 39 (Figure 10), is located between the possible current propagating ridge tip and an abandoned ridge (Figure 12). Possibly dredged 39, 38 and 37 are sampling a decapitated version the current rift, owing to the similar chemical pattern. It is interesting to note that the propagating rift appears to be retreating, which is opposite the long term propagation trend of ~70 mm/yr to the west described by Wilson and Hey (1995). They looked at this region in terms of magnetic anomalies, of which the last one was 780,000 years ago. It is possible that this dueling process may be happening on a scale of a few 1000's of years and therefore wouldn't show up in the magnetic anomaly patterns. Also, the lack of a magnetic anomaly in recent times makes mapping the pseudofault to within close proximity of the propagating rift tip not possible. On the doomed ridge, a possible abandoned rift occurs north of the current dying rift (ODR) and appears to trace back to the current ridge axis between the DR and ODR; this is also where a change in geochemical gradient occurs.

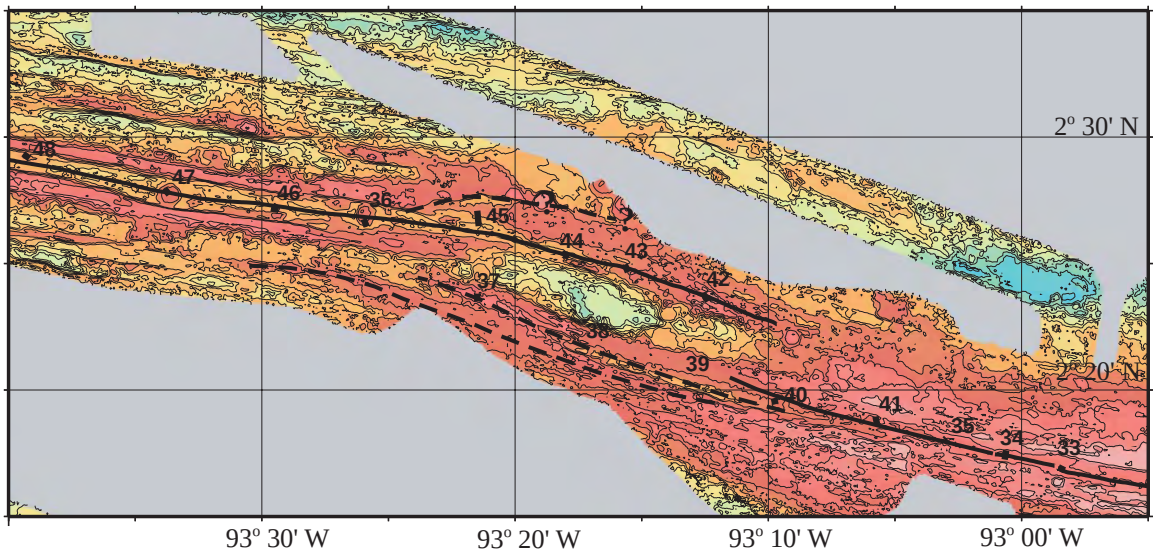

Figure 12. Multibeam bathymetric map of the 93.25ºW OSC, showing possible abandoned propagating and doomed rift segments. Solid lines are the current rise axis, dotted lines are the possible abandoned rifts. G-PRIME dredge locations are labeled (Sinton et al., 2002).

4.2 Implications for Magma Chamber and Eruptive Processes

4.2.1 Propagating and Doomed Rift

An important finding of this study is the large extent of variability in many chemical parameters over short along-axis distances. MgO varies by more than 1.5 wt % between successive sample sites less than 10-15 km apart. There are similarly wide variations at short spatial scales in ratios such as Nb/La and La/Sm. Although there are general along-axis gradients in many chemical parameters within individual chemical types (Figure 10), the distribution of these types is highly irregular along axis. Almost every sample station in this study has returned lavas with compositions that are markedly different in their estimated extent of low-pressure differentiation, parental magma composition, or both, compared to neighboring sites. Although a relatively shallow magma chamber reflector has been imaged by seismic reflection in much of this area (e.g. Blacic et al., 2004), it is clear that processes operating in these magma chambers do not efficiently homogenize magma compositions over length scales as long as our sample spacing. Sinton et al. (1991) argued that the along-axis length of contiguous mid-ocean ridge characterized by similar parental magma compositions, which they called second-order magmatic segmentation, should increase exponentially with spreading rate. The magmatic segment length predicted by those authors (see Figure 15 of Sinton et al., 1991) for the 52 mm/yr spreading rate of the GSC in this area is 11 km. Our observations of differing compositions between neighboring dredge sites indicate that the length scale of magma homogenization in this area can be no greater than this value.

The result of differing lava compositions in nearly all successive dredge locations also has implications for the size of lava flows in this area. In only one case did the same

composition occur in two successive dredges. One sample in dredge 48, from a small high in the axial graben, has an identical glass composition to those in dredge 47, which sampled an axial seamount ~10 km away. Other samples from dredge 48 were of differing composition and are considered to have originated from a flow local to that area. We interpret this result to indicate that a lava flow, probably emanating from the axial seamount of dredge 47, extends at least 10 km to the vicinity of dredge 48. Two or three different chemical types occur within several other dredge sites (Cushman et al., 2004; Appendix A). These dredge sites tend to be on the propagating ridge and are dominantly near the end of the segment, before the rafted limb trace joins the ridge. We conclude that most eruptions in this area have tapped magma chambers that are chemically discontinuous, and that the length of axis covered by individual eruptive units is mostly less than our dredge spacing.

Although magmatic processes in this area do not homogenize magma compositions, there is evidence that magmatic evolution has mainly occurred at similar depths in the crust for samples outside the overlap zone. Shallow-level fractionation of a parental melt appropriate for nT-MORB was modeled using the MELTS algorithm (Ghorsio and Sack, 1995) at varying pressures to draw inferences as to the depth of magma evolution in the study area. Samples from outside the overlap zone are consistent with evolution at ~1000 bars. Generally lower SiO_2 in PR lavas relative to DR lavas may indicate evolution at slightly higher pressures (Figure 13), but the lack of evidence for different evolutionary paths for other elements, e.g., Al_2O_3, Na_2O and FeO*, suggests that the parental magmas for the DR and PR may have had slightly different SiO_2 contents. See Chapter 2 for an explanation of how parental melts were calculated.

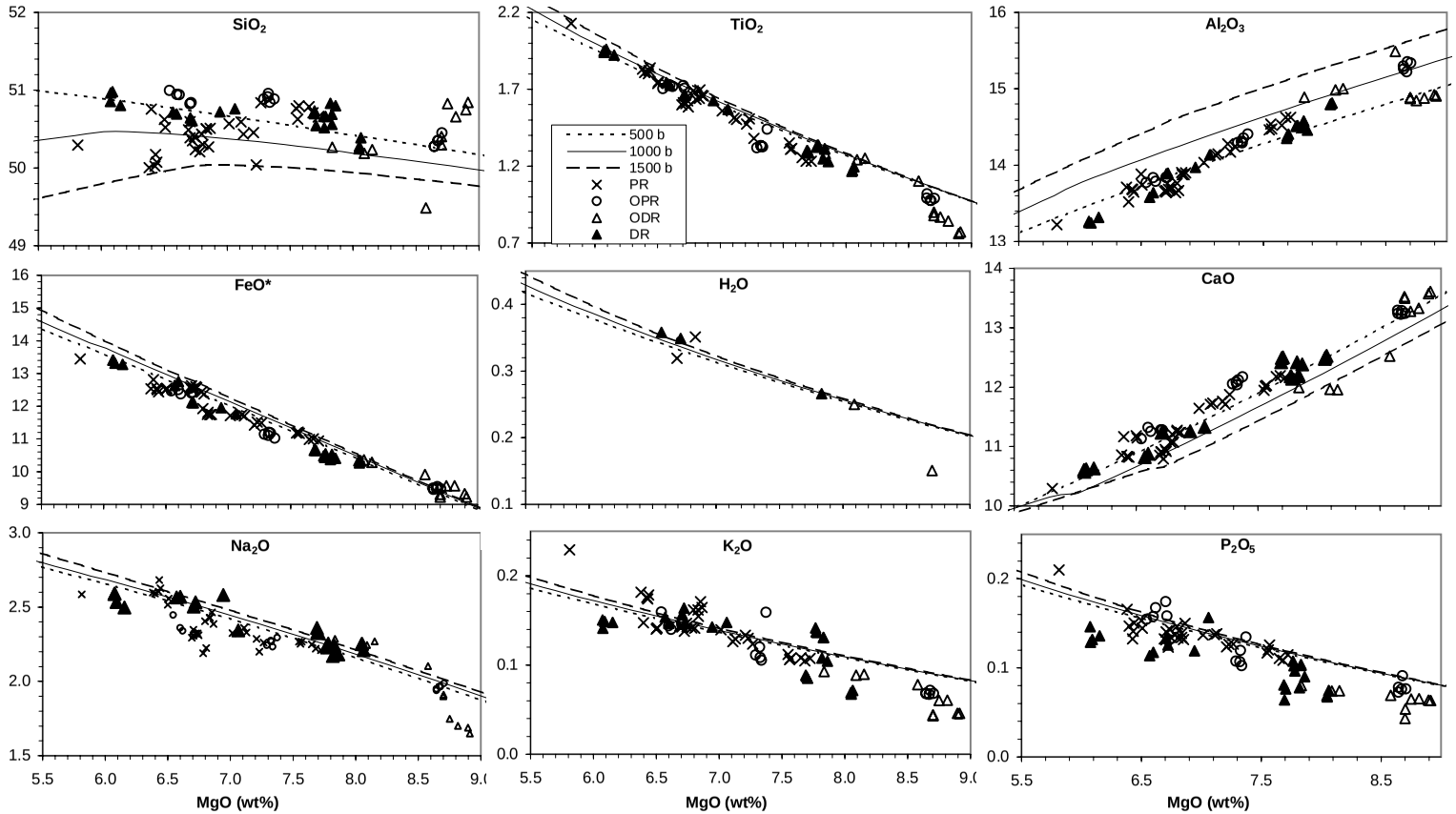

Figure 13. Model shallow-level fractionation paths of the nT parent using the MELTS algorithm at 500, 1000 and 1500 bars (Ghorsio and Sack, 1995) are compared to the study area data. Magmatic evolution occured at similar depths in the crust for samples outside the overlap zone (~1000 bars). Note that SiO_2 is lower in most PR samples compared to DR samples, which could reflect either a higher pressure evolution or a lower-SiO_2 parent for the PR. However, these samples lack the differences predicted for higher pressure evolution on in Al_2O_3, Na_2O, FeO* and CaO. We therefore interpret this difference as reflecting parental magma composition rather than differences in conditions of evolution. All models used an oxygen fugasity of FMQ -2. See Chapter 2 for explanation of how the composition of the nT parent was calculated.

4.2.2 Propagating and Doomed Rifts of the Overlap Zone

Inside the overlap zone, the local chemical and isotopic variability is much greater at even shorter length scales (Figure 10). The regional geochemical gradients along the western GSC are disturbed within the zone, with more extreme compositions there. Although uncertainties of some elements in some samples from the OSC are close to those along the MELTS-derived liquid lines of descent, the wide geochemical variability within the overlap zone precludes the possibility of relating all samples to a set of common parental magmas or evolutionary conditions.

The mineralogical data are particularly important for understanding magmatic processes within the overlap zone. Propagating overlapping-limb lavas tend to be more crystal rich, containing 10-16% crystals vs. 2-11% outside the overlap zone, and commonly contain multiple compositional populations of plagioclase and olivine with significant core to rim variations (Tables 1 and 2), many of which are far from equilibrium with their host glasses (Figures 4 and 5). The chemical and mineralogical diversity within the OSC indicates, along with the presence of sieve-textured plagioclase in some samples, that magma mixing and the entrainment of xenocrysts is more important in this zone than in the ridge segments outside the zone. These are all characteristics of low-magma-supply ridges lacking a well-developed melt lens (e.g., Sinton and Detrick, 1992), and where magma chambers tend to be smaller, more intermittent, and probably also deeper in the crust.

Rubin and Sinton (2007) showed that the extent of magma homogenization, particularly for chemical features inherited from the mantle, is also a feature of low-magma-supply mid-ocean ridges, which tend to be significantly less differentiated than

higher-supply ridges. The high chemical diversity and high MgO contents of magmas within the overlap zone are therefore also consistent with the interpretation that this zone is one of low overall magma supply.

From evidence outlined in the above discussion, we conclude that the high magma supply, broad magma chamber model is not appropriate for the overlapping spreading center at 93.25˚W on the GSC. The petrological data from this OSC are better explained by small, discontinuous magma chambers, characterized by overall low magma supply.

4.3 Geochemical Patterns Related to Rift Propagation at 93.25°W

Along the propagating rift there are gradual decreases in ratios of highly incompatible to moderately incompatible trace elements, along with a gradual increase in CaO/Al_2O_3 for at least 50 km as the overlap zone is approached from the east. This pattern is repeated for the short, propagating limb segment within the overlap zone which may be a new propagating ridge segment formed by dueling propagation. In contrast, there are no gradients in any of these parameters along the doomed rift outside the overlap zone, other than those that can be related to long-wavelength gradients associated with proximity to the Galápagos hotspot. The presence of gradients on the propagating rift and not on the doomed rift is generally consistent with propagating rift theory because magmatic processes, including overall magma supply and the development of magma chambers, can continue to evolve for long distances behind the initial rifting through old lithosphere (Christie and Sinton, 1981; Sinton et al., 1983; 1991; Hey et al., 1989, 1992). In contrast, the doomed rift is generally unaffected until it actually begins to fail by

passage of the propagating tip. In this regard, the doomed rift can be considered to be a normal rift that does not "know" that it is doomed to fail if rift propagation continues.

Although chemical gradients along the propagating rift, and the lack of similar gradients along the doomed rift, are generally consistent with rift propagation, the nature of the gradients in this area is different from those normally ascribed to propagating rifts elsewhere. Whereas most propagating rifts have pronounced gradients in parameters that can be related to the extent of low-pressure differentiation (e.g., pronounced fractionation anomaly on the OPR), the geochemical signature of rift propagation at the 93.25°W GSC propagating rift is mainly in ratios that are not strongly affected by crustal processes and instead indicate differences in the composition of parental magmas derived from the melting processes.

The compositional variations along the propagating rift inside the overlap zone (OPR samples, dredges 39, 38, 37) are consistent with this segment being a former propagating rift tip that has been decapitated by dueling propagation because the gradients are identical to those of the PR just outside the overlap zone. Although there are no pronounced gradients other than MgO along the DR, samples within the overlap zone (ODR, dredges 45 to 42) show strong gradients of decreasing ratios of highly to moderately incompatible elements with progressive rift failure; i.e., from west to east within the zone (Figure 10). The three eT- and dT-MORB samples appear to follow trends parallel to those of nT-MORB for both the ODR and OPR. Thus, the overlap zone tends to have increased chemical variability, owing to the presence of all three major chemical types, and progressive incompatible element depletion within individual chemical types along axis toward both the propagating and failing rift tips.

In general, the development of incompatible-element depleted lava compositions can arise from large extents of non-batch partial melting, melting of an incompatible-element depleted source, and / or variations in melt migration within the upwelling mantle. The relative roles of these processes in contributing to the chemical variations at the GSC 93.25˚W offset are evaluated in the following sections.

4.3.1 High Degrees of Partial Melting in the Overlap Zone

With progressive increase in extent of melting of a common source (increasing F), incompatible trace elements will become increasingly depleted in order of their bulk distribution coefficients. Therefore, the progressive incompatible element depletion within the overlap zone could reflect progressively larger extents of melting in this zone. Ratios of elements with closely similar bulk distribution coefficients (Nb/Zr, Nb/La) should be affected less than those with more widely differing distribution coefficients ($Zr_{(8)}/Y_{(8)}$, $La_{(8)}/Yb_{(8)}$) but with a similar overall pattern, as is seen in the data (Figure 10). Samples of the eT- and dT-MORB groups have overall higher and lower ratios, respectively, but appear to follow similar trends to the nT-MORB. The interpretation that low incompatible element ratios, where the more incompatible element is in the ratios numerator, are derived from larger extents of melting is generally consistent with the observed increase in $CaO_{(8)}/Al_2O_{3(8)}$ along the propagating and failing rifts (Figure 10), and the overall negative correlation between $CaO_{(8)}/Al_2O_{3(8)}$ and $L_{a(8)}/Yb_{(8)}$ (Figure 14), which should be inversely correlated with progressive melting. Larger melting extents in the overlap zone also are consistent with the shallow bathymetric expression of the overlapping limbs at the 93.25˚W OSC. Unlike most

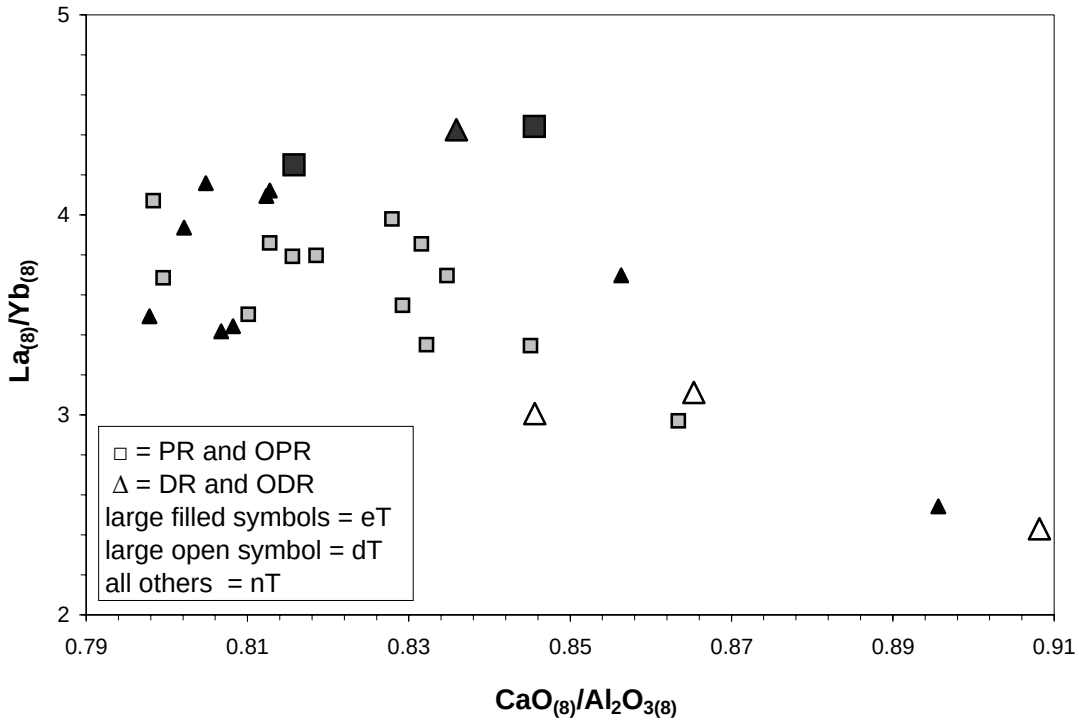

Figure 14. Fractionation-adjusted La/Yb vs. CaO/Al_2O_3. The negative correlation for each of the three mantle types adds further confirmation of the melting trends in highly to moderately incompatible trace element ratios. High-degree melts tend to produce high CaO/Al_2O_3 lavas because Al is more incompatible than Ca in clinopyroxene. High-degree melts also tend to produce lower La/Yb lavas because Yb is more incompatible than La. As the degree of melting decreases, the relative amounts of Ca and La going into the melt increase. Symbols are the same as those in Figure 10.

overlapping spreading centers, which contain pronounced deep bathymetry at the overlapping limbs, this OSC displays limbs which are shallower than the adjacent ridge axes by up to 150 m (Sinton et al., 2003). The presence of a negative mantle bougier anomaly (MBA) over the overlapping limbs (M. Behn, pers. comm., 2007) argues against these shallow limbs being dynamically supported. The presence of a fossil high to remain without requiring buoyant support from low-density material in the crust or mantle has been addressed by Shah and Buck (2006). Through elastoplastic thin plate flexure models, they attribute shallow remnant ridges to plate strengthening during cooling and melt solidification, resulting in the preservation of a "frozen" fossil high.

Taken together, bathymetric and some geochemical evidence supports an interpretation for larger degrees of melting within the overlapping segments of this part of the GSC despite our previous arguments that magma chambers are poorly developed and that the data are strongly indicative of a low melt flux. It is hard to reconcile arguments for poorly developed magma chambers and low magma supply with high degrees of melting of the underlying mantle and it is also counter-intuitive to expect robust melting as a rift progressively dies or a new rift forms in old lithosphere. Although the overlapping limbs are shallow, they also are relatively narrow, and there is no evidence for thicker crust in the overlap region. The presence of isotopic extremes in the overlap zones argues against high melt volumes in this region as high melt flux should tend to homogenize magma compositions, either in the melt accumulation zone within the mantle or within crustal magma chambers (e.g. Rubin and Sinton, 2007). The simplest explanation for the greater isotopic heterogeneity within the OSC is that smaller volumes of heterogeneous mantle are melted there. The creation of relatively low-

volume melts, low melt flux, and melt evolution in small, poorly developed magma chambers better explains how these unique compositions can be preserved and expressed at the surface. Finally, we note that Na_2O does not vary in a way that would be expected if simple melting variations controlled the low incompatible element ratios and high CaO/Al_2O_3 observed.

The strong evidence for small melt volumes and poorly developed magma chambers, along with the geological implausibility of high degrees of melting associated with rift failure and new rift initiation, leads us to explore alternative explanations for the geochemical variations in this region.

4.3.2 Melting of Previously Depleted Mantle

The evidence for increasing incompatible-element depletion with progressive rift failure and as the propagating rift tip is approached need not be associated with unusually large extents of melting if we allow for variable mantle composition in the region. For example, incompatible-element-depleted magmas could be produced by melting previously depleted mantle in these zones. Prior melting will leave a residual mantle depleted in the more incompatible elements, but leaves isotopic ratios unchanged, assuming materials with different isotope compositions all melt in the same way. The residual mantle also will have higher CaO/Al_2O_3 because of selective enrichment of Al in the melt phase during prior melting, and will generally be more refractory than less depleted mantle. Thus melting of previously depleted mantle should produce the characteristic chemical features of the area at low melt volumes and total melt fluxes, which in turn should result in poorly developed crustal magma systems. The challenge is

to understand why previously depleted mantle might be preferentially melted beneath the OSC.

Decompression melting at mid-ocean ridges is an incomplete process, such that parcels of upwelling mantle tend not to melt more than about 20% (e.g., Klein and Langmuir, 1987; Plank and Langmuir, 1992; Langmuir et al., 1992). Because of the nature of mantle flow beneath spreading ridges, the unmelted, residual mantle passes through the melting zone and is rafted away with the plate, assuming passive mantle flow. The amount of melting experienced by this mantle varies with depth and the composition of residual mantle depends on the level to which it rises within the melt zone. Deeper material undergoes the least amount of melting and therefore is the least depleted in highly to moderately incompatible elements. Material that rises to shallower levels will have undergone the most melting and therefore is most depleted in incompatible elements. The section of mantle that has passed through the melting zone is referred to as the residual melt column (RMC) (Klein and Langmuir, 1987; Plank and Langmuir, 1992; Langmuir et al., 1992) (Figure 15), which is characterized by vertical variation in amount of melt (and incompatible element) depletion.

Because of the geometric relationship between the opposing limbs of the OSC, it is possible that each of these limbs could be tapping mantle that had previously cycled through the melting zone of the other limb. For example, because the offset between the two limbs at the 93.25˚W OSC is small (24 km of overlap and 7 km of offset), the ODR should be tapping the RMC recently created at the OPR.

Similarly, the OPR is breaking through and melting mantle that could be residual from previous melting along the doomed limb. Whether or not one rift taps mantle that

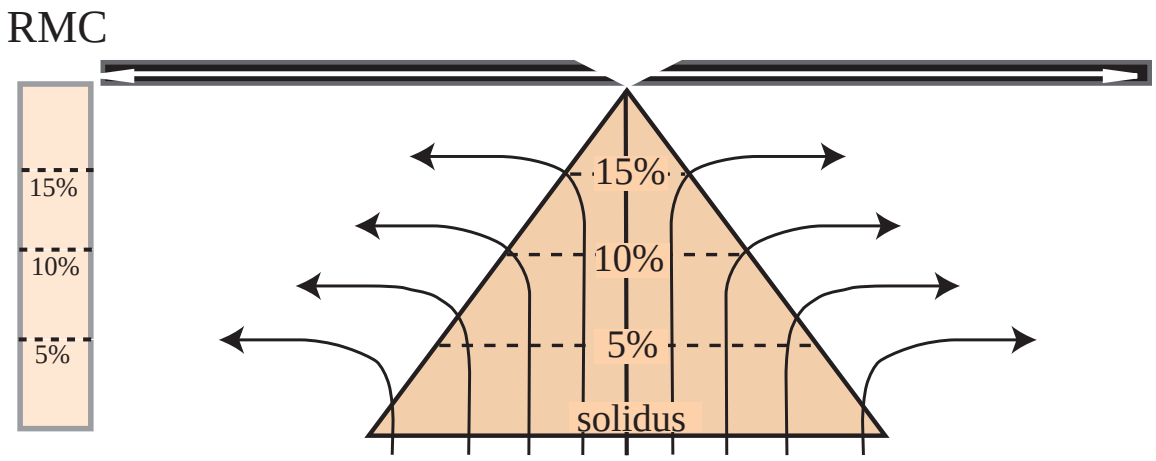

Figure 15. Schematic diagram showing the melting dynamics at mid-ocean ridges. Melting occurs within the melting zone triangle; arrows depict mantle flow; dotted lines depict extent-of-melting contours. Residual mantle exits the melting region after having undergone varying extents of depletion depending on its depth within the melting zone. The column of residual mantle is referred to as the residual melt column (RMC) by Plank and Langmuir (1992).

was previously depleted by prior melting depends on a number of variables, including the depth where melting begins, which is primarily a function of mantle potential temperature, and also on the relative geometries of the respective limbs compared to the directions of mantle flow in the region. Although mantle flow in the plate reference frame will usually be symmetrical about the ridge, as indicated in Figure 15, it is important to consider how the ridge axes migrate relative to the deeper mantle. Using the angular velocities of Gripp and Gordon (2002), the 93.25˚W OSC is moving 41.5˚NE at a rate of 32 mm/yr in the hotspot reference frame. This ridge motion predicts that the OPR is moving over mantle that was just melted at the doomed overlap zone.

Alternatively, the OPR could be a limb newly created through the most recent episode of dueling between the propagating and doomed limb, and therefore be melting mantle inside the pseudofault (Figures 11, 12) which was previously melted by the abandoned propagating limb. In either case, incompatible element depletion accompanying low melt supply can be explained by melting of previously depleted mantle, and the geometry of the 93.25˚W OSC is consistent with the OSC limbs tapping mantle that was residual from previous melting in the local environment.

4.3.3 Incomplete Melt Focusing

Yet another option to explain incompatible element depletion is through incomplete focusing of melt to the ridge axis (e.g., McKenzie, 1984; Plank and Langmuir 1992) (Figure 16), in which low-degree melts from the corners of the triangular melting region will be the least likely to migrate to the ridge axis. This may be in response to less suction drawing melt to the ridge axis over the broader zone of extension over the overlap

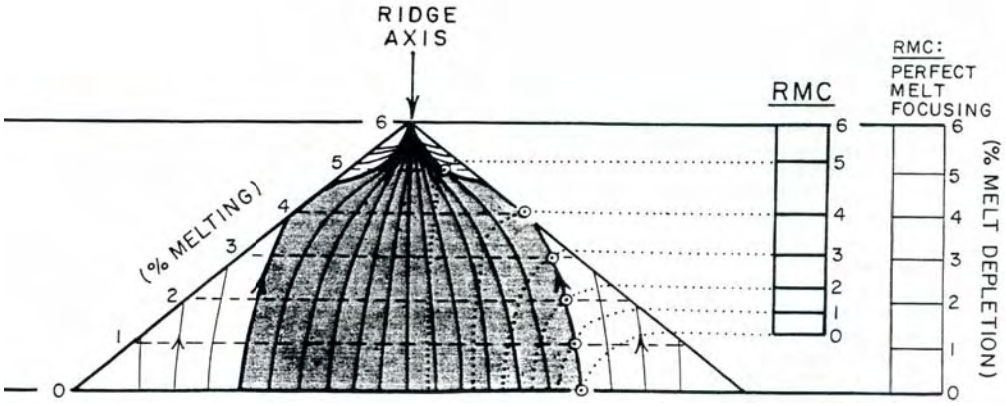

Figure 16. Schematic diagram showing how incomplete melt focusing could affect the chemistry of the lavas and RMC (from Plank and Langmuir, 1992, after Spiegelman and McKenzie, 1987). Grey shading denotes the region where melt is focused to the ridge axis (shown by heavy arrows). Melt in the non shaded region does not get focused to the ridge axis (shown by light arrows).

region. The effect of this process is that the mean extent of melting for melts that do make it to the ridge axis will be greater, and the total melt flux lower, than for the case where melt extraction and migration to the ridge axis are complete. The process of incomplete melt focusing can explain our observations if melt focusing is progressively less complete as the doomed rift dies and as the propagating rift tip is approached from the east. Unfortunately, melt migration is poorly understood and the controls on the efficacy of melt focusing even less so (e.g. Phipps Morgan, 1987; Scott and Stevenson, 1989; Spiegelman, 1996; Katz et al., 2006). For example, it is not presently known how a diffuse or overlapping plate boundary configuration, such as that at OSCs, might affect melt migration patterns in the underlying asthenosphere.

Of the three possible explanations for incompatible element depletion in the OSC region, we consider the argument for greater extents of melting to be the least plausible, geologically. Furthermore, other evidence, particularly the wide diversity of mantle source characteristics in this zone and the presence of high MgO lavas with complex mineralogical relations, most likely reflects low melt supply to the dying and propagating limbs within the overlap zone. High geochemical diversity is also a characteristic of the GSC 95.5°W (Ingle et al., in prep.) and EPR 20.7°S (Mahoney et al., 1994; Smaglik et al., in prep) propagating rift regions. The most likely explanation for this diversity is that melting taps smaller volumes of heterogeneous mantle in these zones, a scenario that is consistent with overall low magma supply to these offsets.

Although we do not understand why the limbs at 93.25˚W are unusually shallow, abandoned ridges in other complex OSCs can be relatively shallow, e.g. EPR 20˚S

(Macdonald et al., 1988), and the stresses at the ridge axis associated with overlapping spreading centers can be complex.

Finally, it is notable that highly depleted lava compositions are known from small intra-transform spreading centers in major transform zones, such as the Garrett (Sinton et al., 1991; Mahoney et al., 1994; Wendt et al., 1999), Siqueiros (Perfit et al., 1996) and the Galápagos Transform (G-PRIME dredge 2, see Detrick et al., 2002; Cushman et al., 2004; Ingle et al., in prep). The depleted character of these lavas is commonly attributed to tapping of shallow, previously melt-depleted mantle. Although there is considerable uncertainty concerning the dynamics of mantle upwelling beneath migrating, propagating and overlapping spreading centers, geochemical evidence supports the hypothesis that previously depleted mantle is preferentially melted in such regions. Incomplete melt focusing might also explain the presence of incompatible-element-depleted lavas in OSCs and transform zones, but it is not possible to evaluate whether or not this is more or less likely to occur with complicated ridge geometries.

5. Conclusions

1. The propagating OSC at 93.25˚W on the GSC differs significantly from the 'classic' 95.5˚W propagating rift, primarily in the eruption of T-MORB rather than N-MORB, the presence of high-Mg lavas within the overlap zone, rather than the pronounced increase in fractionation along the propagating rift at 95.5˚W, and shallow overlapping ridges, versus deep axes along the propagating and failing rifts at 95.5˚W. Some of these differences may be attributed to differences in propagation rate (70 mm/yr vs. 48 mm/yr),

proximity to the Galápagos hotspot, and for the fact that the 93.25˚W PR is breaking through younger and thicker crust (260 ka, 6.4 km thick vs. 910 ka and 5.7 km thick).

2. Compared to ridge segments outside the overlap zone, lavas from the ODR and sample 40-2 from the OPR are much less differentiated, with higher MgO, lower overall incompatible element abundances, and less pronounced negative depletions in Sr.

3. Data for the study area fall within, and encompass, 50-60% of the total range of the nearly linear arrays of isotopic ratios for the western GSC. The near-linearity of these arrays suggests source mixing primarily between two components with different isotopic ratios.

4. Incompatible trace element ratios correlate well with isotopic ratios, allowing samples to be separated into three geochemical types: relatively incompatible-element enriched T-MORBs (the eT group, samples 29-1, 39-1, 50-1), relatively incompatible-element depleted T-MORBs (the dT group, 43-1, 48-1, 51-1), and normal T-MORBs (the nT group, all other samples). The presence of all three geochemical types in all four regions of the study area indicates that the two principal mantle components are present throughout the study region. There is no requirement for variation of the distribution of these components along axis. Rather, the smooth gradients in isotopic ratios outside the overlap zone could reflect melting processes within a uniformly heterogeneous mantle.

5. The presence of significant variations in extent of low-pressure fractionation and parental magma compositions over short along-axis distances suggests that magma chambers that fed eruptions in this region are likely to be small, discontinuous and/or poorly mixed over distances less than our sample spacing of about 10 km.

6. High-Mg, crystal-rich lavas containing multiple populations of plagioclase and olivine with significant variation from grain interior to exterior, and significantly out of equilibrium with their host glasses, suggests that overlap limb lavas originated from magma chambers characterized by overall low melt supply. This result suggests that the high magma-supply model for some OSCs is not appropriate for this offset.

7. The long-wavelength along-axis geochemical gradient apparent for the entire western GSC (e.g. in $^{206}Pb/^{204}Pb$, Nb/Zr, Nb/La) is also present in the study area but is interrupted by geochemical variability in the overlap zone. These gradients are best seen in the more numerous nT group but sympathetic variations are observed for the eT and dT samples. Propagating rift samples show a decrease in incompatible trace element ratios from east to west, as the OSC is approached, consistent with the idea that magmatic processes continue to evolve for long distances behind the initial rifting through old lithosphere. This trend is interrupted inside the OPR and a similar trend begins, consistent with an interpretation based on bathymetry for dueling propagation and ridge abandonment in this area. DR samples do not vary beyond the long-wavelength gradation. Within the overlap zone, dying (ODR) rift samples show sharp decreases in incompatible trace element ratios.

8. The presences of lava samples that are highly depleted in the more incompatible elements is a strong feature of the 93.25°W OSC, as well as for some ridge axis discontinuities and intra-transform spreading centers elsewhere. We consider three possible explanations for the generation of incompatible-element depleted lava compositions: (1) increased degrees of melting, (2) melting of an incompatible-element depleted source, or (3) variations in melt migration focusing within the upwelling zone. An increased degree of melting is geologically implausible and inconsistent with chemical, mineralogical and petrographic evidence for low melt supply in the OSC. Although the concept of incomplete melt focusing in the overlap zone is viable, we currently are unable to test this hypothesis. Melting of previously melted mantle is consistent with the geometry of the OSC, such that each limb could be tapping mantle that was previously cycled though the melting zone of the other limb, in the case of the ODR because of its position behind the OPR wake and at the OPR because of the northeastern migration of the ridge over the mantle.

Chapter 2: Mantle Source Compositions

1. Introduction

Chemical variations among lava samples of the GSC 92-94°W study region require different parental magmas for each of the three chemical types: eT-, nT- and dT-MORB. Because characteristic incompatible element ratios of these types also correlate with radiogenic isotope ratios, the differences in parental magma compositions are likely to have been inherited from melting of mantle sources that are chemically, as well as isotopically different. Although the isotopic characteristics of mantle sources contributing to GSC magmas are reasonably well known (e.g. Ingle et al., in prep.), the trace element compositions are much less well constrained. We therefore have attempted to quantify the chemical compositions of sources that have contributed to the different chemical types.

The determination of source composition from the composition of lavas is a multi-step process, each step requires certain assumptions about the processes that have taken place. For example, lavas have differentiated from parental magmas, which in turn have evolved from the primary magmas created during partial melting. Melting processes themselves can be complex, depending on the mineralogy of the mantle and ways in which melts are extracted and accumulated to form magmas entering the crust. The approach presented here involves a number of simplifying assumptions to the processes involved. Although more sophisticated models are possible, each requires additional assumptions to be made. The procedure outlined below uses some of the simpler equations available (e.g., accumulated modal fractional melting) in order to avoid making additional assumptions about parameters which are unknown.

2. Methods

We used the thermodynamically based MELTS algorithms (Ghiorso and Sack, 1995) contained within Adiabat_1ph (Smith and Asimow, 2005) to model fractionation, assuming that low-pressure fractional crystallization was the only process that relates primary magmas to lava compositions. Fractionation was modeled at 1000 bars and at the oxygen fugacity represented by the faylite-magnetite-quartz (FMQ) buffer -2 log units. Through trial and error we determined major element compositions of parental melts that have only olivine on the liquidus, which, when fractionated, produce liquid compositions similar to those of each of the main chemical types (Table 6, Appendix F). A primary melt was then determined from each parental melt by reversing the fractionation process and adding equilibrium olivine back into the system in 2% increments. The olivine added to the liquid at each step was the equilibrium olivine composition calculated using MELTS. This procedure was repeated until the olivine in equilibrium with the liquid attained a mol. % forsterite composition of 90.5 ($Fo_{90.5}$), similar to that of abyssal peridotite olivine (K. T. M. Johnson, pers. comm.., 2007). The liquid composition in equilibrium with $Fo_{90.5}$ was assumed to be in equilibrium with residual mantle, and therefore representative of primary magma. The total amount of olivine fractionation between primary and parental magmas was found to range from 18% to 19.5% for the three types. Using the calculated primary melt major element compositions, we repeated a similar process of trial and error to find the incompatible trace element compositions of the primary mantle components (Table 6, Appendix G).

Table 6. Model Compostion of the Three Mantle Components Beneath the Study Area

	dT-MORB (Nb/Zr <0.06)			nT-MORB (Nb/Zr 0.06-0.08)			eT-MORB (Nb/Zr >0.08)		
	Parent	Primary	Source	Parent	Primary	Source	Parent	Primary	Source
SiO_2	49.8	48.3	-	49.6	48.1	-	49.7	48.1	-
Al_2O_3	16.1	13.4	-	15.9	13.2	-	15.9	13.3	-
FeO*	7.80	8.41	-	8.20	8.79	-	8.09	8.673	-
MnO	0.14	0.15	-	0.14	0.15	-	0.13	0.135	-
MgO	9.64	15.9	-	9.64	16.1	-	9.64	15.90	-
CaO	13.8	11.5	-	13.5	11.3	-	13.6	11.4	-
Na_2O	1.78	1.48	-	1.78	1.48	-	1.78	1.48	-
Cr_2O_3	0.07	0.06	-	0.07	0.06	-	0.07	0.06	-
TiO_2	0.79	0.66	-	0.84	0.69	-	0.88	0.73	-
K_2O	0.05	0.04	-	0.07	0.06	-	0.08	0.07	-
P_2O_5	0.05	0.04	-	0.07	0.06	-	0.08	0.06	-
H_2O	0.08	0.07	-	0.13	0.11	-	0.14	0.12	-
	Parent	Primary	Source	Parent	Primary	Source	Parent	Primary	Source
Rb	-	0.75	0.11	-	1.48	0.21	-	1.85	0.27
Ba	-	10.2	1.48	-	16.96	2.46	-	23.00	3.34
Th	-	0.10	0.01	-	0.19	0.03	-	0.25	0.04
U	-	0.03	0.00	-	0.06	0.01	-	0.07	0.01
Nb	-	1.43	0.21	-	2.63	0.38	-	3.41	0.49
Ta	-	0.09	0.01	-	0.16	0.02	-	0.21	0.03
La	-	1.32	0.19	-	2.20	0.32	-	2.54	0.37
Ce	-	3.70	0.54	-	5.59	0.81	-	6.13	0.89
Pb	-	0.19	0.03	-	0.23	0.03	-	0.24	0.03
Pr	-	0.62	0.09	-	0.91	0.13	-	0.93	0.14
Sr	-	58	8.43	-	72.8	10.58	-	89	12.93
Nd	-	3.40	0.50	-	4.67	0.68	-	4.81	0.70
Sm	-	1.24	0.19	-	1.57	0.23	-	1.57	0.23
Zr	-	30	4.39	-	39.2	5.73	-	39.2	5.73
Hf	-	0.85	0.12	-	1.09	0.16	-	1.06	0.15
Eu	-	0.48	0.07	-	0.56	0.08	-	0.56	0.08
Gd	-	1.67	0.26	-	1.97	0.30	-	1.92	0.30
Tb	-	0.34	0.05	-	0.39	0.06	-	0.37	0.06
Dy	-	2.25	0.38	-	2.62	0.44	-	2.53	0.43
Y	-	15.2	2.65	-	16.20	2.83	-	16.55	2.89
Ho	-	0.51	0.09	-	0.57	0.10	-	0.56	0.10
Er	-	1.50	0.27	-	1.67	0.30	-	1.64	0.30
Yb	-	1.48	0.29	-	1.66	0.32	-	1.59	0.31
Lu	-	0.23	0.05	-	0.26	0.05	-	0.24	0.05

Modeled using the MELTS and Adiabat_1ph algorithms at 1000 bars and with mantle oxygen fugacity of FMQ -2 (Ghorso and Sack, 1995; Smith and Asimow, 2005). Rb, Ba, Sr and Eu were modeled with variable distribution coefficients (Ds), all others with constant Ds of McKenzie and O'Nions (1991; 1995) as is the default in the MELTS algorithm.

In order to convert primary magma composition to source composition, one must estimate, or know, the extent of melting and the nature of the melting process. Because we have few constraints on modes of potential mantle lithologies in this area, we have elected to use the accumulated fractional (modal) melting equation $C_L=(C_o/F)[1-(1-F)^{1/D}]$, (Shaw, 1970; Wood and Fraser, 1976) and the suggested bulk distribution coefficients of McKenzie and O'Nions (1991). C_L is the concentration of a trace element in the primary liquid relative to that in the source (C_o) before melting, F is the total melt fraction and D is the bulk distribution coefficient. With this equation one can calculate the source composition (C_o), if the amount of melting (F) can be estimated. Previous work, notably by Klein and Langmuir (1987) and Langmuir et al. (1992), has shown that extents of melting for MORB globally can be estimated from liquid Na_2O content. Although our three chemical types have important differences in some incompatible elements, it is notable that they have similar Na_2O values at similar MgO (Figure 13) and each type has a calculated primary Na_2O content of 1.48 wt % (Table 6). We therefore assume that constant primary Na_2O represents similar extents of melting for each type.

Using a source Na_2O content of 0.21 wt% for Galápagos T-MORB from Cushman et al. (2004) and a D of 0.03 from Langmuir et al. (1992), as used by Cushman et al. (2004), the amount of melting (F) required to produce melts with 1.48 wt % Na_2O is 14%. Although this value is higher than some recent estimates for normal MORB, e.g. 5% or 8% (Workman and Hart, 2005; Boyet and Carlson, 2006, respectively), these lavas are T-MORB, not normal MORB, and this region is characterized by thicker than normal ocean crust (6.4 km). Thus, the determined value of F is considered reasonable. This value is input into the accumulated fractional (modal) melting equation to calculate C_o

values for all trace elements using the proposed bulk D values of Workman and Hart (2005).

3. Results

Calculated incompatible-element compositions for the three mantle types are given in Table 6, and shown in Figure 17. Fractionated assemblages are clinopyroxene, plagioclase and minor spinel for all three mantles. For the most part, parent melt major elements do not differ significantly between the three modeled mantle types, in contrast to the behavior of the more incompatible minor element oxides K_2O, P_2O_5 and H_2O. This result provides further support for assuming a constant 14% melting for all three types. Incompatible trace elements also differ among the three modeled mantle types (Figure 17). Because the nT-MORB group contains the most samples, the source mantle for this group is the best constrained. Primitive-mantle-normalized plots, using values of Sun and McDonough (1989), show the eT-MORB source to be more similar to the nT-MORB source than the dT-MORB source. Both the dT-MORB and eT-MORB source types have a small Sr and Ba spike and a distinctive Nb and Ta hump, which is common for western GSC samples in the E- and T-MORB regions (Ingle et al., in prep). Notably, the mantle source lacks the Sr anomaly trough that is present in the sample data. This Sr anomaly can be produced with fractionation of the primary magmas of the three source types using MELTS (Figure 18). In comparison to the average depleted MORB mantle compositions proposed by Workman and Hart (2005) and Salters and Stracke (2004), our calculated mantle compositions have higher light rare earth element contents and lower heavy rare

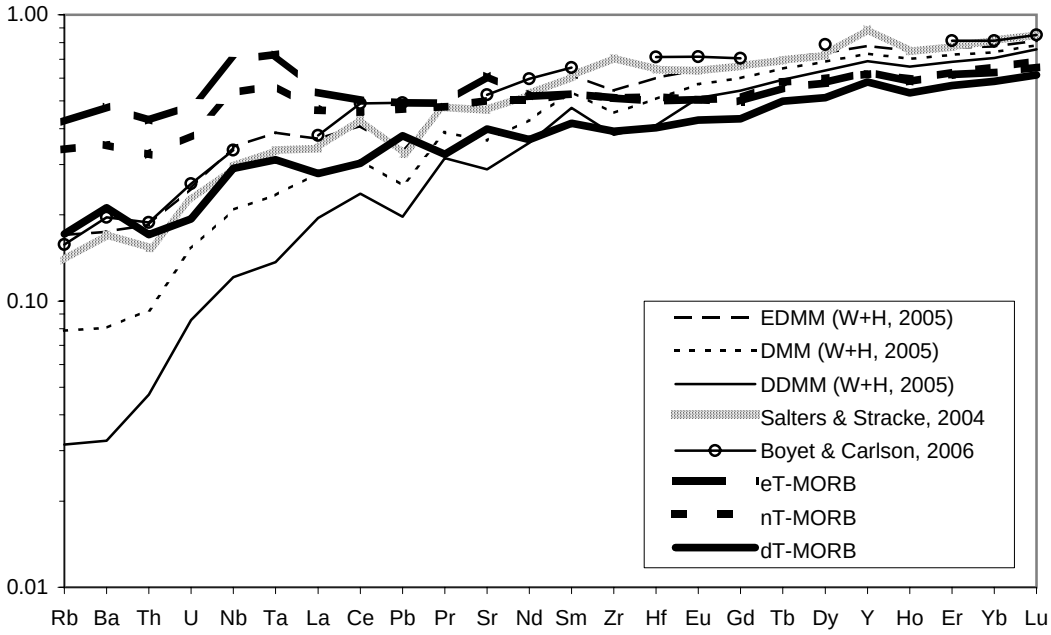

Figure 17. Primitive-mantle-normalized incompatible element patterns for modeled mantle source types in the study area compared to general MORB-source mantle compositions proposed by Workman and Hart (2005), Salters and Stracke (2004), and Boyet and Carlson (2006). Primitive-mantle normalizing values are those of Sun and McDonough (1989).

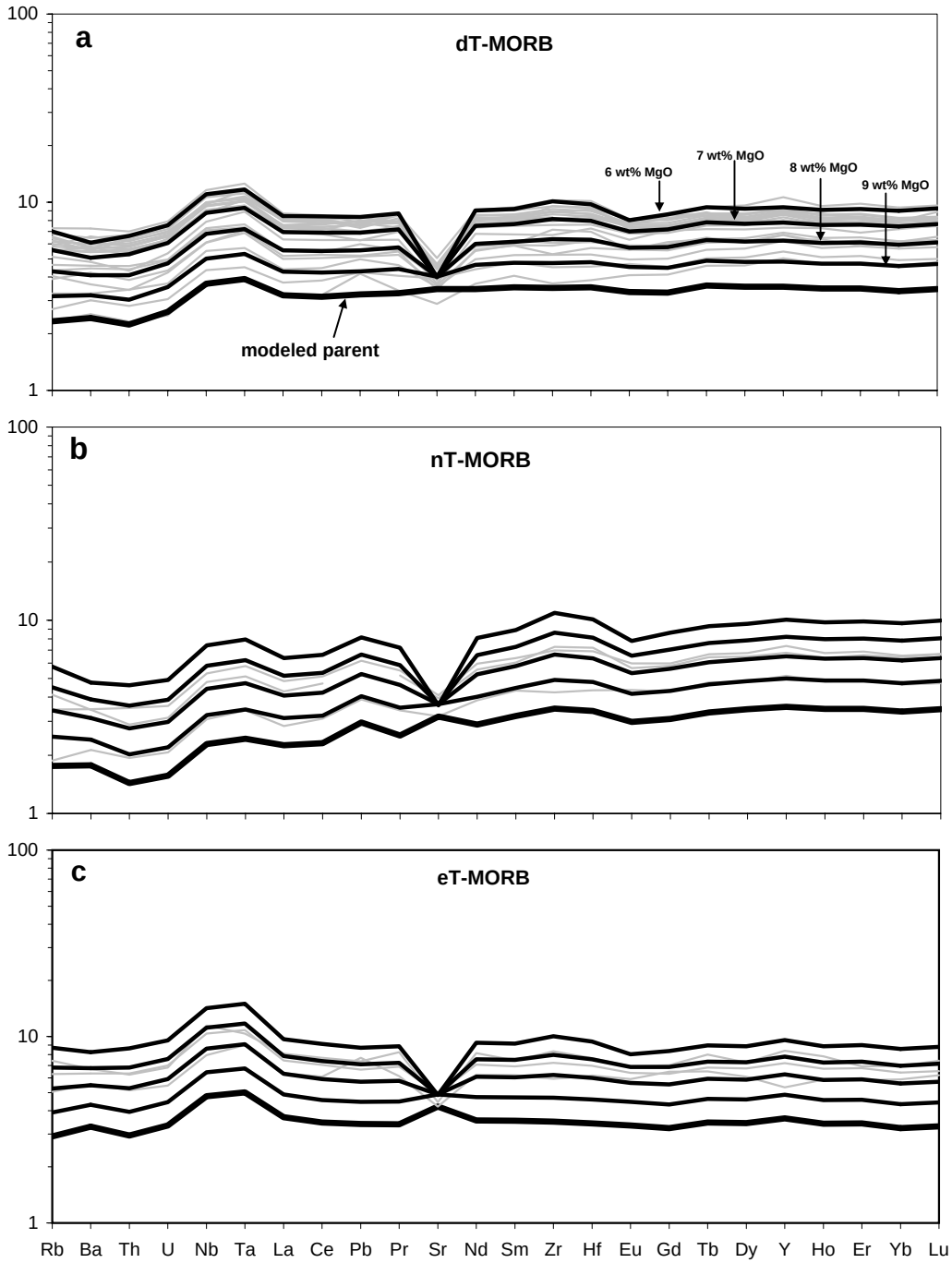

Figure 18. Fractionating the parent for each mantle type to show that the Sr depletion in study area lavas (thin gray lines) can be explained by plagioclase fractionation of a source without Sr depletion. Modeled parent magma compositions are represented by the heavy black lines (see text for how compositions were achieved). The thinner black lines show the results of fractionating the parent using MELTS to 9wt%, 8wt%, 7wt% and 6wt% MgO in the liquid. All data are normalized to the estimated primitive mantle of Sun and McDonough (1989).

earth element contents, possibly reflecting the involvement of garnet during melting, close to the Galápagos hotspot; our model assumes no melting in th garnet stability zone. The three mantle types from the study area lack the positive Sm and Ce anomaly and negative Pb anomaly seen in the Workman and Hart (2005) and Salters and Stracke (2004) primitive mantle normalized patterns. The Ba spike in the study area is also seen in Salters and Stracke's (2004) proposed mantle. The positive Sr anomaly seen in the dT- and eT-MORB sources but not the nT-MORB source may reflect analytical uncertainties as the average primary magma for these types is less well constrained because of a fewer number of samples.

When plotted on a $^{206}Pb/^{204}Pb$ vs. Nb/Zr diagram the study area data do not follow the same trend as the Workman and Hart (2005) average values for model depleted MORB mantle (Figure 19). Instead they plot on a steeper trend in which the enriched (high-Nb/Zr) end-member isotopic values approach those for the proposed common or 'C' mantle component (Hanan and Graham, 1996) possibly indicating the presence of this mantle component in the study area. A detailed discussion of the trace element and isotopic nature of the western GSC can be found in Ingle et al. (in prep).

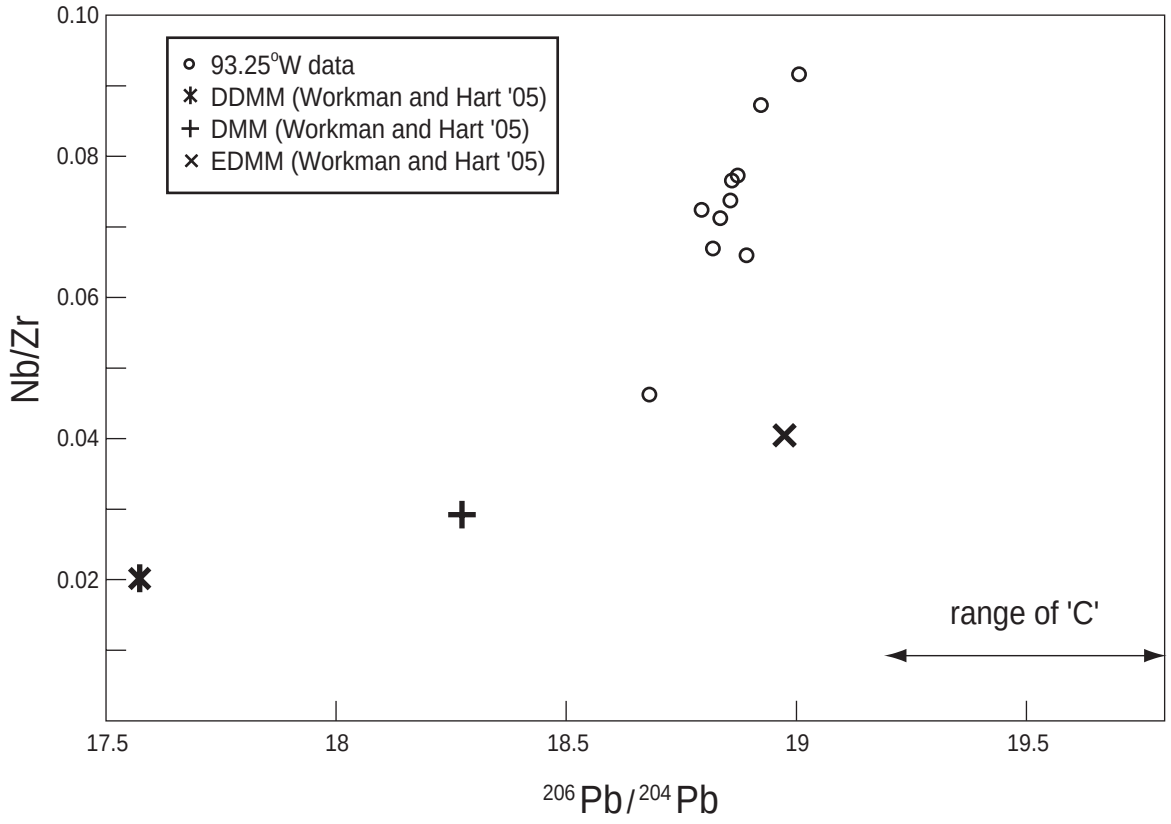

Figure 19. Comparison of study area data to model manlte compositions proposed by Workman and Hart (2005). Notice that our data plot oblique to the Workman and Hart trend, with values for the "enriched" samples approaching the $^{206}Pb/^{204}Pb$ values of the proposed common or 'C' mantle component (Hanan and Graham, 1996).

4. Summary and Conclusions

The geochemical variations in lavas from the 93.25˚W OSC on the GSC require variations in source compositions, which probably represent a mixture of relatively incompatible-element enriched and depleted components. To constrain the trace element compositions of these mixtures, we determined suitable parental compositions, with only olivine on the liquidus at low pressure, which will reproduce the data trends for the three types of T-MORB with low-pressure fractionation using MELTS. These parental magmas were then back-fractionated to equilibrium with $Fo_{90.5}$ olivine, and then assuming 14% accumulated modal fractional melting, mantle source compositions were determined.

Although there are considerable uncertainties to our derived mantle compositions, this is the first attempt in quantifying the mantle source for T-MORB, which can then be compared to the much better constrained mantle compositions giving rise to normal MORB (e.g., Salters and Stracke, 2004; Workman and Hart, 2005; Boyet and Carlson, 2006).

Our derived Galápagos T-MORB mantle differs from the model depleted MORB mantle (DMM) of Workman and Hart (2005) in the presence of a pronounced Nb – Ta hump in the mantle-normalized patterns, a characteristic of all western GSC E- and T-MORB (Ingle et al., in prep), and in isotopic and incompatible trace element ratios. Comparison of $^{206}Pb/^{204}Pb$ and Nb/Zr shows the study area samples to lie on a trend dissimilar to the Workman and Hart (2005) average model mantle types. The high Pb

isotopic ratios in the study area samples possibly suggest that a common- or ‘C’-type mantle may be involved in the sources of the region. An important conclusion of this study is that the strong negative Sr anomaly found in western GSC T-MORB can be explained entirely by plagioclase fractionation and does not require an anomalously low Sr content in the underlying mantle (Figure 18).

Appendix A. Glass Compositions for all Study Area Samples used to to Define the Chemical Groups of Cushman et al. (2004)

Sample	SiO_2	TiO_2	Al_2O_3	FeO*	MnO	MgO	CaO	Na_2O	K_2O	P_2O_5
29-1	50.5	1.70	13.9	11.8	0.21	6.84	11.3	2.43	0.15	0.13
29-2	50.5	1.64	13.9	11.7	0.21	6.83	11.3	2.43	0.16	0.14
29-3	50.3	1.66	13.9	11.7	0.19	6.85	11.2	2.46	0.17	0.13
29-4	50.5	1.66	13.9	11.8	0.21	6.86	11.2	2.39	0.16	0.15
29-5	50.4	1.68	13.8	11.9	0.20	6.80	11.2	2.41	0.16	0.15
31-1	50.0	1.83	13.7	12.5	0.19	6.38	10.9	2.60	0.18	0.17
31-2	50.1	1.84	13.6	12.4	0.21	6.44	10.8	2.63	0.18	0.15
31-3	50.2	1.82	13.7	12.5	0.20	6.43	10.8	2.68	0.17	0.14
31-4	50.0	1.80	13.7	12.5	0.23	6.43	10.8	2.60	0.18	0.13
32-1	50.3	1.63	13.7	12.4	0.22	6.81	11.1	2.23	0.14	0.13
32-2	50.2	1.69	13.6	12.4	0.22	6.78	11.1	2.19	0.14	0.14
33-1	50.5	1.60	13.7	12.6	0.23	6.69	10.9	2.29	0.14	0.13
33-2	50.6	1.61	13.6	12.5	0.23	6.70	10.9	2.35	0.14	0.13
33-3	50.4	1.61	13.7	12.6	0.21	6.71	10.9	2.31	0.15	0.14
33-4	50.4	1.62	13.7	12.6	0.24	6.74	11.0	2.32	0.15	0.14
33-5	50.2	1.58	13.7	12.6	0.22	6.75	10.9	2.31	0.14	0.13
33-6	50.4	1.61	13.7	12.5	0.22	6.72	10.8	2.32	0.14	0.12
34-1	50.0	1.51	14.2	11.5	0.21	7.23	11.7	2.20	0.13	0.13
34-5	50.5	1.47	14.3	11.4	0.22	7.21	11.8	2.29	0.13	0.12
34-2	50.6	1.51	14.1	11.7	0.20	7.11	11.7	2.36	0.13	0.14
34-3	50.4	1.50	14.1	11.7	0.19	7.13	11.7	2.33	0.13	0.14
34-4	50.6	1.56	14.0	11.7	0.19	7.02	11.6	2.33	0.14	0.14
35-1	50.6	1.74	13.9	12.5	0.23	6.50	11.2	2.52	0.14	0.15
35-4	50.5	1.75	13.7	12.5	0.22	6.51	11.1	2.56	0.14	0.14
35-2	50.8	1.81	13.5	12.8	0.24	6.40	11.2	2.59	0.15	0.15
36-1	50.8	1.57	14.1	11.8	0.21	7.06	11.3	2.34	0.15	0.16
37-1	50.9	1.32	14.3	11.1	0.19	7.29	12.1	2.24	0.11	0.11
37-2	51.0	1.33	14.3	11.2	0.21	7.33	12.0	2.27	0.11	0.12
37-3	50.9	1.33	14.3	11.1	0.21	7.32	12.1	2.27	0.12	0.11
37-4	50.8	1.33	14.4	11.2	0.20	7.34	12.1	2.23	0.11	0.10
38-1	50.8	1.72	13.8	12.4	0.21	6.70	11.3	2.31	0.15	0.17
38-2	50.8	1.71	13.8	12.4	0.22	6.71	11.3	2.33	0.15	0.16
38-3	50.9	1.72	13.8	12.4	0.23	6.62	11.3	2.34	0.14	0.17
39-2	51.0	1.70	13.8	12.5	0.23	6.54	11.1	2.45	0.16	0.15
39-3	50.9	1.73	13.8	12.5	0.20	6.60	11.3	2.36	0.14	0.16
39-1	50.9	1.44	14.4	11.0	0.19	7.37	12.2	2.29	0.16	0.13
40-1	50.4	0.98	15.4	9.5	0.17	8.68	13.3	1.96	0.07	0.09
40-2	50.5	0.99	15.3	9.5	0.17	8.71	13.2	1.99	0.07	0.08
40-3	50.3	0.98	15.2	9.5	0.16	8.67	13.2	1.97	0.07	0.08
40-4	50.3	1.02	15.3	9.5	0.16	8.65	13.2	1.95	0.07	0.08
40-5	50.3	0.99	15.3	9.5	0.17	8.65	13.3	1.94	0.07	0.07
41-1	50.8	1.38	14.2	11.5	0.20	7.27	11.9	2.26	0.12	0.13
41-3	50.8	1.35	14.5	11.2	0.20	7.55	11.9	2.27	0.11	0.12
41-4	50.6	1.31	14.5	11.2	0.22	7.56	12.0	2.25	0.11	0.12
41-5	50.8	1.31	14.5	11.2	0.20	7.57	12.0	2.27	0.11	0.13

Analyses collected using the University of Hawai'i Cameca SX-50 electron microprobe and methods described in Cushman et al. (2004). All values in wt%. FeO* is total Fe as FeO. Samples are separated into geochemical groups defined by Cushman et al. (2004).

Appendix A (Continued). Glass Compositions for all Study Area Samples used to to Define the Chemical Groups of Cushman et al. (2004)

Sample	SiO_2	TiO_2	Al_2O_3	FeO*	MnO	MgO	CaO	Na_2O	K_2O	P_2O_5
41-6	50.7	1.23	14.6	11.0	0.19	7.68	12.2	2.22	0.10	0.11
41-7	50.7	1.23	14.6	10.9	0.21	7.72	12.2	2.21	0.11	0.11
42-1	50.8	0.77	14.9	9.2	0.18	8.91	13.6	1.65	0.05	0.06
42-3	50.7	0.76	14.9	9.3	0.18	8.90	13.6	1.69	0.05	0.06
42-2	50.7	0.84	14.9	9.6	0.18	8.82	13.3	1.70	0.06	0.07
42-4	50.8	0.87	14.8	9.6	0.18	8.75	13.3	1.75	0.06	0.07
43-1	50.4	0.88	14.9	9.2	0.18	8.70	13.5	1.91	0.04	0.05
43-2	50.3	0.90	14.9	9.3	0.18	8.70	13.5	1.90	0.04	0.04
44-1	49.5	1.10	15.5	9.9	0.18	8.58	12.5	2.10	0.08	0.07
45-1	50.2	1.25	15.0	10.3	0.17	8.15	12.0	2.27	0.09	0.07
45-2	50.2	1.24	15.0	10.4	0.18	8.09	12.0	2.25	0.09	0.07
45-3	50.3	1.28	14.9	10.4	0.17	7.84	12.0	2.29	0.09	0.08
46-1	50.8	1.23	14.5	10.4	0.19	7.86	12.4	2.18	0.10	0.09
46-2	50.8	1.25	14.5	10.4	0.19	7.82	12.4	2.17	0.11	0.08
47-1	50.6	1.66	13.9	12.1	0.21	6.71	11.2	2.50	0.16	0.13
48-4	50.6	1.66	13.9	12.1	0.24	6.72	11.2	2.53	0.16	0.13
48-1	50.4	1.20	14.8	10.3	0.20	8.06	12.5	2.21	0.07	0.07
48-2	50.2	1.17	14.8	10.3	0.19	8.05	12.5	2.25	0.07	0.07
48-3	50.3	1.17	14.8	10.3	0.19	8.05	12.5	2.25	0.07	0.07
49-1	50.7	1.74	13.6	12.6	0.22	6.57	10.8	2.57	0.15	0.11
49-2	50.7	1.73	13.6	12.8	0.23	6.60	10.9	2.57	0.15	0.12
50-1	50.6	1.31	14.6	10.5	0.19	7.83	12.2	2.24	0.13	0.10
50-2	50.7	1.32	14.5	10.5	0.20	7.77	12.2	2.24	0.14	0.11
50-3	50.7	1.31	14.6	10.5	0.20	7.83	12.2	2.24	0.13	0.10
50-4	50.7	1.34	14.5	10.5	0.20	7.78	12.1	2.26	0.14	0.10
50-5	50.5	1.34	14.5	10.4	0.19	7.77	12.2	2.23	0.14	0.10
51-1	50.7	1.30	14.4	10.6	0.19	7.69	12.4	2.36	0.09	0.08
51-2	50.5	1.29	14.4	10.7	0.21	7.70	12.5	2.32	0.09	0.08
51-3	50.7	1.30	14.4	10.7	0.21	7.69	12.5	2.33	0.09	0.06
53-1	51.0	1.96	13.2	13.3	0.21	6.09	10.6	2.53	0.15	0.13
53-2	51.0	1.94	13.3	13.4	0.23	6.07	10.6	2.59	0.14	0.13
53-3	50.9	1.95	13.2	13.4	0.23	6.07	10.6	2.59	0.15	0.15
53-4	50.8	1.92	13.3	13.3	0.23	6.15	10.6	2.50	0.15	0.14
Precision	0.1	0.015	0.05	0.06	0.01	0.07	0.05	0.03	0.01	0.01

Analyses collected using the University of Hawai'i Cameca SX-50 electron microprobe and methods described in Cushman et al. (2004). All values in wt%. FeO* is total Fe as FeO. Samples are separated into geochemical groups defined by Cushman et al. (2004).

Appendix B. Petrographic Description of All Samples with Mineral Probe Data

29-1

Plagioclase (2%) occurs mainly as elongated glomerophyric microphenocryst laths (gloms) intergrown with subhedral to anhedral clinopyroxene and sometimes as euhedral plagioclase-only intergrowths. Solitary quenched microphenocrysts laths averaging 0.2 mm in length occur throughout the groundmass and glass. Plagioclase phenocrysts occur as euhedral grains up to 0.8 mm in length. Phenocrysts either have a thin visibly zoned rim or contain no zoning. Clinopyroxene (1%) mainly occurs as glomerophyric intergrowths with plagioclase (gloms) and rarely as subhedral to anhedral solitary grains (0.1mm), similar in size to those intergrown with plagioclase. One small euhedral grain of olivine was identified and subsequently probed. Vesicles account for 2% of the thin section, very fine indiscernible cryptocrystalline groundmass and glass account for the remainder.

31-1

This thin section was point counted and used as a reference for making visual estimates of modes for other samples. Plagioclase (1.65%) occurs as euhedral and skeletal laths up to 2 mm in length, as glomerophyric intergrowths (gloms) with subhedral to anhedral clinopyroxene or euhedral olivine, or as solitary glomerophyric quenched microphenocryst laths up to 0.1 mm in length throughout the groundmass and glass. Plagioclase phenocrysts either have a thin visibly zoned rim or contain no visible zoning. Clinopyroxene (0.85%) occurs mainly intergrown with plagioclase as 0.1 mm to 0.4 mm

subhedral to anhedral gloms. Some clinopyroxene and plagioclase gloms are clustered and intergrowing with each other over areas 2.8 mm in diameter. Olivine occurs as euhedral to highly skeletal grains either intergrowing with plagioclase or as solitary grains. Olivine grains range in size from 0.1 mm to 1.1 mm. Vesicles account for 2.65% of the thin section, very fine discernable cryptocrystalline groundmass and glass account for the remainder.

34-4

Plagioclase (8%) occurs in several forms, as small elongated to skeletal laths, as medium euhedral zoned and non zoned laths and as large euhedral to subhedral grains, all of which can be solitary or intergrown with olivine. One large grain (2.6 mm) displays 'sieve texture' in which a plagioclase core is mantled with a zone of poikilitic textured plagioclase, which is in turn mantled with an outermost euhedral rim of plagioclase (Figure 3). Microprobe analyses show the core to have an Anorthite content of 87 mol. % and the rim to have an Anorthite content of 75 mol. %. Several grains have complex visible zoning patterns, some grains display no visible zoning. Olivine (3%) occurs as euhedral, subhedral and skeletal grains ranging from 0.1 mm to 1 mm and commonly is intergrown with plagioclase grains. Some grains display rounded edges and nearly all grains contain void spaces. Many plagioclase and olivine grains contain small inclusions up to 0.06 mm distributed randomly throughout the grain. No clinopyroxene was identified in thin section. Vesicles account for less than 1% of the thin section, very fine discernable cryptocrystalline groundmass and glass account for the remainder.

38-2

This thin section was point counted and used as a reference for making visual estimates of modes for other samples. Plagioclase (8.55%) occurs in several forms, as small elongated to skeletal laths averaging 0.6 mm by 0.08 mm, as large euhedral phenocrysts ranging from 0.6 mm to 3 mm in length and ranging from complexly visibly zone to non-visibly zoned, and as small elongated glomerophyric laths intergrown with clinopyroxene (gloms). Clinopyroxene (5.75%) occurs either as subhedral to anhedral solitary grains up to 1.5 mm, or as small anhedral grains intergrowing with plagioclase. One large subhedral clinopyroxene grain is mantled with sieve textured plagioclase. Olivine (1.7%) occurs as euhedral to highly skeletal grains up to 1.25 mm in length sometimes intergrowing with plagioclase laths. Plagioclase and clinopyroxene gloms range from single plagioclase and clinopyroxene grains intergrowing, to loose clusters with approximately 50% interstitial matrix, to large tight clusters with little interstitial matrix up to 1.8 mm in length. Vesicles account for 3.2% of the thin section and range from rounded to irregular, very fine discernable cryptocrystalline groundmass and glass account for the remainder.

39-1

Plagioclase (6%) occurs mainly as small elongated microphenocryst laths averaging 0.2 mm in length which are either solitary or intergrowing with anhedral clinopyroxene or with other plagioclase laths. Larger plagioclase grains up to 0.8 mm occur as solitary grains or intergrowing with other large plagioclase grains and are both visibly zoned and non-visibly zoned. Olivine (1%) occurs mainly as euhedral to subhedral solitary grains

up to 0.22 mm. Clinopyroxene (3%) occurs as either small subhedral to anhedral grains intergrowing with plagioclase or as large subhedral to euhedral phenocrysts up to 1.4 mm in longest dimension. Vesicles account for 1% of the thin section and range from rounded to irregular. Very fine discernable cryptocrystalline groundmass and glass account for the remainder.

40-2

Visual inspection of the thin section without magnification shows the sample matrix is not uniform throughout. Inspection under low magnification (5 times power) shows there to be two variations of matrix, a salt and pepper looking speckled matrix and a light brown, feathery radiating-type matrix. Plagioclase (9%) occurs in several forms, as large (up to 2.6 mm) euhedral to subhedral grains with mild thin visible zoning on the grains rims, or as complexly visibly zoned grains, or as non-visibly zoned grains. Several plagioclase grains display sieve texture, one such grain is mantled with a zone of poikilitic texture, which is in turn mantled with an outermost euhedral rim (1 mm). Another grain displays sieve texture throughout it's core with a non-sieve textured euhedral rim (1.6 mm). Clinopyroxene (<1%) occurs mainly as small anhedral grains intergrowing with plagioclase and rarely as large grains up to 0.3 mm intergrowing with plagioclase and olivine. Olivine (3%) commonly occurs as subhedral to highly skeletal grains intergrowing with plagioclase laths and sometimes as euhedral to skeletal solitary grains up to 0.6 mm. Vesicles account for 1% of the thin section and range from round grains 3.4 mm in diameter, to highly irregular and elongate grains. The discernable groundmass described above and glass account for the remainder.

42-4

Inspection under low magnification (5 times power) shows there to be two variations of matrix, a salt and pepper looking speckled matrix and a light brown feathery radiating looking matrix The salt and pepper looking material sometimes surrounds grains or clusters of grains. Plagioclase (2%) occurs mainly as solitary euhedral zoned grains up to 2 mm, and less commonly as elongated laths intergrowing with anhedral clinopyroxene or olivine. Microphenocrysts are rare and randomly distributed throughout the thin section. Some plagioclase grains (0.5 mm) contain abundant inclusions. Olivine (1%) occurs as small (0.3 mm) solitary skeletal grains, small (0.14 mm) solitary euhedral grains, as subhedral grains intergrowing with plagioclase and as large (1.1 mm) euhedral to subhedral grains which sometimes have mottled grain boundaries which are surrounded with small (0.06 mm) plagioclase microphenocrysts. Clinopyroxene (<<1%) occurs as anhedral grains intergrowing with plagioclase. Vesicles account for <1% of the thin section and are mainly round. The discernable groundmass described above and glass account for the remainder.

43-1

Matrix is mostly glass, few microphenocrysts are present. Glass ranges from clean alteration free to a brown feathery radiating variety. Plagioclase (4%) occurs as subhedral to anhedral elongate laths which can be solitary, in clusters with other plagioclase laths or intergrowing with olivine or clinopyroxene. Visible plagioclase zonation is uncommon in smaller grains but does occur in larger grains. Several large plagioclase grains are up to 2.1 mm. Olivine (2%) occurs as larger (up to 1.5 mm)

subhedral to highly anhedral grains in clusters with plagioclase and sometimes clinopyroxene, as small (0.4 mm) euhedral to subhedral solitary grains and as subhedral to highly skeletal solitary grains up to 1.8 mm. Clinopyroxene phenocrysts (1%) commonly occur intergrowing with plagioclase up to 0.8 mm. Vesicles account for 1% of the thin section and are mostly round to sub-rounded. The glassy groundmass accounts for the remainder.

44-1

This thin section contains abundant alteration free glass with few small olivine phenocrysts and microphenocrysts and very few plagioclase microphenocrysts. A single large (1.5 mm) plagioclase phenocryst occurs in this thin section, and appears to have been undergoing re-melting at the time it was quenched. This grain has retained its euhedral shape and twinning but contains over 50% continuous, evenly spaced tiny glassy blebs (<20μm). Olivine phenocrysts (<1%) are highly skeletal, averaging 0.2 mm. Small round vesicles account for 1% of the thin section, glassy ground mass accounts for the remainder.

Appendix C. Olivine Data

				Oxides (wt%)							Cations based on 4 oxygens							
sample	grain		n	SiO_2	MgO	FeO*	CaO	MnO	NiO	Total	Si	Mg	Fe	Ca	Mn	Ni	Sum	Fo
29-1	9	core	3	38.6	41.2	18.7	0.31	0.31	0.10	99.2	0.996	1.587	0.404	0.009	0.007	0.002	3.004	79.7
		rim	3	38.6	41.7	18.6	0.30	0.27	0.11	99.6	0.993	1.597	0.400	0.008	0.006	0.002	3.007	80.0
31-1	1*	core	3	38.6	39.5	20.2	0.30	0.30	0.11	99.0	1.005	1.532	0.440	0.008	0.007	0.002	2.995	77.7
		rim	4	38.7	39.7	19.8	0.31	0.30	0.08	98.8	1.006	1.540	0.430	0.009	0.007	0.002	2.994	78.2
	2*	core	4	38.8	40.0	19.3	0.29	0.32	0.09	98.8	1.008	1.549	0.419	0.008	0.007	0.002	2.992	78.7
		rim	3	38.6	39.7	19.7	0.30	0.31	0.08	98.7	1.007	1.541	0.429	0.008	0.007	0.002	2.993	78.2
	6	core	3	38.7	39.3	20.5	0.28	0.31	0.06	99.2	1.007	1.525	0.445	0.008	0.007	0.001	2.993	77.4
		rim	3	38.9	39.9	19.5	0.30	0.29	0.09	99.0	1.008	1.544	0.423	0.008	0.006	0.002	2.992	78.5
	10*	core	3	38.9	39.9	19.5	0.29	0.29	0.10	99.0	1.009	1.543	0.423	0.008	0.006	0.002	2.991	78.5
		rim	3	38.8	39.8	19.7	0.31	0.29	0.09	99.0	1.008	1.539	0.429	0.009	0.006	0.002	2.992	78.2
	9	core	3	38.7	39.8	19.6	0.29	0.29	0.10	98.7	1.008	1.543	0.426	0.008	0.006	0.002	2.993	78.4
		rim	2	38.7	39.7	19.8	0.32	0.31	0.08	98.9	1.007	1.539	0.430	0.009	0.007	0.002	2.993	78.1
34-4	2b*	core	4	39.2	42.9	17.3	0.29	0.25	0.14	100.1	0.996	1.625	0.367	0.008	0.005	0.003	3.004	81.6
		rim	3	39.1	42.6	17.8	0.32	0.29	0.14	100.2	0.994	1.615	0.378	0.009	0.006	0.003	3.006	81.0
	4	core	3	39.1	43.7	16.7	0.30	0.27	0.17	100.2	0.990	1.649	0.354	0.008	0.006	0.004	3.010	82.3
		rim	4	38.9	42.6	17.6	0.32	0.28	0.13	99.9	0.993	1.620	0.376	0.009	0.006	0.003	3.007	81.1
	5	core	3	39.1	43.0	17.3	0.29	0.26	0.13	100.1	0.994	1.627	0.368	0.008	0.006	0.003	3.006	81.6
		rim	4	39.1	42.8	17.5	0.32	0.29	0.14	100.1	0.994	1.624	0.372	0.009	0.006	0.003	3.007	81.4
	11	core	3	39.2	43.1	17.0	0.30	0.29	0.15	100.0	0.995	1.631	0.362	0.008	0.006	0.003	3.005	81.8
		rim	4	39.0	42.8	17.2	0.31	0.26	0.14	99.8	0.995	1.627	0.366	0.009	0.006	0.003	3.005	81.6
	12	core	3	39.1	43.1	17.3	0.30	0.26	0.14	100.3	0.993	1.630	0.368	0.008	0.006	0.003	3.007	81.6
		rim	3	39.1	42.8	17.5	0.31	0.27	0.13	100.1	0.994	1.623	0.373	0.008	0.006	0.003	3.006	81.3
	13	core	3	38.9	41.9	18.2	0.30	0.28	0.12	99.7	0.997	1.599	0.391	0.008	0.006	0.003	3.003	80.4
		rim	3	39.0	42.1	18.1	0.31	0.27	0.13	99.9	0.996	1.605	0.387	0.008	0.006	0.003	3.004	80.6
	14	core	3	39.2	43.3	16.7	0.30	0.24	0.13	100.0	0.995	1.639	0.354	0.008	0.005	0.003	3.005	82.2
		rim	3	39.0	42.9	17.3	0.31	0.27	0.14	100.0	0.993	1.628	0.368	0.008	0.006	0.003	3.007	81.6
	15	core	3	39.2	43.6	16.7	0.29	0.25	0.17	100.2	0.993	1.645	0.353	0.008	0.005	0.003	3.007	82.3
		rim	2	39.1	43.0	17.2	0.30	0.26	0.15	100.0	0.994	1.629	0.366	0.008	0.006	0.003	3.006	81.6
36-1	1*	core	6	38.9	41.7	17.6	0.29	0.26	0.13	98.9	1.002	1.601	0.380	0.008	0.006	0.003	2.998	80.8
	7a	core	5	39.0	41.7	17.6	0.30	0.26	0.11	98.9	1.003	1.599	0.378	0.008	0.006	0.002	2.997	80.9
	7b	core	4	39.0	41.6	17.7	0.31	0.27	0.11	99.0	1.003	1.595	0.382	0.009	0.006	0.002	2.997	80.7
	8	core	4	38.8	40.4	19.4	0.28	0.26	0.09	99.2	1.004	1.558	0.419	0.008	0.006	0.002	2.996	78.8
	9	core	4	39.2	41.6	17.7	0.31	0.24	0.12	99.2	1.005	1.592	0.381	0.009	0.005	0.003	2.994	80.7
	12	core	3	38.9	41.7	18.1	0.29	0.28	0.12	99.4	0.999	1.597	0.389	0.008	0.006	0.002	3.001	80.4
38-2	5	core	3	38.9	41.9	17.6	0.29	0.26	0.11	99.1	1.000	1.607	0.378	0.008	0.006	0.002	3.000	81.0
		rim	3	39.0	41.2	18.3	0.29	0.28	0.13	99.2	1.004	1.580	0.394	0.008	0.006	0.003	2.996	80.0
	11*	core	3	39.0	40.9	18.9	0.30	0.30	0.10	99.5	1.003	1.570	0.408	0.008	0.006	0.002	2.997	79.4
		rim	3	38.8	40.4	19.3	0.30	0.31	0.11	99.3	1.004	1.558	0.418	0.008	0.007	0.002	2.996	78.9
	12	core	3	38.8	40.5	19.3	0.26	0.28	0.17	99.3	1.003	1.561	0.417	0.007	0.006	0.004	2.997	78.9
		rim	3	39.1	41.0	19.0	0.29	0.28	0.11	99.7	1.004	1.568	0.407	0.008	0.006	0.002	2.996	79.4
	13*	core	3	39.4	42.7	16.6	0.30	0.23	0.12	99.3	1.005	1.621	0.354	0.008	0.005	0.002	2.995	82.1
		rim	3	38.9	40.5	19.1	0.30	0.30	0.11	99.3	1.005	1.560	0.413	0.008	0.006	0.002	2.995	79.1
	15*	core	3	39.1	40.9	18.7	0.29	0.29	0.11	99.4	1.006	1.569	0.403	0.008	0.006	0.002	2.994	79.5
		rim	5	38.6	39.6	19.9	0.29	0.30	0.09	98.9	1.005	1.538	0.434	0.008	0.007	0.002	2.995	78.0
	16**	core	3	39.0	41.1	18.3	0.28	0.27	0.09	99.0	1.006	1.580	0.394	0.008	0.006	0.002	2.994	80.0
		rim	3	38.8	40.6	18.8	0.30	0.25	0.10	98.9	1.005	1.567	0.407	0.008	0.005	0.002	2.995	79.4
	19a	core	3	38.7	39.8	19.9	0.26	0.30	0.15	99.2	1.004	1.542	0.433	0.007	0.007	0.003	2.996	78.1
		rim	3	38.9	40.8	18.9	0.30	0.31	0.12	99.3	1.004	1.568	0.407	0.008	0.007	0.002	2.996	79.4
	19b	core	4	38.7	39.7	20.1	0.25	0.28	0.16	99.3	1.005	1.537	0.437	0.007	0.006	0.003	2.995	77.9
		rim	3	38.9	40.4	19.5	0.28	0.28	0.13	99.5	1.004	1.556	0.421	0.008	0.006	0.003	2.996	78.7
39-1	7	core	3	39.1	43.1	17.5	0.30	0.27	0.11	100.4	0.992	1.629	0.371	0.008	0.006	0.002	3.008	81.5
		rim	3	39.4	44.0	16.3	0.33	0.22	0.15	100.4	0.993	1.654	0.344	0.009	0.005	0.003	3.007	82.8
	9	core	3	39.4	44.1	15.9	0.33	0.26	0.11	100.1	0.994	1.659	0.336	0.009	0.006	0.002	3.006	83.2
		rim	2	39.2	43.7	16.3	0.34	0.25	0.12	99.9	0.994	1.649	0.345	0.009	0.005	0.002	3.006	82.7
	16	core	2	39.1	44.1	15.9	0.31	0.23	0.15	99.7	0.991	1.665	0.336	0.008	0.005	0.003	3.009	83.2
		rim	2	38.9	42.8	17.3	0.33	0.26	0.10	99.7	0.993	1.627	0.370	0.009	0.006	0.002	3.007	81.5
	17	core	3	39.1	44.4	14.7	0.33	0.22	0.14	98.9	0.995	1.681	0.313	0.009	0.005	0.003	3.005	84.3
		rim	3	39.0	43.8	15.5	0.33	0.24	0.14	98.9	0.994	1.665	0.330	0.009	0.005	0.003	3.006	83.5
	18	core	3	39.2	44.1	15.4	0.30	0.25	0.13	99.3	0.995	1.669	0.326	0.008	0.005	0.003	3.005	83.6
		rim	3	39.1	43.6	16.0	0.30	0.26	0.13	99.3	0.995	1.653	0.341	0.008	0.006	0.003	3.005	82.9
	19	core	3	39.2	43.9	15.8	0.31	0.21	0.13	99.7	0.994	1.660	0.336	0.008	0.005	0.003	3.006	83.2
		rim	3	39.1	43.7	15.9	0.31	0.21	0.14	99.5	0.995	1.656	0.339	0.009	0.005	0.003	3.005	83.0
	20	core	3	39.2	44.1	15.3	0.31	0.22	0.15	99.2	0.995	1.668	0.325	0.008	0.005	0.003	3.005	83.7
		rim	3	39.0	43.5	15.6	0.33	0.19	0.14	98.8	0.997	1.657	0.333	0.009	0.004	0.003	3.003	83.3

Appendix C (Continued). Olivine Data

				Oxides (wt%)							Cations based on 4 oxygens							
sample	grain		n	SiO_2	MgO	FeO*	CaO	MnO	NiO	Total	Si	Mg	Fe	Ca	Mn	Ni	Sum	Fo
40-2	7	core	3	39.7	45.7	13.9	0.32	0.20	0.17	100.0	0.993	1.706	0.291	0.009	0.004	0.004	3.007	85.4
		rim	3	40.0	46.4	13.0	0.33	0.17	0.17	100.0	0.995	1.723	0.270	0.009	0.004	0.004	3.005	86.4
	8	core	3	40.1	47.7	11.4	0.32	0.15	0.23	99.9	0.994	1.760	0.237	0.008	0.003	0.005	3.006	88.1
		rim	3	39.9	46.9	12.3	0.32	0.19	0.25	99.9	0.993	1.740	0.256	0.009	0.004	0.005	3.007	87.2
	9	core	3	39.8	46.2	13.2	0.31	0.21	0.17	99.9	0.994	1.719	0.276	0.008	0.004	0.003	3.006	86.2
		rim	3	39.7	46.4	13.0	0.33	0.23	0.23	99.8	0.992	1.726	0.271	0.009	0.005	0.005	3.008	86.4
	10	core	3	39.8	46.4	13.1	0.30	0.19	0.21	100.0	0.993	1.724	0.273	0.008	0.004	0.004	3.007	86.3
		rim	3	39.9	46.5	13.0	0.33	0.22	0.20	100.1	0.993	1.725	0.270	0.009	0.005	0.004	3.007	86.5
	11	core	3	39.8	46.8	12.8	0.32	0.19	0.18	100.1	0.991	1.736	0.265	0.009	0.004	0.004	3.009	86.7
		rim	3	39.2	46.5	13.0	0.33	0.18	0.15	99.4	0.985	1.740	0.273	0.009	0.004	0.003	3.015	86.4
	12*	core	3	40.0	46.5	12.8	0.32	0.17	0.21	100.0	0.995	1.726	0.267	0.009	0.004	0.004	3.005	86.6
		rim	3	39.8	46.2	12.9	0.33	0.25	0.17	99.7	0.995	1.723	0.270	0.009	0.005	0.003	3.005	86.5
	13*	core	3	40.0	46.4	13.2	0.30	0.20	0.20	100.3	0.994	1.721	0.274	0.008	0.004	0.004	3.006	86.3
		rim	3	39.9	46.7	13.0	0.34	0.21	0.22	100.4	0.992	1.728	0.271	0.009	0.004	0.004	3.009	86.4
42-4	1	core	3	40.4	49.1	9.8	0.32	0.15	0.28	100.0	0.993	1.797	0.201	0.008	0.003	0.005	3.007	90.0
		rim	3	40.1	47.6	11.8	0.33	0.20	0.20	100.2	0.992	1.754	0.244	0.009	0.004	0.004	3.008	87.8
	2a	core	3	40.4	48.9	10.1	0.32	0.19	0.26	100.1	0.992	1.791	0.207	0.008	0.004	0.005	3.008	89.6
		rim	3	40.0	46.8	12.2	0.32	0.17	0.18	99.8	0.996	1.737	0.254	0.009	0.004	0.004	3.004	87.2
	2b	core	3	40.5	48.7	10.2	0.31	0.14	0.26	100.2	0.994	1.785	0.210	0.008	0.003	0.005	3.006	89.5
		rim	3	40.1	47.1	12.2	0.33	0.18	0.18	100.1	0.994	1.741	0.253	0.009	0.004	0.004	3.006	87.3
	4	core	2	39.7	46.1	13.4	0.31	0.17	0.16	99.9	0.992	1.719	0.281	0.008	0.004	0.003	3.008	86.0
		rim	2	39.8	46.3	13.0	0.33	0.17	0.15	99.8	0.994	1.724	0.272	0.009	0.004	0.003	3.006	86.4
	9	core	2	39.8	46.5	13.0	0.33	0.21	0.16	99.9	0.993	1.728	0.271	0.009	0.005	0.003	3.007	86.5
		rim	2	39.9	46.4	13.0	0.33	0.23	0.15	100.0	0.995	1.722	0.270	0.009	0.005	0.003	3.005	86.4
	10	core	2	39.8	46.6	12.9	0.33	0.19	0.17	99.9	0.992	1.731	0.269	0.009	0.004	0.004	3.008	86.5
		rim	2	39.7	46.4	12.9	0.34	0.21	0.17	99.7	0.993	1.729	0.269	0.009	0.004	0.003	3.007	86.5
43-1	12	core	3	40.0	45.8	12.5	0.32	0.20	0.15	98.9	1.004	1.714	0.262	0.009	0.004	0.003	2.996	86.7
		rim	2	40.1	45.8	12.4	0.36	0.22	0.13	99.1	1.005	1.712	0.261	0.010	0.005	0.003	2.995	86.8
	13*	core	3	39.9	46.0	12.5	0.31	0.22	0.16	99.1	1.002	1.718	0.263	0.008	0.005	0.003	2.998	86.7
		rim	2	40.0	45.7	12.7	0.34	0.22	0.13	99.1	1.004	1.710	0.266	0.009	0.005	0.003	2.996	86.6
	14	core	2	39.9	45.8	12.6	0.32	0.19	0.13	98.9	1.003	1.715	0.264	0.009	0.004	0.003	2.997	86.6
		rim	3	40.1	45.8	12.8	0.35	0.19	0.12	99.2	1.004	1.709	0.268	0.009	0.004	0.002	2.996	86.5
	15	core	4	40.0	45.9	12.6	0.35	0.21	0.16	99.2	1.002	1.715	0.263	0.009	0.004	0.003	2.998	86.7
		rim	4	39.9	45.7	12.8	0.36	0.20	0.13	99.1	1.001	1.713	0.268	0.010	0.004	0.003	2.999	86.5
44-1	4*	core	3	39.8	46.0	13.2	0.40	0.19	0.23	99.7	0.995	1.715	0.276	0.011	0.004	0.005	3.005	86.1
	5*	core	4	39.5	45.9	13.5	0.32	0.20	0.24	99.7	0.991	1.717	0.284	0.009	0.004	0.005	3.009	85.8
	7*	core	4	39.6	45.8	13.6	0.35	0.20	0.20	99.8	0.992	1.713	0.286	0.009	0.004	0.004	3.008	85.7
	8	core	3	39.8	45.9	13.0	0.40	0.21	0.23	99.6	0.997	1.714	0.273	0.011	0.004	0.005	3.003	86.3
	9*	core	5	39.6	45.8	13.6	0.32	0.19	0.21	99.7	0.994	1.711	0.284	0.009	0.004	0.004	3.006	85.7
	10	core	2	39.7	45.3	13.4	0.43	0.21	0.20	99.3	0.999	1.700	0.281	0.012	0.004	0.004	3.001	85.8
48-1	2*	core	2	39.4	44.6	15.0	0.35	0.22	0.16	99.8	0.994	1.677	0.316	0.010	0.005	0.003	3.006	84.1
	3	core	3	39.5	45.0	15.2	0.32	0.22	0.16	100.3	0.991	1.683	0.319	0.009	0.005	0.003	3.009	84.1
		rim	3	39.5	44.7	14.9	0.38	0.19	0.15	99.8	0.996	1.678	0.313	0.010	0.004	0.003	3.004	84.3
	6	core	4	39.6	45.5	14.5	0.33	0.24	0.16	100.3	0.991	1.697	0.304	0.009	0.005	0.003	3.009	84.8
	7	core	3	39.6	44.6	15.3	0.30	0.26	0.14	100.1	0.995	1.671	0.322	0.008	0.006	0.003	3.005	83.9
		rim	3	39.6	44.8	15.2	0.33	0.21	0.14	100.3	0.994	1.677	0.319	0.009	0.004	0.003	3.006	84.0
	8	core	3	39.2	44.2	15.8	0.32	0.23	0.13	100.0	0.992	1.665	0.334	0.009	0.005	0.003	3.008	83.3
		rim	3	39.5	44.6	15.2	0.34	0.23	0.14	100.0	0.995	1.674	0.320	0.009	0.005	0.003	3.005	84.0
	11	core	3	39.5	45.3	14.4	0.32	0.23	0.17	100.0	0.992	1.696	0.303	0.009	0.005	0.003	3.008	84.9
	13*	core	3	39.4	44.7	14.7	0.35	0.23	0.17	99.6	0.995	1.682	0.311	0.010	0.005	0.004	3.005	84.4
49-1	4*	core	3	38.5	40.5	20.5	0.26	0.32	0.09	100.1	0.993	1.555	0.443	0.007	0.007	0.002	3.007	77.8
		rim	3	38.4	39.8	21.0	0.28	0.33	0.09	100.0	0.995	1.538	0.455	0.008	0.007	0.002	3.005	77.2
	15	core	3	38.3	39.9	21.2	0.29	0.32	0.09	100.1	0.992	1.541	0.458	0.008	0.007	0.002	3.008	77.1
		rim	3	38.4	39.6	21.3	0.29	0.30	0.07	99.9	0.996	1.531	0.462	0.008	0.007	0.002	3.005	76.8
	17	core	4	38.5	39.8	21.3	0.29	0.35	0.07	100.3	0.995	1.533	0.461	0.008	0.008	0.002	3.005	76.9
1 standard deviation (σ)				0.13	0.13	0.01	0.02	0.11	0.02	0.21	0.0037	0.0019	0.0002	0.0005	0.0022	0.0003	0.0019	0.11

All analyses by University of Hawaii electron microprobe. Total Fe assumed to be Fe^{3+}. Fo (forsterite) content is cationic ratio 100 Mg/(Mg+Fe). n = number fo probe analyses used in the average. Note: * denotes skeletal grains, ** denotes plagioclase and olivine and clinopyroxene intergrowths.

Appendix D. Plagioclase Data

				Oxides (wt%)								Cations (wt%) based on 8 oxygens								
sample	grain		n	NaO	MgO	Al_2O_3	SiO_2	K_2O	CaO	FeO	Total	Na	Mg	Al	Si	K	Ca	Fe	Total	An
29-1	1	core	7	2.97	0.20	31.6	49.8	0.03	14.7	0.52	99.7	0.264	0.014	1.703	2.280	0.002	0.719	0.020	5.001	73.0
		rim	7	2.75	0.19	32.0	49.1	0.03	15.1	0.60	99.7	0.245	0.013	1.731	2.252	0.002	0.740	0.023	5.005	75.1
	12	core	7	2.65	0.19	31.9	48.8	0.02	15.1	0.57	99.3	0.237	0.013	1.733	2.249	0.001	0.748	0.022	5.003	75.8
	13	core	5	2.72	0.18	32.0	49.1	0.03	14.8	0.60	99.5	0.242	0.012	1.731	2.257	0.002	0.731	0.023	4.999	74.9
31-1	3*	core	4	3.42	0.18	30.5	50.7	0.03	13.7	0.51	99.0	0.305	0.012	1.653	2.330	0.002	0.675	0.020	4.996	68.7
		rim	3	3.19	0.16	30.9	49.9	0.03	14.3	0.59	99.1	0.285	0.011	1.680	2.300	0.002	0.704	0.023	5.003	71.1
	4	core	4	2.95	0.17	31.2	49.4	0.02	14.7	0.46	98.9	0.264	0.012	1.698	2.283	0.001	0.725	0.018	5.001	73.2
		rim	4	3.19	0.19	30.9	50.4	0.04	14.2	0.51	99.3	0.284	0.013	1.669	2.312	0.002	0.697	0.019	4.997	70.9
	8*	core	4	3.58	0.19	30.2	51.2	0.04	13.6	0.55	99.4	0.318	0.013	1.632	2.346	0.002	0.666	0.021	4.998	67.5
		rim	3	3.80	0.19	29.6	51.8	0.04	13.1	0.63	99.2	0.338	0.013	1.602	2.373	0.003	0.644	0.024	4.996	65.4
	17^	core	3	3.97	0.23	29.4	52.2	0.05	12.8	0.70	99.4	0.352	0.015	1.583	2.388	0.003	0.629	0.027	4.998	63.9
	11^	core	4	3.73	0.18	30.0	51.3	0.04	13.3	0.62	99.1	0.332	0.012	1.621	2.356	0.003	0.653	0.024	5.001	66.1
		rim	3	3.83	0.17	29.9	51.8	0.05	13.1	0.63	99.5	0.340	0.012	1.608	2.368	0.003	0.644	0.024	4.999	65.3
	13	core	4	3.89	0.20	29.6	51.7	0.05	13.0	0.61	99.1	0.346	0.014	1.600	2.374	0.003	0.640	0.024	5.000	64.7
		rim	3	3.81	0.19	29.7	51.7	0.05	13.1	0.61	99.2	0.339	0.013	1.605	2.370	0.003	0.645	0.023	4.998	65.4
	14^	core	3	4.15	0.18	29.3	52.4	0.06	12.5	0.66	99.3	0.368	0.012	1.578	2.398	0.003	0.613	0.025	4.998	62.3
	15^	core	3	3.86	0.20	29.7	51.9	0.05	13.0	0.66	99.4	0.343	0.013	1.603	2.374	0.003	0.638	0.025	4.998	64.9
	18^	core	4	3.93	0.19	29.7	52.1	0.05	13.0	0.65	99.6	0.348	0.013	1.598	2.378	0.003	0.635	0.025	4.999	64.4
34-4	1*	core	4	3.41	0.20	30.7	51.0	0.04	14.0	0.57	100.0	0.302	0.014	1.650	2.326	0.002	0.685	0.022	5.000	69.3
		rim	4	3.24	0.21	31.0	50.5	0.04	14.2	0.56	99.8	0.287	0.014	1.672	2.308	0.002	0.697	0.021	5.001	70.6
	2a*	core	4	3.23	0.20	31.0	50.2	0.03	14.3	0.55	99.5	0.287	0.014	1.673	2.303	0.002	0.704	0.021	5.004	70.9
		rim	4	2.96	0.22	31.6	50.3	0.03	14.8	0.55	100.5	0.261	0.015	1.695	2.285	0.002	0.721	0.021	4.999	73.3
	3**	core	6	1.42	0.24	34.2	46.5	0.01	17.5	0.33	100.3	0.13	0.016	1.849	2.136	0.001	0.863	0.013	5.003	87.2
		rim	2	2.75	0.22	32.0	49.5	0.02	15.2	0.54	100.3	0.24	0.015	1.720	2.259	0.001	0.744	0.021	5.003	75.3
	6	core	4	3.17	0.20	31.4	50.4	0.03	14.5	0.53	100.2	0.280	0.013	1.683	2.297	0.002	0.707	0.020	5.002	71.5
		rim	4	3.09	0.23	31.2	50.0	0.04	14.6	0.53	99.7	0.275	0.016	1.685	2.290	0.002	0.717	0.020	5.006	72.2
	7	core	4	2.27	0.17	32.8	47.9	0.02	16.1	0.48	99.8	0.202	0.012	1.779	2.204	0.001	0.793	0.019	5.008	79.6
		rim	4	2.34	0.18	32.7	48.4	0.03	15.9	0.47	100.0	0.207	0.012	1.767	2.216	0.001	0.783	0.018	5.005	78.9
	8	core	4	2.95	0.19	31.5	49.5	0.04	14.8	0.57	99.6	0.263	0.013	1.705	2.272	0.002	0.731	0.022	5.008	73.4
		rim	4	3.01	0.21	31.4	49.7	0.03	14.8	0.55	99.8	0.267	0.014	1.697	2.279	0.002	0.726	0.021	5.007	73.0
	9	core	4	3.21	0.19	31.1	50.9	0.04	14.3	0.53	100.2	0.283	0.013	1.667	2.313	0.002	0.697	0.020	4.996	71.0
		rim	4	3.02	0.22	31.3	50.0	0.03	14.7	0.52	99.8	0.268	0.015	1.687	2.290	0.002	0.720	0.020	5.001	72.7
	10*	core	4	2.94	0.18	31.6	49.8	0.04	14.9	0.51	100.0	0.261	0.013	1.704	2.277	0.002	0.727	0.019	5.003	73.5
		rim	4	2.80	0.21	31.8	49.8	0.04	15.0	0.52	100.1	0.248	0.014	1.710	2.272	0.002	0.732	0.020	4.998	74.6
36-1	2	core	3	3.35	0.23	30.6	50.9	0.03	13.9	0.57	99.5	0.298	0.016	1.650	2.329	0.001	0.680	0.022	4.995	69.5
		rim	4	3.31	0.22	30.5	50.3	0.03	14.0	0.59	99.0	0.296	0.015	1.657	2.319	0.002	0.689	0.023	5.001	69.8
	5^	core	3	3.68	0.24	30.0	51.2	0.04	13.3	0.62	99.1	0.328	0.017	1.622	2.352	0.002	0.657	0.024	5.002	66.6
	6^	core	3	3.56	0.24	30.2	51.1	0.04	13.5	0.68	99.4	0.317	0.016	1.634	2.341	0.003	0.665	0.026	5.002	67.6
	10	core	4	3.60	0.26	29.9	51.6	0.03	13.5	0.67	99.6	0.319	0.018	1.613	2.358	0.002	0.661	0.026	4.996	67.3
	11	core	3	3.61	0.24	30.0	51.2	0.04	13.5	0.67	99.2	0.321	0.017	1.621	2.351	0.003	0.662	0.026	5.000	67.2
	13^^	core	3	3.66	0.25	30.0	51.0	0.04	13.5	0.61	99.1	0.326	0.017	1.627	2.345	0.002	0.664	0.023	5.005	66.9
	14	core	3	3.78	0.23	30.0	51.5	0.04	13.3	0.65	99.5	0.335	0.016	1.618	2.357	0.002	0.649	0.025	5.003	65.8
38-2	1*	core	3	3.55	0.13	30.3	50.9	0.05	13.6	0.61	99.1	0.316	0.009	1.639	2.339	0.003	0.671	0.023	5.001	67.8
		rim	3	3.49	0.16	30.3	51.0	0.04	13.8	0.63	99.4	0.311	0.011	1.640	2.337	0.003	0.676	0.024	5.000	68.3
	2*	core	4	1.43	0.22	33.7	46.2	0.01	17.2	0.34	99.1	0.129	0.015	1.843	2.143	0.000	0.857	0.013	5.000	86.9
		rim	3	2.73	0.22	31.6	49.4	0.01	15.0	0.52	99.5	0.243	0.015	1.710	2.270	0.001	0.739	0.020	4.997	75.2
	3	core	4	3.70	0.14	30.3	51.5	0.04	13.4	0.63	99.6	0.328	0.009	1.630	2.351	0.002	0.656	0.024	5.000	66.5
		rim	3	3.55	0.17	30.3	51.1	0.04	13.7	0.61	99.5	0.315	0.011	1.638	2.340	0.002	0.670	0.024	5.000	67.8
	4*	core	3	2.91	0.15	31.4	49.4	0.03	14.7	0.56	99.3	0.259	0.010	1.705	2.276	0.002	0.728	0.022	5.002	73.6
		rim	3	3.52	0.18	30.3	51.3	0.03	13.6	0.60	99.5	0.313	0.012	1.632	2.346	0.002	0.668	0.023	4.996	68.0
	6	core	4	3.28	0.19	30.7	50.6	0.03	14.1	0.54	99.5	0.291	0.013	1.658	2.320	0.002	0.693	0.021	4.998	70.3
		rim	3	3.30	0.20	30.6	51.0	0.04	14.0	0.57	99.7	0.292	0.014	1.646	2.332	0.002	0.685	0.022	4.993	70.0
	7^^	core	3	3.12	0.20	31.0	49.9	0.02	14.4	0.52	99.2	0.278	0.014	1.680	2.298	0.001	0.711	0.020	5.002	71.8
	10	core	4	3.79	0.14	30.1	51.4	0.04	13.3	0.59	99.3	0.336	0.010	1.623	2.354	0.002	0.655	0.023	5.003	65.9
		rim	3	3.68	0.20	30.0	51.7	0.05	13.3	0.61	99.6	0.326	0.014	1.615	2.362	0.003	0.652	0.023	4.995	66.5
	14*	core	4	3.26	0.21	30.8	50.4	0.03	14.1	0.53	99.4	0.290	0.015	1.666	2.312	0.001	0.695	0.020	5.000	70.5
		rim	3	3.34	0.22	30.5	50.7	0.03	14.0	0.63	99.4	0.297	0.015	1.650	2.325	0.002	0.687	0.024	4.999	69.7
	16^^	core	3	3.10	0.26	30.7	49.9	0.02	14.4	0.60	98.9	0.277	0.018	1.670	2.302	0.001	0.710	0.023	5.002	71.8
	17^^	core	4	3.45	0.24	30.4	50.7	0.03	13.9	0.58	99.2	0.307	0.016	1.644	2.329	0.002	0.682	0.022	5.003	68.8
39-1	2*	core	3	2.95	0.18	31.3	49.4	0.02	14.4	0.51	98.8	0.265	0.012	1.702	2.284	0.001	0.714	0.020	4.998	72.9
		rim	3	2.43	0.18	32.0	48.2	0.02	15.3	0.54	98.6	0.219	0.013	1.749	2.236	0.001	0.760	0.021	4.999	77.5
	8*	core	4	2.69	0.23	32.2	49.7	0.02	15.5	0.47	100.8	0.236	0.015	1.721	2.257	0.001	0.752	0.018	5.001	76.0
		rim	4	2.17	0.19	33.1	48.1	0.02	16.3	0.52	100.4	0.192	0.013	1.782	2.200	0.001	0.799	0.020	5.006	80.5
	11*	core	5	2.56	0.20	31.9	48.5	0.03	15.0	0.50	98.7	0.230	0.013	1.741	2.247	0.002	0.746	0.019	4.998	76.4
		rim	4	2.82	0.22	31.3	49.3	0.02	14.6	0.54	98.7	0.253	0.015	1.704	2.279	0.001	0.723	0.021	4.996	74.0
	12	core	2	1.95	0.20	33.2	47.5	0.02	16.5	0.38	99.7	0.174	0.013	1.799	2.187	0.001	0.813	0.015	5.002	82.3
		rim	5	2.94	0.25	31.5	49.8	0.03	14.7	0.50	99.8	0.261	0.017	1.699	2.280	0.002	0.723	0.019	5.001	73.3
	12b	core	3	2.05	0.19	33.2	47.9	0.02	16.3	0.38	100.0	0.183	0.013	1.793	2.195	0.001	0.802	0.015	5.001	81.3
		rim	4	1.96	0.18	33.2	47.5	0.02	16.4	0.45	99.8	0.175	0.012	1.802	2.185	0.001	0.810	0.017	5.003	82.1
	14&&	core	5	2.11	0.19	33.1	47.9	0.02	16.3	0.38	100.0	0.188	0.013	1.790	2.197	0.001	0.801	0.014	5.003	80.9
		rim	5	1.72	0.16	33.9	46.9	0.01	17.0	0.43	100.1	0.153	0.011	1.834	2.155	0.001	0.835	0.017	5.005	84.5
	15^	core	3	3.43	0.29	30.4	51.2	0.04	13.9	0.60	99.8	0.304	0.020	1.633	2.338	0.002	0.679	0.023	4.999	68.9
		rim	3	3.15	0.24	31.1	50.5	0.04	14.5	0.56	100.0	0.279	0.016	1.673	2.303	0.002	0.707	0.021	5.001	71.5
	15b^	core	3	3.10	0.24	31.1	50.7	0.03	14.4	0.56	100.1	0.274	0.016	1.671	2.309	0.002	0.701	0.021	4.994	71.8

Appendix D (Continued). Plagioclase Data

				Oxides (wt%)								Cations (wt%) based on 8 oxygens								
sample	grain		n	NaO	MgO	Al_2O_3	SiO_2	K_2O	CaO	FeO	Total	Na	Mg	Al	Si	K	Ca	Fe	Total	An
40-2	1*	core	6	1.65	0.21	33.7	46.6	0.02	16.9	0.34	99.3	0.148	0.014	1.836	2.154	0.001	0.836	0.013	5.003	84.9
		rim	6	2.19	0.27	32.7	47.9	0.01	15.9	0.41	99.4	0.196	0.018	1.777	2.207	0.000	0.787	0.016	5.002	80.1
	2*	core	6	1.2	0.2	34.4	45.3	0.00	17.64	0.31	99.1	0.111	0.011	1.886	2.107	0.000	0.879	0.012	5.006	88.8
		rim	5	2.1	0.3	32.8	47.5	0.01	16.16	0.40	99.2	0.187	0.018	1.786	2.197	0.001	0.800	0.016	5.004	81.0
	3*	core	4	1.97	0.23	32.9	47.1	0.01	16.6	0.34	99.1	0.177	0.016	1.795	2.184	0.001	0.822	0.013	5.008	82.2
		rim	5	2.42	0.27	32.3	48.6	0.01	15.6	0.40	99.6	0.216	0.019	1.751	2.231	0.001	0.769	0.015	5.002	78.0
	4&	core	5	1.74	0.20	33.6	46.8	0.01	16.7	0.43	99.5	0.156	0.014	1.826	2.163	0.000	0.825	0.017	5.002	84.1
		rim	6	2.39	0.27	32.2	48.2	0.01	15.7	0.42	99.2	0.214	0.018	1.752	2.226	0.001	0.778	0.016	5.006	78.3
	5&	core	5	2.67	0.19	32.1	49.2	0.02	15.0	0.49	99.7	0.238	0.013	1.733	2.256	0.001	0.737	0.019	4.997	75.5
		rim	6	2.09	0.25	32.8	47.5	0.01	16.1	0.42	99.1	0.187	0.017	1.786	2.197	0.000	0.800	0.016	5.004	81.0
	18*	core	3	1.43	0.18	34.4	46.2	0.02	17.2	0.31	99.7	0.128	0.012	1.869	2.130	0.001	0.848	0.012	5.000	86.8
		rim	8	1.86	0.23	33.4	47.0	0.01	16.6	0.39	99.6	0.167	0.016	1.817	2.169	0.001	0.822	0.015	5.006	83.1
	21*	core	5	1.50	0.23	34.0	46.6	0.01	17.1	0.36	99.7	0.134	0.016	1.847	2.145	0.000	0.843	0.014	4.999	86.3
		rim	4	2.19	0.26	32.7	47.8	0.01	16.0	0.40	99.3	0.196	0.018	1.779	2.206	0.000	0.789	0.016	5.003	80.1
42-4	6* **	core	8	1.30	0.38	33.9	46.2	0.00	17.8	0.41	99.9	0.116	0.026	1.841	2.131	0.000	0.878	0.016	5.007	88.3
		rim	4	1.11	0.22	34.4	45.8	0.00	18.0	0.38	99.9	0.100	0.015	1.871	2.112	0.000	0.891	0.014	5.003	89.9
	7*	core	4	1.11	0.26	34.4	45.7	0.00	18.0	0.34	99.9	0.099	0.018	1.871	2.111	0.000	0.891	0.013	5.003	90.0
		rim	3	1.08	0.21	34.5	45.9	0.00	18.0	0.38	100.1	0.097	0.014	1.873	2.112	0.000	0.889	0.015	5.000	90.2
	8*	core	4	1.01	0.25	34.6	45.1	0.00	18.3	0.28	99.6	0.090	0.017	1.891	2.090	0.000	0.909	0.011	5.009	90.9
		rim	3	0.91	0.18	35.1	45.2	0.00	18.4	0.32	100.1	0.082	0.012	1.906	2.083	0.000	0.909	0.012	5.005	91.8
	11&	core	4	2.89	0.22	31.5	49.2	0.02	15.1	0.48	99.4	0.258	0.015	1.711	2.264	0.001	0.743	0.019	5.010	74.2
	12	core	4	1.40	0.30	33.8	46.2	0.00	17.6	0.33	99.5	0.125	0.021	1.842	2.135	0.000	0.871	0.013	5.007	87.4
		rim	4	1.05	0.23	34.7	45.3	0.00	18.2	0.37	99.8	0.094	0.016	1.890	2.094	0.000	0.900	0.014	5.008	90.6
	13	core	4	1.14	0.23	34.3	45.4	0.00	18.0	0.38	99.4	0.103	0.016	1.876	2.105	0.000	0.895	0.015	5.009	89.7
		rim	4	1.09	0.22	34.3	45.3	0.00	18.1	0.39	99.5	0.098	0.015	1.878	2.102	0.000	0.900	0.015	5.008	90.2
	14	core	4	1.32	0.27	33.9	45.8	0.01	17.7	0.34	99.4	0.118	0.019	1.853	2.125	0.000	0.881	0.013	5.008	88.1
		rim	4	1.19	0.26	34.2	45.4	0.00	18.0	0.39	99.3	0.107	0.018	1.870	2.107	0.000	0.894	0.015	5.012	89.3
	16^	core	3	2.98	0.33	30.8	50.3	0.02	14.6	0.59	99.7	0.265	0.023	1.663	2.304	0.001	0.718	0.023	4.997	73.0
43-1	1*	core	4	1.52	0.23	33.7	46.8	0.00	17.2	0.29	99.7	0.136	0.016	1.830	2.156	0.000	0.848	0.011	4.997	86.2
		rim	4	2.17	0.27	32.4	48.4	0.01	16.0	0.42	99.6	0.194	0.019	1.754	2.225	0.001	0.787	0.016	4.995	80.2
	3^	core	4	2.61	0.31	31.5	49.3	0.00	15.3	0.40	99.4	0.233	0.021	1.707	2.267	0.000	0.752	0.015	4.996	76.4
		rim	3	2.36	0.31	31.9	48.8	0.01	15.7	0.44	99.4	0.210	0.021	1.732	2.244	0.001	0.772	0.017	4.996	78.6
	4&	core	4	2.46	0.31	31.6	48.6	0.00	15.5	0.44	99.0	0.221	0.021	1.723	2.248	0.000	0.770	0.017	5.001	77.7
	6*	core	4	1.42	0.23	33.7	46.2	0.00	17.2	0.32	99.1	0.128	0.016	1.845	2.142	0.000	0.857	0.013	5.000	87.0
		rim	3	2.57	0.33	31.3	49.5	0.01	15.2	0.50	99.5	0.229	0.023	1.698	2.273	0.001	0.750	0.019	4.993	76.5
	13^^	core	5	2.62	0.31	31.4	48.9	0.01	15.3	0.48	99.0	0.235	0.021	1.713	2.258	0.001	0.756	0.019	5.003	76.2
	17^^	core	4	2.67	0.35	31.3	49.3	0.01	15.2	0.43	99.3	0.239	0.024	1.700	2.270	0.001	0.749	0.016	4.999	75.8
		rim	3	2.51	0.31	31.7	48.9	0.01	15.4	0.46	99.3	0.224	0.021	1.719	2.254	0.000	0.762	0.018	4.999	77.2
44-1	1**	core	4	1.81	0.24	33.5	47.0	0.01	16.6	0.38	99.6	0.162	0.016	1.823	2.166	0.000	0.823	0.015	5.004	83.5
		rim	4	1.69	0.23	33.7	46.6	0.00	16.9	0.42	99.5	0.151	0.016	1.834	2.152	0.000	0.838	0.016	5.007	84.7
48-1	1*	core	4	2.34	0.23	32.7	48.4	0.00	16.1	0.44	100.2	0.208	0.016	1.764	2.214	0.000	0.789	0.017	5.008	79.1
		rim	3	2.10	0.22	33.2	48.1	0.01	16.5	0.43	100.5	0.185	0.015	1.787	2.195	0.001	0.805	0.017	5.005	81.2
	4	core	4	2.13	0.22	33.0	48.0	0.01	16.3	0.44	100.2	0.189	0.015	1.783	2.199	0.001	0.801	0.017	5.004	80.9
		rim	4	1.98	0.22	33.3	47.7	0.00	16.7	0.44	100.3	0.176	0.015	1.798	2.182	0.000	0.818	0.017	5.006	82.3
	5	core	4	1.92	0.20	33.3	47.8	0.00	16.6	0.44	100.2	0.171	0.014	1.798	2.187	0.000	0.813	0.017	4.999	82.6
		rim	4	2.11	0.22	33.1	47.9	0.01	16.4	0.49	100.2	0.188	0.015	1.788	2.193	0.001	0.804	0.019	5.007	81.0
	9	core	9	1.44	0.24	34.4	47.0	0.00	17.6	0.31	100.9	0.127	0.016	1.847	2.140	0.000	0.858	0.012	5.000	87.1
		rim	9	2.14	0.21	33.2	48.3	0.01	16.4	0.45	100.6	0.189	0.014	1.782	2.201	0.000	0.799	0.017	5.003	80.8
	10	core	3	1.88	0.19	33.3	47.4	0.00	16.7	0.47	99.9	0.168	0.013	1.804	2.178	0.000	0.821	0.018	5.004	83.0
		rim	3	2.00	0.21	33.3	48.0	0.01	16.6	0.50	100.6	0.177	0.014	1.792	2.189	0.000	0.812	0.019	5.004	82.1
	12*	core	3	1.48	0.22	34.3	46.5	0.00	17.6	0.35	100.4	0.132	0.015	1.853	2.132	0.000	0.863	0.013	5.008	86.7
		rim	2	2.61	0.26	32.3	49.5	0.02	15.6	0.53	100.8	0.230	0.017	1.730	2.247	0.001	0.758	0.020	5.003	76.7
	14*	core	4	1.48	0.18	34.4	46.4	0.01	17.6	0.41	100.5	0.132	0.013	1.856	2.128	0.000	0.866	0.016	5.010	86.8
		rim	3	2.09	0.21	33.2	48.3	0.01	16.4	0.48	100.7	0.185	0.014	1.783	2.200	0.001	0.801	0.018	5.001	81.2
49-1	1	core	5	3.09	0.19	31.3	50.1	0.02	14.7	0.56	99.9	0.273	0.013	1.688	2.289	0.001	0.718	0.022	5.004	72.3
		rim	3	2.81	0.19	32.0	49.5	0.02	15.1	0.60	100.2	0.248	0.013	1.719	2.261	0.001	0.740	0.023	5.004	74.8
	2* ^	core	4	3.24	0.20	31.2	50.5	0.03	14.4	0.55	100.1	0.286	0.014	1.676	2.301	0.002	0.704	0.021	5.005	71.0
		rim	3	3.79	0.22	30.1	52.2	0.04	13.4	0.64	100.4	0.333	0.015	1.609	2.365	0.002	0.649	0.024	4.998	65.9
	3*	core	4	3.16	0.19	31.2	50.1	0.03	14.5	0.57	99.8	0.280	0.013	1.683	2.294	0.002	0.711	0.022	5.005	71.6
		rim	3	2.77	0.18	31.8	49.7	0.02	15.0	0.63	100.1	0.246	0.012	1.710	2.271	0.001	0.735	0.024	4.998	74.9
	7	core	5	3.06	0.18	31.4	50.0	0.02	14.7	0.57	99.9	0.271	0.012	1.692	2.286	0.001	0.720	0.022	5.005	72.5
		rim	3	3.18	0.18	31.2	50.5	0.03	14.4	0.65	100.2	0.281	0.013	1.676	2.301	0.002	0.705	0.025	5.002	71.4
	10*	core	4	3.20	0.19	31.1	50.6	0.03	14.4	0.58	100.2	0.283	0.013	1.672	2.305	0.002	0.704	0.022	5.001	71.2
		rim	4	3.87	0.23	29.9	52.1	0.04	13.3	0.68	100.1	0.341	0.015	1.602	2.368	0.002	0.649	0.026	5.003	65.4
	11	core	4	3.05	0.18	31.7	50.3	0.02	14.8	0.56	100.7	0.269	0.012	1.694	2.285	0.001	0.721	0.021	5.003	72.8
		rim	4	3.07	0.19	31.8	50.2	0.03	14.9	0.58	100.8	0.270	0.013	1.699	2.277	0.002	0.726	0.022	5.009	72.8
	13^	core	4	3.95	0.21	29.9	52.3	0.03	13.2	0.73	100.3	0.347	0.014	1.598	2.372	0.002	0.641	0.028	5.003	64.8
	16^	core	4	3.93	0.22	29.9	52.2	0.03	13.2	0.72	100.1	0.346	0.015	1.600	2.371	0.002	0.642	0.027	5.003	64.8
1 standard deviation (σ)				0.028	0.014	0.083	0.101	0.004	0.070	0.019	0.154	0.0027	0.0009	0.0030	0.0028	0.0003	0.0030	0.0008	0.003	0.254

All analyses by University of Hawaii electron microprobe. Total Fe assumed to be Fe^{3+}. An (anorthite) content is cationic ratio 100 Ca/(Ca+Na+K). n = number of probe analyses used in the average. *=visibly zoned, **=sieve texture, ^=plagioclase and clinopyroxene glomophyric intergrowth ^^=plagioclase and olivine glomophyric intergrowth, &&=plagioclase glomophyric intergrowth, &=skeletal.

Appendix E. MELTS Runs to Find Equilibrium Plagioclase Compositions

500b	assemblage	SiO_2	Al_2O_3	CaO	Na_2O	K_2O	An	longitude	region	Ca# glass	MgO glass
29-1	cpx, plag, oliv	49.6	32.3	15.1	2.95	0.02	73.8	92.618	PR	71.1	6.8361
31-1	cpx,plag,oliv	50.0	32.1	14.8	3.13	0.03	72.2	92.822	PR	68.8	6.3799
34-4	cpx,plag,oliv	49.3	32.6	15.4	2.79	0.02	75.2	93.010	PR	72.7	7.0152
36-1	cpx,plag,oliv	49.5	32.4	15.2	2.91	0.02	74.2	93.432	DR	72.0	7.0616
38-2	cpx, plag	49.5	32.4	15.1	2.92	0.02	74.0	93.268	OPR	72.0	6.7148
39-1	cpx,plag,oliv	48.9	32.8	15.7	2.61	0.02	76.7	93.218	OPR	73.7	7.3735
40-2	cpx,plag,oliv	47.7	33.6	16.6	2.08	0.01	81.5	93.158	OPR	78.3	8.7067
42-4	cpx,plag,oliv	47.4	33.8	16.8	1.95	0.01	82.7	93.205	ODR	80.4	8.7509
43-1	cpx, plag, oliv	47.8	33.6	16.5	2.12	0.01	81.1	93.257	ODR	79.4	8.7016
44-1	cpx, plag, oliv	47.9	33.5	16.4	2.17	0.01	80.6	93.295	ODR	76.3	8.5793
48-1	cpx,plag,oliv	48.3	33.2	16.1	2.37	0.01	79.0	93.657	DR	75.4	8.0631
49-1	plag, cpx, oliv	50.0	32.0	14.7	3.15	0.02	72.0	93.871	DR	69.2	6.5701
1000b	assemblage	SiO_2	Al_2O_3	CaO	Na_2O	K_2O	An	longitude	region	Ca# glass	MgO glass
29-1	cpx, plag	49.7	32.3	15.0	2.99	0.02	73.4	92.618	PR	71.1	6.8361
31-1	cpx,plag	50.2	31.9	14.6	3.22	0.03	71.4	92.822	PR	68.8	6.3799
34-4	cpx,plag	49.4	32.5	15.3	2.84	0.02	74.8	93.010	PR	72.7	7.0152
36-1	cpx,plag	49.6	32.3	15.1	2.95	0.02	73.7	93.432	DR	72.0	7.0616
38-2	cpx, plag	49.6	32.3	15.1	2.97	0.02	73.6	93.268	OPR	72.0	6.7148
39-1	cpx,plag	49.0	32.8	15.6	2.66	0.02	76.3	93.218	OPR	73.7	7.3735
40-2	cpx,plag,oliv	47.8	33.5	16.5	2.15	0.01	80.9	93.158	OPR	78.3	8.7067
42-4	cpx,plag,oliv	47.5	33.8	16.8	1.98	0.01	82.4	93.205	ODR	80.4	8.7509
43-1	cpx, plag, oliv	48.0	33.4	16.4	2.21	0.01	80.3	93.257	ODR	79.4	8.7016
44-1	cpx, plag, oliv	48.1	33.4	16.3	2.25	0.01	80.0	93.295	ODR	76.3	8.5793
48-1	cpx,plag,oliv	48.5	33.1	16.0	2.45	0.01	78.2	93.657	DR	75.4	8.0631
49-1	plag, cpx	50.2	32.0	14.7	3.20	0.03	71.6	93.871	DR	69.2	6.5701
1500b	assemblage	SiO_2	Al_2O_3	CaO	Na_2O	K_2O	An	longitude	region	Ca# glass	MgO glass
29-1	cpx, plag	49.9	32.1	14.9	3.08	0.03	72.6	92.618	PR	71.1	6.8361
31-1	cpx,plag	50.3	31.9	14.5	3.27	0.03	71.0	92.822	PR	68.8	6.3799
34-4	DOES NOT RUN IN MELTS							93.010	PR	72.7	7.0152
36-1	cpx,plag	49.8	32.2	14.9	3.05	0.03	72.9	93.432	DR	72.0	7.0616
38-2	cpx, plag	49.8	32.2	14.9	3.05	0.03	72.9	93.268	OPR	72.0	6.7148
39-1	cpx,plag	49.2	32.6	15.4	2.74	0.03	75.6	93.218	OPR	73.7	7.3735
40-2	cpx,plag,oliv	47.9	33.5	16.4	2.18	0.01	80.6	93.158	OPR	78.3	8.7067
42-4	cpx,plag	47.5	33.7	16.7	2.01	0.01	82.1	93.205	ODR	80.4	8.7509
43-1	cpx, plag, oliv	48.1	33.4	16.3	2.25	0.01	80.0	93.257	ODR	79.4	8.7016
44-1	cpx, plag, oliv	48.2	33.3	16.2	2.30	0.01	79.5	93.295	ODR	76.3	8.5793
48-1	cpx,plag,oliv	48.6	33.0	15.9	2.48	0.01	77.9	93.657	DR	75.4	8.0631
49-1	plag, cpx	50.4	31.8	14.5	3.30	0.03	70.8	93.871	DR	69.2	6.5701
2000b	assemblage	SiO_2	Al_2O_3	CaO	Na_2O	K_2O	An	longitude	region	Ca# glass	MgO glass
29-1	cpx, plag	50.0	32.1	14.8	3.12	0.03	72.3	92.618	PR	71.1	6.8361
31-1	cpx,plag,sp	50.5	31.7	14.4	3.36	0.03	70.2	92.822	PR	68.8	6.3799
34-4	cpx,plag	49.6	32.3	15.1	2.96	0.02	73.7	93.010	PR	72.7	7.0152
36-1	cpx,plag	49.9	32.1	14.9	3.08	0.03	72.6	93.432	ODR	72.0	7.0616
38-2	cpx, plag	49.9	32.1	14.9	3.09	0.03	72.6	93.268	PR	72.0	6.7148
39-1	cpx,plag	49.2	32.6	15.4	2.78	0.03	75.3	93.218	OPR	73.7	7.3735
40-2	cpx,plag,oliv	48.0	33.4	16.4	2.20	0.01	80.4	93.158	OPR	78.3	8.7067
42-4	cpx,plag	47.7	33.6	16.6	2.07	0.01	81.6	93.205	OPR	80.4	8.7509
43-1	cpx,plag	48.1	33.3	16.3	2.28	0.01	79.8	93.257	ODR	79.4	8.7016
44-1	cpx, plag, oliv	48.2	33.2	16.2	2.33	0.01	79.3	93.295	ODR	76.3	8.5793
48-1	cpx,plag	48.7	32.9	15.8	2.56	0.01	77.2	93.657	DR	75.4	8.0631
49-1	plag, cpx	50.5	31.7	14.4	3.38	0.03	70.0	93.871	DR	69.2	6.5701

TiO_2, Fe_2O_3, FeO, MnO, MgO, P_2O_5, H_2O = 0 wt%. cpx = clinopyroxene, plag = plagioclase, oliv = olivine, sp = spinel. Oxygen fugacity used was FMQ-2; measured water data was used when available, otherwise an average water content of 0.25 wt% was used.

.

Appendix F. Determining the Major Element Composition of the nT-MORB Parent Melt

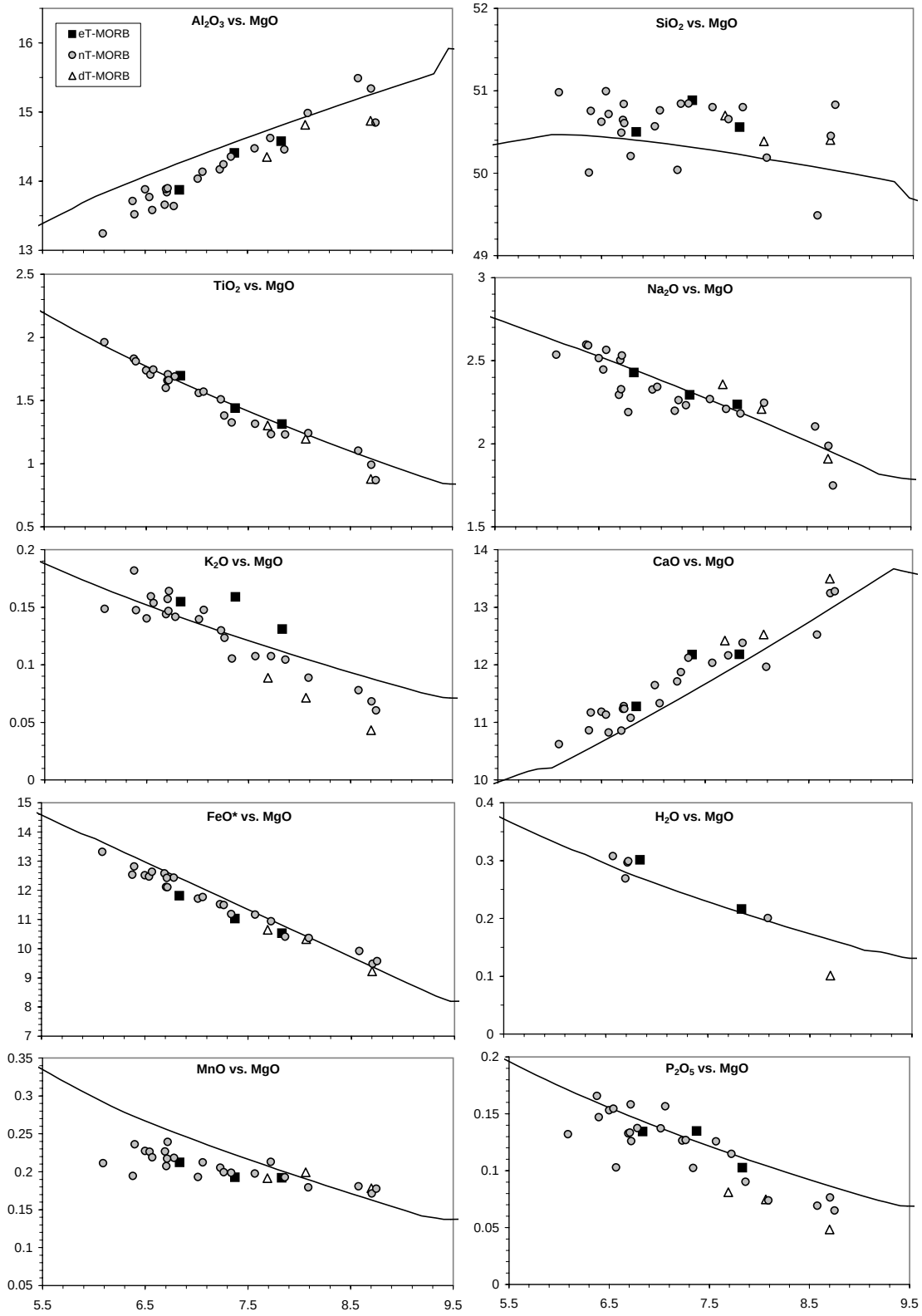

*Data are for microprobed glasses (Cushmam et al., 2004; Appendix A).

Appendix G. Determining the Trace Element Composition of the nT-MORB Primary Melt

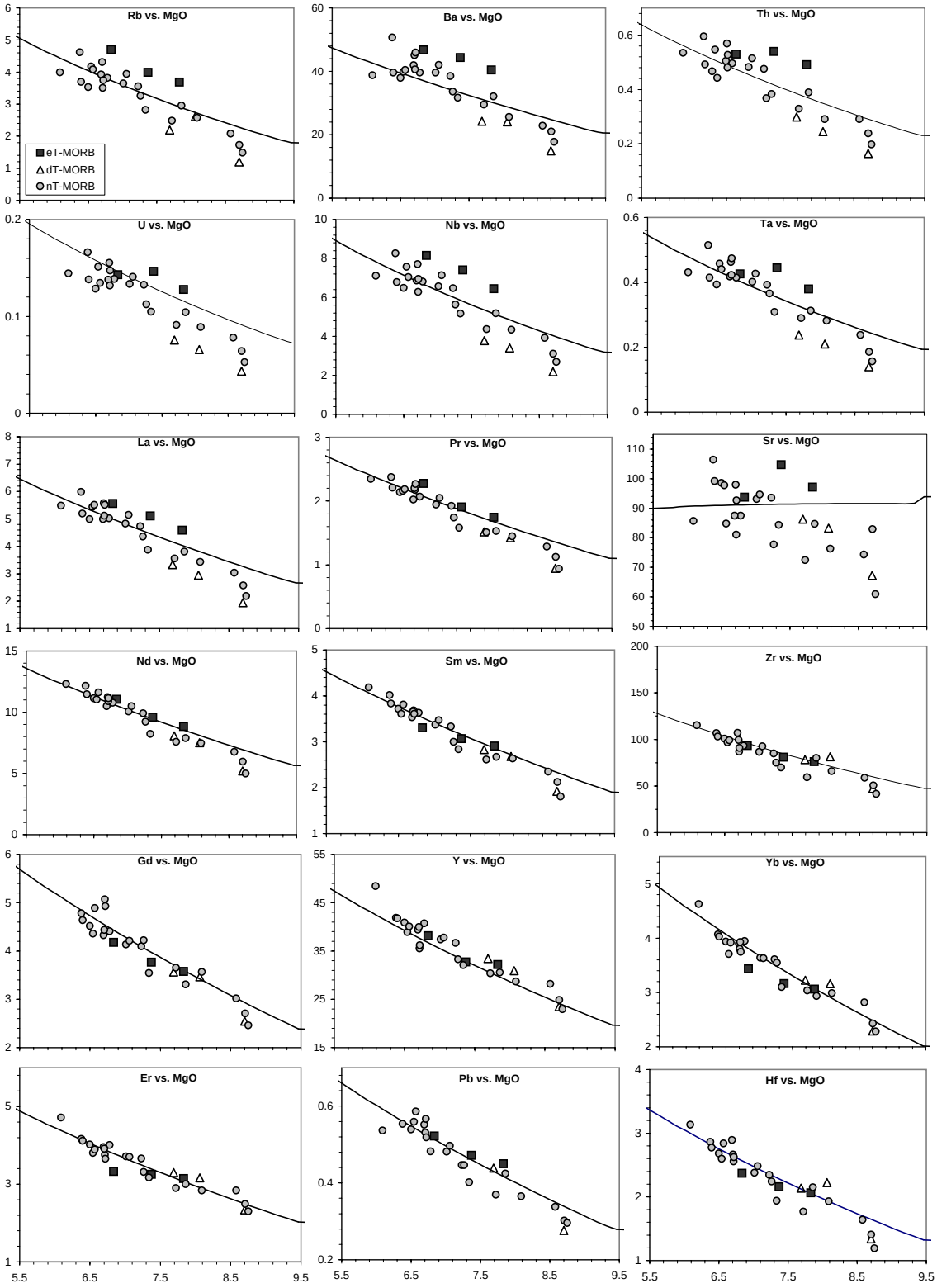

*Data are for microprobed glasses (Cushmam et al., 2004; Appendix A).

References

Behn, M.D., Sinton, J.M., and Detrick, R.S., 2004, Effect of the Galapagos hotspot on seafloor volcanism along the Galapagos Spreading Center (90.9˚ - 97.6˚W). Earth and Planetary Science Letters, v. 217, p. 331-347.

Bezos, A., and Humler, E., 2005, The $Fe^{3+}/\Sigma Fe$ ratios of MORB glasses and their implications for mantle melting: Geochimica et Cosmochimica Acta, v. 69, p. 711-725.

Blacic, T.M., Ito, G., Canales, J.P., Detrick, R.S., and Sinton, J.M., 2004, Constructing the crust along the Galapagos Spreading Center 91.3˚W - 95.5˚W: correlation of seismic layer 2A with axial magma lens and topographic characteristics: Journal of Geophysical Research, v. 109, p. 19.

Boyet, M., and Carlson, R.W., 2006, A new geochemical model for the Earth's mantle inferred from $^{146}Sm - ^{142}Nd$ systematics: Earth and Planetary Science Letters, v. 250, p. 254-268.

Byerly, G.R., Melson, W.G., 1976, Rhyodacites, andesites, ferro-basalts and ocean tholeiites from the Galápagos spreading center: Earth and Planetary Science Letters, v. 30, p. 215-221.

Byerly, G.R., 1980, The nature of differentiation trends in some volcanic rocks from the Galápagos Spreading Center: Journal of Geophysical Research, v. 85, p. 3797-3810.

Canales, J.P., Ito, G., Detrick, R.S., and Sinton, J.M., 2002, Crustal thickness along the western Galapagos Spreading Center and the compensation of the Galapagos hotspot swell: Earth and Planetary Science Letters, v. 203, p. 311-327.

Chappell, B., 1992, Trace element analysis of rocks by X-ray spectrometry: Advances in X-ray Analysis, v. 34, p. 263-276.

Chen, Y.J., and Lin, J., 2004, High sensitivity of ocean ridge thermal structure to changes in magma supply: the Galapagos Spreading Center: Earth and Planetary Science Letters, v. 221, p. 263-273.

Christie, D.M., Carmichael, I.S.E., and Langmuir, C.H., 1986, Oxidation states of mid-ocean ridge basalt glasses: Earth and Planetary Science Letters, v. 79, p. 397-411.

Christie, D.M., and Sinton, J.M., 1981, Evolution of abyssal lavas along propagating segments of the Galapagos spreading center: Earth and Planetary Science Letters, v. 56, p. 321-335.

Christie, D.M., and Sinton, J.M., 1986, Major element constraints on melting, differentiation and mixing of magmas from the Galapagos 95.5˚W propagating rift system: Contributions to Mineralogy and Petrology, v. 94, p. 274-288.

Christie, D.M., Werner, R., Hauff, F., Hoernle, K., and Hanan, B.B., 2005, Morphological and geochemical variations along the eastern Galapagos Spreading Center: Geochemistry, Geophysics, Geosystems, v. 6, p. 44.

Cooper, P.A., Milholland, P.D., and Duennebier, F.K., 1987, Seismicity of the Galapagos 95.5˚W propagating rift: Journal of Geophysical Research, v. 92, p. 14,091-14,112.

Cushman, B., Sinton, J.M., Ito, G., and Dixon, J.E., 2004, Glass compositions, plume-ridge interaction, and hydrous melting along the Galapagos Spreading Center, 90.5˚W to 98˚W: Geochemistry, Geophysics, Geosystems, v. 5, p. 30.

DeMets, C., Gordon, R.G., Argus, D.F., and Stein, S., 1994, Effect of recent revisions to

the geomagmatic reversal time scale on estimates of current plate motions: Geophysical Research Letters, v. 21, p. 2191-2194.

Detrick, R.S., Sinton, J.M., Ito, G., Canales, J.P., Behn, M., Blacic, T., Cushman, B., Dixon, J.E., Graham, D.W., and Mahoney, J.J., 2002, Correlated geophysical, geochemical, and volcanological manifestations of plume-ridge interaction along the Galapagos Spreading Center: Geochemistry, Geophysics, Geosystems, v. 3, p. 14.

Dunn, R., Toomey, D., Detrick, R., Wilcock, W., 2001, Continuous mantle melt supply beneath an overlapping spreading center on the East Pacific Rise: Science, p. 1955-1958.

Eason, D., and Sinton, J.M., 2006, Origin of high-Al N-MORB by fractional crystallization in the upper mantle beneath the Galapagos Spreading Center: Earth and Planetary Science Letters, v. 252, p. 423-436.

Fisk, M.R., 1986, Mid-ocean ridge basalts from the Galápagos Spreading Center: direct probes of magma chambers: Geology, v. 14, p. 204-207.

Fisk, M.R., Bence, A.E., and Schilling, J.G., 1982, Major element chemistry of Galapagos Rift Zone magmas and their phenocrysts: Earth and Planetary Science Letters, v. 61, p. 171-189.

Ghiorso, M.S., and Sack, R.O., 1995, Chemical mass transfer in magmatic processes IV. A revised and internally consistent thermodynamic model for the interpolation and extrapolation of liquid-solid equilibria in magmatic systems at elevated temperatures and pressures: Contributions to Mineralogy and Petrology, v. 119, p. 197-212.

Gripp, A.E., and Gordon, R.G., 2002, Young tracks of hotspots and current plate velocities: Geophysical Journal International, v. 150, p. 321-361.

Hanan, B.B., and Graham, D.W., 1996, Lead and helium isotope evidence from oceanic basalts for a common deep source of mantle plumes: Science, v. 272, p. 991-995.

Hey, R., 1977a, A new class of "pseudofaults" and their bearing on plate tectonics: a propagating rift model: Earth and Planetary Science Letters, v. 37, p. 321-325.

Hey, R., 1977b, Tectonic evolution of the Cocos-Nazca spreading center: Geological Society of America Bulletin, v. 88, p. 1404-1420.

Hey, R., Kleinrock, M.C., Miller, S.P., Atwater, T.M., Searle, R.C., 1986, Sea Beam / deep-tow investigation of an active oceanic propagating rift system, Galápagos 95.5 W: Journal of Geophysical Research, v. 91, p. 3369-3393.

Hey, R., Duennebier, F.K., and Morgan, J.W., 1980, Propagating rifts on mid ocean ridges: Journal of Geophysical Research, v. 85, p. 3647-3658.

Hey, R., Sinton, J.M., and Duennebier, F.K., 1989, Propagating rifts and spreading centers, *in* Winterer, E.L., Hussong, D.M., and Decker, R.W., eds., The Geology of North America, Volume N, The Eastern Pacific Ocean and Hawaii: Boulder, Colorado, Geological Society of America, p. 161-176.

Hey, R., Sinton, J.M., Kleinrock, M.C., Yonover, R.N., Macdonald, K.C., Miller, S.P., Searle, R.C., Christie, D.M., Atwater, T.M., Sleep, N.H., Johnson, H.P., and Neal, C.A., 1992, ALVIN investigation of an active propagating rift system, Galapagos 95.5° W: Marine Geophysical Researches, v. 14, p. 207-226.

Hey, R., and Vogt, P., 1977, Spreading center jumps and sub-axial asthenosphere flow near the Galápagos hotspot: Tectonophysics, v. 37, p. 41-52.

Ishikawa, A., Nakamura, E., and Mahoney, J.J., 2005, Jurassic oceanic lithosphere beneath the southern Ontong Java Plateau: Evidence from xenoliths in alnoite, Malaita, Solomon Islands; Geology, v. 33, p. 393-396.

Karsten, J.L., Delaney, J.R., Rhodes, J.M., and Liias, R.A., 1990, Spatial and temporal evolution of magmatic systems beneath the Endeavour segment, Juan de Fuca Ridge: tectonic and petrologic constraints: Journal of Geophysical Research, v. 95, p. 19,235-19,256.

Katz, R., Spiegelman, K.L., and Holtzman, B., 2006, The dynamics of melt and shear localization in partially molten aggregates: Nature, v. 442, p. 676-679.

Kent, G.M., Harding, A.J., and Orcutt, J.A., 1993, Distribution of magma beneath the East Pacific Rise between the Clipperton Transform and the 9˚17'N deval from forward modeling of common depth point data.: Journal of Geophysical Research, v. 98, p. 13,945-13,969.

Klein, E.M., and Langmuir, C.H., 1987, Global correlations of ocean ridge basalt chemistry with axial depth and crustal thickness: Journal of geophysical research, v. 92, p. 8089-8115.

Kleinrock, M.C., and Hey, R., 1989a, Detailed tectonics near the tip of the Galapagos 95.5˚W propagator: how the lithosphere tears and a spreading axis develops: Journal of Geophysical Research, v. 94, p. 13,801-13,838.

Kleinrock, M.C., and Hey, R.N., 1989b, Migrating transform zone and lithospheric transfer at the Galapagos 95.5˚W propagator: Journal of Geophysical Research, v. 94, p. 13,859-13,878.

Kleinrock, M.C., Searle, R.C., and Hey, R.N., 1989, Tectonics of the failing spreading

system associated with the 95.5˚W Galapagos propagator: Journal of Geophysical Research, v. 94, p. 13,839-13,857.

Langmuir, C.H., Klein, E.M., and Plank, T., 1992, Petrological systematics of mid-ocean ridge basalts: constraints on melt generation beneath ocean ridges, *in* Morgan, J.P., Blackman, D.K., and Sinton, J.M., eds., Mantle Flow and Melt Generation at Mid-Ocean Ridges, Volume Geophysical Monograph 71: Washington, DC, American Geophysical Union, p. 183-280.

Lonsdale, P., 1983, Overlapping rift zones at the 5.5˚S offset at the East Pacific Rise: Journal of Geophysical Research, v. 88, p. 9393-9406.

Lonsdale, P., 1985, Nontransform offsets of the Pacific-Cocos plate boundary and their traces on the rise flank: Geological Society of America Bulletin, v. 96, p. 313-327.

Lonsdale, P., 1986, Comments on "East Pacific Rise from Sequeiros to Orozco fracture zones: along-strike continuity of axial neovolcanic zone and structure and evolution of overlapping spreading centers" by K. Macdonald, J.Sempere and P.J. Fox: Journal of Geophysical Research, v. 91, p. 10,493-10499.

Macdonald, K., R.M., H., Miller, S.P., Sempere, J.-C., and Fox, P.J., 1988, Deep-tow and sea beam studies of dueling propagating ridges on the East Pacific Rise near 20˚40'S: Journal of Geophysical Research, v. 93, p. 2875-2898.

Macdonald, K.C., Sempere, J.C., and Fox, P.J.,1986, Reply: the debate concerning overlapping spreading centers and mid-ocean ridge processes: Journal of Geophysical Research, v. 91, p. 10,501-10,511.

Macdonald, K.C., Sempere, J.C., and Fox, P.J., 1984, East Pacific Rise from Siqueiros to

Orozco fracture zones: along strike continuity of axial neovolcanic zone and structure and evolution of overlapping spreading centers: Journal of Geophysical Research, v. 89, p. 6049-6069.

Macdonald, K., Sempere, J.-C., and Fox, P.J., 1987, Tectonic evolution of ridge-axis discontinuities by the meeting, linking, or self-decapitation of neighboring ridge segments: Geology, v. 15, p. 993-997.

Macdonald, K.C., and Fox, P.J., 1983, Overlapping spreading centers: new accretion geometry on the East Pacific Rise: Nature, v. 301, p. 55-58.

Mahoney, J., J., Sinton, J., M., Kurz, M.D., Macdougall, J.D., Spencer, K.J., and Lugmair, G.W., 1994, Isotope and trace element characteristics of a super-fast spreading ridge: East Pacific rise, 13-23˚S: Earth and Planetary Science Letters, v. 121, p. 173-193.

Mahoney, J.J., Le Roex, A.P., Peng, Z.X., Fisher, R.L., and Natland, J.H., 1992, Southwestern limits of Indian Ocean ridge mantle and the origin of low $^{206}Pb/^{204}Pb$ mid-ocean ridge basalt: isotope systematics of the Central Southwestern Indian Ridge (17˚-50˚E): Journal of Geophysical Research, v. 97, p. 19,771-19,790.

Mahoney, J.J., Nicollet, C., and Dupuy, C., 1991, Madagascar basalts: tracking oceanic and continental sources: Earth and Planetary Science Letters, v. 104, p. 350-363.

McKenzie, D., 1984, The generation and compaction of partially molten rock: Journal of Petrology, v. 25, p. 713-765.

McKenzie, D., and O'Nions, R.K., 1991, Partial melt distributions from inversion of rare-earth element concentrations: Journal of Petrology, v. 32, p. 1021-1091.

McKenzie, D., and O'Nions, R.K., 1995, The source regions of ocean island basalt: Journal of Petrology, v. 36, p. 133-159.

Norrish, K., and Hutton, J., 1977, An accurate X-ray spectrographic method for the analysis of a wide range of geological samples: Geochimica et Cosmochimica Acta, v. 33, p. 431-441.

Perfit, M.R., Fornari, D.J., Ridley, W.I., Kirk, P.D., Casey, J., Kastens, K.A., Reynolds, J.R., Edwards, M., Desonie, D., Shuster, R., Paradis, S., 1996, Recent volcanism in the Siqueiros transform fault; picritic basalts and implications for MORB magma genesis: Earth and Planetary Science Letters, v. 141, p. 91-108.

Phipps Morgan, J., 1987, Melt migration beneath mid-ocean spreading centers: Geophysical Research Letters, v. 14, p. 1238-1241.

Phipps Morgan, J., and Parmentier, E.M., 1985, Causes and rate-limiting mechanisms of ridge propagation: a fracture mechanics model: Journal of Geophysical Research, v. 90, p. 8603-8612.

Plank, T., and Langmuir, C.H., 1992, Effects of the melting regime on the composition of the oceanic crust: Journal of Geophysical Research, v. 97, p. 19,749-19,770.

Pollard, D.D., and Aydin, A., 1984, Propagation and linkage of oceanic ridge segments: Journal of Geophysical Research, v. 89, p. 10,017-10,029.

Pyle, D.D, Christie, D.M., Mahoney, J.J., Duncan, R.A., 1995, Geochemistry and geochronology of ancient southeast Indian and southwest Pacific seafloor: Journal of Geophysical Research, v. 100, p. 22,261- 22,282.

Roeder, P.L., and Emslie, P.L., 1970, Olivine-liquid equilibrium: Contributions to Mineralogy and Petrology, v. 29, p. 275-289.

Rubin, K.H., and Sinton, J.M., 2007, Inferences on mid-ocean ridge thermal and magmatic structure from MORB compositions: Earth and Planetary Science Letters, v. 260, p. 257-276.

Salters, V.J.M., and Stracke, A., 2004, Composition of the depleted mantle: Geochemistry, Geophysics, Geosystems, v. 5, p. 27.

Schilling, J.G., Fontignie, D., Blichert-Toft, J., Kingsley, R.H., and Tomza, U., 2003, Pb-Hf-Nd-Sr isotope variations along the Galapagos Spreading Center (101˚-83˚W): Constraints on the dispersal of the Galapagos mantle plume: Geochemistry, Geophysics, Geosystems, v. 4, p. 40.

Schilling, J.G., Anderson, R.N., and Vogt, P., 1976, Rare earth, Fe and Ti variations along the Galápagos Spreading Center and their relationship to the Galápagos Mantle Plume: Nature, v. 261, p. 108-113.

Schilling, J.G., Kingsley, R.H., and Devine, J.D., 1982, Galapagos hot spot-spreading center system 1. Spatial petrological and geochemical variations (83˚W-101˚W): Journal of Geophysical Research, v. 87, p. 5593-5610.

Schouten, H., and Klitgord, K.D., 1983, Overlapping spreading centers on East Pacific Rise, Comment: Nature, v. 303, p. 549-550.

Scott, D.R., and Stevenson, D.J., 1989, A self-consistent model of melting, magma migration, and buoyancy-driven circulation beneath mid-ocean ridges: Journal of Geophysical Research, v. 94, p. 2973-2988.

Sempere, J.-C., and Macdonald, K., 1986, Overlapping spreading centers: implications from crack growth simulation by the displacement discontinuity method: Tectonics, v. 5, p. 151-163.

Shah, A. K., and Buck, R.W. 2006, The rise and fall of axial highs during ridge jumps: Journal of Geophysical Research, v. 111, 12 pp.

Shaw, 1970, Trace element fractionation during anatexis: Geochimica et Cosmochimica Acta, v. 34, p. 237-243.

Sinton, J.M. and Detrick, R.S., 1992, Mid-ocean ridge magma chambers: Journal of Geophysical Research, v. 97, p. 197-216.

Sinton, J.M., Detrick, R.S., Canales, P.J., Ito, G., and Behn, M.D., 2003, Morphology and segmentation of the western Galapagos Spreading Center, 90.5˚-98˚W: Plume-ridge interaction at an intermediate spreading ridge: Geochemistry, Geophysics, Geosystems, v. 4, p. 26.

Sinton, J.M., Smaglik, S.M., and Mahoney, J.J., 1991, Magmatic processes at superfast spreading mid-ocean ridges: glass compositional variations along the east pacific rise 13˚-23˚S.: Journal of geophysical research, v. 96, p. 6133-6155.

Sinton, J.M., Wilson, D.S., Christie, D.M., Hey, R.N., and Delaney, J.R., 1983, Petrologic consequences of rift propagation on oceanic spreading ridges: Earth and Planetary Science Letters, v. 62, p. 193-207.

Smith, P.M., and Asimow, P.D., 2005, Adiabat_1ph: A new public front-end to the MELTS, pMELTS, and pHMELTS models: Geochemistry, Geophysics, Geosystems, v. 6, p. 8.

Spiegelman, M., and McKenzie, D., 1987, Simple 2-D models for melt extraction at mid-ocean ridges and island arcs.: Earth and Planetary Science Letters, v. 83, p. 137-152.

Spiegelman, M., 1996, Geochemical consequences of melt transport in 2-D; the

sensitivity of trace elements to mantle dynamics: Earth and Planetary Science Letters, v. 139, p. 115-132.

Sun, S.S., and McDonough, W.F., 1989, Chemical and isotopic systematics of oceanic basalts: implications for mantle composition and processes, *in* Saunders, A.D., and Norry, M.J., eds., Magmatism in the ocean basins, Volume 42, Geological Society Special Publication, p. 313-345.

Verma, S., and Schilling, J.G., 1982, Galapagos hot spot-spreading center system 2. $^{87}Sr/^{86}Sr$ and large ion lithophile element variations (85˚W-101˚W): Journal of Geophysical Research, v. 87, p. 10,838-10,856.

Wendt, I.J., Regelous, M., Niu, Y., Hekinian, R., and Collerson, K.D., 1999, Geochemistry of lavas from the Garrett Transform Fault: insights into mantle heterogeneity beneath the eastern Pacific: Earth and Planetary Science Letters, v. 173, p. 271-284.

Wilson, D.S., and Hey, R., 1995, History of rift propagation and magnetization intensity for the Cocos-Nazca spreading center: Journal of Geophysical Research: v. 100, p. 10041-10056.

Wilson, D.S., 1990, Kinematics of overlapping rift propagation with cyclic rift failure: Earth and Planetary Science Letters, v. 96, p. 384-392.

Wood, B.J., and Fraser, D.G., 1976, *Elementary thermodynamics for geologists*: Oxford University Press, Oxford, United Kingdom (GBR), 303 pp.

Workman, R.K., and Hart, S.R., 2005, Major and trace element composition of the depleted MORB mantle (DMM): Earth and Planetary Science Letters, v. 231, p. 53-72.